# Wake Control Strategies for a Large-Scale Offshore Wind Turbine: A Comparative CFD Study of Axial Induction & Yaw Control on the IEA 15MW Reference Turbine

Master's Thesis

by

Birta Aradóttir & Julia Holz

Department of Energy Sciences

Faculty of Engineering, LTH, Lund University

Supervised by Johan Revstedt

Examined by Jens Klingmann

June 8, 2026

ISRN LUTMDN/TMHP-26/5675-SE

ISSN 0282-1990

# Abstract

As offshore wind farms continue to grow in scale and number, wake interaction between turbines represents a significant source of power loss and increased fatigue risk. Consequently, there has been an increased interest in wake control strategies. Wake control strategies aim to mitigate these effects but their comparative effectiveness across power, wake velocity and turbulence intensity is not well established for large offshore turbines. Thus, a computational fluid dynamic (CFD) study comparing three wake control strategies: Axial induction control (AIC) via pitch and, via derating and yaw control, is conducted for a three-turbine inline offshore wind farm using the IEA 15MW reference turbine. This was conducted using OpenFOAM with turbinesFoam actuator line model (ALM) implementation and RANS $k-\epsilon$ turbulence modeling. The metrics evaluated for this study are: total farm power output, normalized streamwise velocity, and turbulence intensity along the farm centerline. Each strategy's control parameters were selected based on ranges reported in existing literature. AIC via pitch tested at $-5.0°$, $-2.5°$, $+2.5°$ and $+5.0°$, AIC via derating at 90%, 75% and 60%, and yaw control at 10°, 20° and 30°. The findings of this study revealed that AIC via negative pitch achieved the highest total farm power (+1.37%) for pitch $-2.5°$. However, as turbine 1, T1, operates below its optimal tip speed ratio (TSR), negative pitch increases $C_t$ rather than reducing it, deepening the downstream wake and reducing T2 and T3 power output. AIC via derating produced net negative farm power across all cases but achieved the greatest velocity improvement and turbulence intensity (TI) reduction behind T1, with a TI difference of -5.3% to -18% at T2 and -0.71% to -3.2% at T3, where TI decreased with higher derating levels. Yaw control produced the most balanced results, with a net farm gain of +0.32% for yaw 10° with meaningful downstream improvements, with a TI reduction of -1.15% at T2 and -0.48% at T3. All strategies showed limited benefit to T3 due to dominant wake formation behind T2. These results demonstrate that no single wake control strategy dominates across all performance metrics simultaneously. The decision of which strategy to choose is thus dependent on whether power maximization or fatigue risk reduction is the primary operating objective.



***Keywords:*** *Offshore Wind Farm · Wake Control · Axial Induction Control · Yaw Control · Computational Fluid Dynamics · Actuator Line Method · RANS · Turbulence Intensity · IEA 15MW Reference Turbine*

# Popular Science Article

As countries shift away from fossil fuels, making wind energy as efficient as possible becomes increasingly important. Today's offshore turbines are enormous, some taller than the Eiffel Tower, yet almost no research has examined whether wake control strategies work the same way for large turbines as they do for smaller ones. That is exactly the gap this thesis set out to fill.

Wind turbines are built both onshore and offshore in arrangements or farms that are planned to get the most possible energy output from the limited area available for construction. When the wind comes at a turbine, the turbine's blades rotate, using that rotation to produce energy. In the air directly after the turbine, there is still wind, but it has different properties. For example, the wind after the turbine is slower and choppier, like the flow of water after a boat, but with the wind turbine and air. Despite the previously mentioned planned arrangements of turbines for certain areas, the turbines are still close enough together that the changed wind after one turbine interacts with and affects the second turbine that is behind the first. When the second turbine experiences this affected wind it performs worse in the ways of less energy production, and the blades can experience more harmful strains due to the choppiness of the flow.

This thesis researches how the affected airflow behind an offshore turbine can be improved for the second turbine experiencing this flow behind the first. This improvement comes from changing aspects of the first turbine, such as adjusting the angles of the blades to the incoming wind, slowing down the speed of the blades, and tilting the whole turbine sideways. These adjustments decrease the amount of energy the first turbine takes from the wind so that the turbine after has more available energy to take from in the wind. This may decrease the energy output for the first turbine, but increases the energy produced from the turbine after it. Therefore, it is important to look at the total energy production which adds up the energy from every turbine in the farm. The goal is to increase total energy production and decrease the damaging strains on the blades of the latter turbines.

A key result from this research is that there in an undeniable tradeoff between energy production and the risk of damage from the strain on the turbine. This means that most methods follow the trend of increasing energy production but also increase the risk of damage, or vice versa. More results show that the strategy of tilting the whole turbine sideways by 10 degrees is the best option, since it leads to an increase in the total farm power while also decreasing the risk of damage to the turbine. Slowing down the speed of the blades of the first turbine best decreases the risk of damage to the turbine after it, but the decrease in energy production is too significant to be a realistic option.

A surprising detail that was found is that the turbine model used for reference is not actually designed to operate at optimal conditions. This leads to the conclusion that changing the angles of the blades to the incoming wind for the first turbine increases its energy production, because it is closer to operating at optimal conditions. This increases the total power output for the whole farm more than any other option, but it is not due to helping the latter turbines. This only benefits the first turbine, so it is not a relevant result to what this research is focusing on. Therefore, the energy production results for this method are not considered in the comparative analysis.

Now, the main benefit of this thesis is that it is a comparative study of large wind turbines. This study gives wind farm operators a clear picture of the tradeoffs when choosing how to control their turbines. If maximizing power is the goal, tilting it slightly sideways offers the most promising balance.

If reducing maintenance costs is the priority, slowing the first turbine down is the best option. Thus, the natural next step for this study would be to put a price tag on these tradeoffs, which can be done by calculating exactly how much money is saved by reducing turbine wear against how much revenue is gained from extra power. That calculation would give operators the economic tools to make the best decision for their specific farm, bringing wind energy one step closer to being not just cleaner, but smarter.

# Acknowledgments

We would like to begin by thanking our supervisor, Johan Revstedt, at the Department of Energy Sciences, Lund University. His guidance has been invaluable throughout this project, from navigating the steep learning curve of OpenFOAM to the many hours spent helping us troubleshoot our simulation. His expertise and patience made this work possible.

We would also like to thank the Department of Energy Sciences at Lund University for providing the resources necessary to conduct this research. The computational simulations were performed on resources provided by LUNARC, the Center for Scientific and Technical Computing at Lund University.

Lund, May 2026

Birta Aradóttir & Julia Holz

# Contents

# List of Figures

# List of Tables

# List of Acronyms

**ABL** Atmospheric Boundary Layer

**AIC** Axial Induction Control

**ALM** Actuator Line Method

**ADM** Actuator Disk Method

**BEM** Blade Element Momentum

**CFD** Computational Fluid Dynamics

**Cp** Power Coefficient

**Ct** Thrust Coefficient

**DEL** Damage Equivalent Load

**DTU** Technical University of Denmark

**FFA** Flygtekniska Försöksanstalten

**HAWT** Horizontal Axis Wind Turbine

**HPC** High Performance Computing

**IEA** International Energy Agency

**IEC** International Electrotechnical Commission

**LES** Large Eddy Simulation

**NREL** National Renewable Energy Laboratory

**PIMPLE** Merged PISO-SIMPLE algorithm

**PISO** Pressure Implicit with Splitting of Operators

**RANS** Reynolds-Averaged Navier-Stokes

**SIMPLE** Semi-Implicit Method for Pressure Linked Equations

**SLURM** Simple Linux Utility for Resource Management

**TI** Turbulence Intensity

**TSR** Tip Speed Ratio

**WPP** Wind Power Plant

**T1** Turbine 1

# 1 Introduction

## 1.1 Background

As global greenhouse gas emissions continue to increase, many countries are setting net-zero carbon emission goals. In order for these goals to be achieved, the transition from fossil fuels to renewable energy must be a priority. Specifically, offshore wind energy is continuously growing; in 2024, the global capacity grew to nearly 83 GW, increasing by almost 12% from 2023 [1]. Offshore wind power plants (WPP) are typically limited in area due to the economic, environmental, and technical practicalities of design. This results in turbines being positioned in close proximity, generating significant wake interactions between nearby turbines. When a downstream turbine is in the wake of another, it produces sub-optimal power and has an increased amount of structural loading [2]. This is because wakes characteristically have a lower wind speed and increased turbulence. The turbulence intensity (TI), overlapping of wakes, and wake meandering all contribute to the increased fatigue from structural loads on the downstream turbines [3]. With more fatigue on the wind turbines, the lifetime will decrease, and operation and maintenance costs will consequently increase for the WPP. The decrease in wind speed in the wake leads to decreased power output for the downstream turbines, because these turbines may not be able to operate at nominal power. This change in power production leads to less revenue overall for the WPP. Thus, by controlling the wakes, the economic outlook for the wind farm can be improved by increasing WPP power output and reducing fatigue risk via turbulence intensity control.

The thesis will focus on the following wake control methods: axial induction control (AIC) via blade pitching, AIC via derating, and yaw control (wake steering). Both AIC methods indirectly adjust the axial induction factor of the upstream wind turbines by modifying either the blade pitch or the generator torque. When altering the induction factor, the velocity deficit in the wake is reduced, thus improving the wind conditions experienced by downstream wind turbines. The yaw control, or wake steering method, intentionally misaligns upstream turbines with respect to the incoming wind direction to deflect their wakes away from downstream turbines, reducing wake interactions and associated power losses.[4] Some wake control methods increase the wake velocity by simultaneously increasing the turbulence intensity, which promotes mixing and quicker wake recovery. On the other hand, the level of turbulence intensity can be a proxy measurement of fatigue risk for each turbine. Therefore, it is important to weigh the benefits and risks of increasing the turbulence intensity of the wake.[5]

## 1.2 Literature Review

Wake management strategies have been researched for both individual wind turbines and WPPs for decades now. Each study covers a new gap in the field that the past research left open. In order to fully understand the knowledge gap this paper fills, it's important to establish a review of the previous knowledge that has gotten the field to where it is today. The existing literature around AIC with blade pitching shows that pitching towards stall, there is increased wake recovery for downstream turbines

[6]. Also pitching towards stall at the design tip speed ratio can increase the upstream turbine's own power coefficient by up to 22.8% [7], though this effect is specific to turbines operating below their aerodynamic optimal tip speed ratio. Studies using both large-eddy simulation and RANS CFD for turbines up to 5 MW support this conclusion. Although these studies did not include the observation of fatigue risk or structural loading. One study involving blade pitching for AIC did account for structural load implications, but looked only at individual pitch control rather than collective pitch control for a NREL 5 MW turbine. The results showed that this individual pitch control led to higher structural loading on the upstream turbine [8]. Larger turbines and farm-scale effects were not studied.

When it comes to derating for axial induction control, a wind tunnel experiment with small turbines found that derating the upstream turbine reduces its wake deficit, leading to an increase in the downstream turbines' power production. While another study found that derating factors of 20% and 40% for a 2 MW turbine model consistently reduced the fatigue loads at the nacelle, yaw bearing, blade root, and tower base [9]. While Bartl and Sætran [10] produced research on power maximization and Galinos et al. [9] on fatigue risk for AIC via derating. There is still a need for a large turbine study that includes simultaneous research on power and fatigue effects.

Wake steering via yaw control research for power maximizing is abundant, typically concluding that yaw control leads to higher WPP power output by deflecting the upstream turbines' wakes from the downstream ones, such as by Gebraad et al. [11] for a CFD (SOWFA) model for a NREL 5MW turbine. Due to this, yaw misalignment is considered one of the most practical wake control methods. But, there still needed to be information on how yawing affects structural fatigue. Bartl et al. [12] found through a wind tunnel experiment for two small turbines that as the yaw angles and power output increased, so did the amount of structural loading on both up- and down- stream turbines. This was one of the first studies to directly research power and fatigue affects in accordance to yaw angle changes. Despite this, there is still a need for this same study for larger turbines that could be used in offshore environments.

As shown, there are many studies that aim to increase power production for WPP, but there are also many that focus solely on improving the amount of fatigue damage for the turbines. In 2007 it was solidified by Frandsen [13] that the added turbulence from the wake is a primary contribution to fatigue damage for the downstream turbines. Specifically, it was found that the fatigue loads could increase by 5-15% for those turbines by Thomsen and Sørensen [14]. One of the most recent studies that contributes greatly to the scope of this thesis is by Ali et al. [15] that directly studied the structural loading of the IEA 15 MW turbine with varying inflow conditions, including turbulence intensities. They used Latin Hypercube Sampling and found that after wind speed, the turbulence intensity has the strongest correlation to structural loading, supporting our methodology for assessing fatigue risk. Ali et al. [15] directly call for future research to include how blade pitching and yaw alignment changes could influence their results.

The main takeaway is that despite the large amount of research that exists around this topic, there is a great need for a higher fidelity CFD study for large (15 MW) offshore turbines since modern-day turbines continue to grow in size. This study needs to consist of observing and comparing the effects of AIC via pitching & derating and yaw control on power production and fatigue risk. This is a gap no research has yet to fill, as studies that observe how yaw control affects fatigue and power with Fast.farm modeling exist [16], [17], but just look at yawing and do not use CFD modeling.

## 1.3 Aim, Purpose & Problem Statement

The goal of the thesis is to investigate the effects of different wake control methods for large offshore wind turbines and wind power plants using computational fluid dynamics (CFD). These impacts include power production and fatigue risk. The wake control methods that will be implemented for the study are axial induction control via blade pitch angle control, AIC via derating, and wake steering via yaw control. The purpose of this is to produce a study for a large-scale offshore turbine that equally analyzes the effects of wake control on power production and risk of fatigue for the turbines. Whereas past research has been for smaller turbines or focused solely on power production or structural fatigue, usually for only one wake management tactic. The wake control methods studied for this project provide a wider variety than previous studies have. Lastly, a thorough comparison and analysis will be performed to account for the tradeoffs related to structural fatigue risks and power output.

## 1.4 Delimitation

Not only is it important to establish the goal of this study, but it is also necessary to mention the boundaries that are set for the scope of the thesis. With respect to the type of turbine and WPP layout, only the IEA 15 MW is modeled, and just one layout option, which is detailed in section 3. The results may not apply to other turbine types, nor to staggered layouts with different spacing. Additionally, the rated and aligned wind speed of 10 m/s is the only velocity investigated; other wind directions and speeds would produce different outputs. For the atmospheric boundary layer (ABL), a neutral ABL with no additional atmospheric turbulence added is simulated. The potential impact of the Coriolis effect is also not introduced into this study, as the location of the WPP is assumed to be at the equator latitude.

The methodology delimitation should also be considered. Each wake control method is separately tested to determine the effects of each strategy, but no combined approaches are investigated. Going along with this, the first turbine of the column is altered by each approach, and only a selected range of values for each wake management tactic is chosen to be observed. Thus, the full affect and trend of the results for each method is not shown. Solely the RANS $k-\varepsilon$ turbulence model is used for predicting the wake recovery. The actuator line model (ALM) is implemented, so no geometrically resolved blades, hub, or tower are modeled. Lastly, for the assessment of turbine fatigue, only turbulence intensity is used as a qualitative proxy for structural fatigue risk. This means no actual structural load calculations or modeling is accomplished in this study.

## 1.5 Research Questions

- Which wake control method has the highest total power production for the WPP? Which wake control method has the highest power production for the downstream turbines? Do the answers to these previous questions coincide?

- Which wake control method best minimizes the deficit between freestream and downstream wake velocity? How does this relate to the rate of wake velocity recovery for downstream conditions?

- Which wake control method best reduces the risk of structural fatigue for the downstream turbines? Is redirecting the wake or lessening the wake best for controlling the effect of turbulence on the downstream turbines' fatigue?

- What benefits and disadvantages of fatigue risk reduction and increased power production are considered for choosing the best wake control method? What tradeoffs between reduced structural fatigue risk and increased power production are significant?

# 2 Theory

## 2.1 Wind Turbine Aerodynamics

The interaction of incoming wind and rotating blades determines a wind turbine's power production as well as the aerodynamic loads imposed upon its structure. [5] Understanding this interaction is fundamental for analyzing how wake control strategies affect turbine operating conditions and their downstream consequences. This section presents the key aerodynamic concepts governing wind turbine operation, from the idealized actuator disk model to blade-scale aerodynamics.

The device that carries out the process of extracting energy in a wind turbine is called an actuator disc. [5] For this concept, the rotor of the turbine is represented as an infinitely thin disc which extracts momentum from the incoming flow, around which a stream-tube can be defined, as can be seen in figure 1.

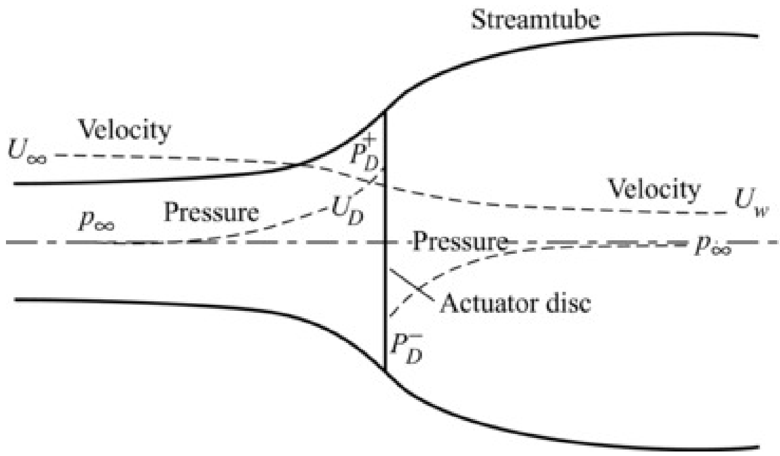


Figure 1: Schematic of an energy extracting actuator disc and stream-tube, illustrating the velocity reduction and pressure variation across the rotor plane. Reproduced from Burton et al. [5]

When the freestream velocity interacts with the actuator disc, the actuator disc induces a velocity variation, changing the flow of the freestream velocity. This induced flow at the disc's stream-wise component is defined as: [5]

$$U_D = U_\infty(1-a) \tag{1}$$

where $a$ is the axial induction factor representing the fractional reduction in wind speed at the rotor disk. As the air travels through the disc, it experiences an overall change in velocity and rate of change of momentum. From momentum theory, the power extracted by the rotor is: [5]

$$P = \frac{1}{2}\rho A U_\infty^3 \cdot 4a(1-a)^2 \tag{2}$$

where $\rho$ is the air density, A is the rotor swept area, and $U_\infty$ is the freestream wind speed. The power coefficient normalizes this by the available power in the undisturbed freestream:

$$C_p = \frac{P}{\frac{1}{2}\rho A U_\infty^3} = 4a(1-a)^2 \tag{3}$$

The thrust coefficient $C_t$ describes the aerodynamic thrust force exerted on the rotor, normalized by the available dynamic pressure:

$$C_t = 4a(1-a) \tag{4}$$

As both $C_p$ and $C_t$ depend solely on a, modifying the induction factor via AIC simultaneously shifts the turbine operating point along both curves.[5] The Betz optimum occurs at a = 1/3, giving maximum power extraction of $C_{p,max} = 16/27 \approx 0.593$. No wind turbine can exceed this theoretical maximum. [5]

The actuator disc theory is then expanded upon in the blade-element/momentum theory (BEM), which combines the actuator disk momentum theory with blade element aerodynamics. The BEM theory is based on the fundamental assumption that each blade element's force acts exclusively on the axial momentum of the air passing through the ring-shaped region it sweeps.[5] This assumption holds true only when the blade slows down the incoming air by the same amount at every point along its length. In practice, this is rarely the case, which represents one of the key limitations of the BEM theory. [5]

A key parameter in BEM theory is the tip speed ratio $\lambda$, which defines the turbine's aerodynamic operating point by relating the blade tip velocity to the freestream wind speed: [5]

$$\lambda = \frac{\Omega R}{U_\infty} \tag{5}$$

where $\Omega$ is the rotor angular velocity and R is the rotor radius. The relationship between $C_p$ and $\lambda$ is described by the $C_p - \lambda$ curve, which peaks at $\lambda_{opt}$. When operations are at $\lambda_{opt}$ maximum power extraction can occur, however, if deviated from this point, a reduction in $C_p$ and $C_t$ occurs. [5]

The local angle of attack $\alpha$ at each blade element is determined by the inflow angle $\phi$ that is set by the ratio of axial to rotational velocity components at the radial position and the local pitch angle $\theta$:

$$\alpha = \phi - \theta \tag{6}$$

where the aerodynamic forces at each element are determined by $\alpha$ and the aerodynamic properties of the airfoil profile at that blade section. Increasing $\theta$ via pitch control directly reduces $\alpha$, decreasing the lift force and consequently $C_t$, while derating shifts the turbine away from $\lambda_{opt}$, also reducing $C_t$ through a different aerodynamic path. While BEM provides the theoretical foundation for blade aerodynamics, the actuator line method used in this thesis extends these principles to a full CFD framework as described in Section 2.7.

## 2.2 Wake Aerodynamics

In a wind farm, turbines rarely operate in undisturbed freestream conditions. As each turbine extracts kinetic energy from the incoming wind, it leaves behind a region of reduced wind speed and elevated turbulence known as a wake. The velocity deficit describes the local reduction in wind speed within the wake relative to the undisturbed freestream, expressed as $\Delta U = U_\infty - U(x,r)$. [18] This phenomenon directly reduces the power available to downstream turbines, while elevated turbulence increases their structural loading. Understanding the structure and recovery of a wake is therefore fundamental to the analysis of wake control strategies.

Wakes can be categorized into two regions: near- and far wake regions. The near wake region is considered the area near the rotor and extends around 2 to 5 rotor diameters downstream. [19] This region is often highly turbulent due to the interaction of the flow with the rotor geometry, resulting in blade tip vortices, steep pressure gradients, and wake expansion. The tip vortices shed from the blade tips describe helical trajectories, forming a cylindrical shear layer. [20] This layer separates the decelerated fluid within the wake from the fluid outside it. Under yaw misalignment, the rotor additionally generates a counter-rotating vortex pair that causes the wake cross-section to deform laterally into a curled shape, resembling a kidney shape. This phenomenon is known as the curled wake. [21] This lateral deformation is the primary physical mechanism exploited by yaw control strategies to deflect the wake away from downstream turbines. As turbulent diffusion causes this shear layer to grow in thickness with downstream distance, it eventually reaches the wake centerline, marking the transition to the far wake where the wake is considered fully developed.[19] In the far wake region, turbulent diffusion dominates and the velocity deficit gradually recovers towards freestream conditions. The turbulence intensity ($TI$), defined as:

$$TI = \frac{\sigma_u}{U_\infty} \tag{7}$$

where $\sigma_u$ is the standard deviation of streamwise velocity fluctuations. The turbulence intensity is influenced by the rotor-induced turbulence and the atmospheric turbulence. Peak TI occurs at the wake edges rather than at the centerline, due to the high shear in the cylindrical shear layer. [19] The velocity deficit in the far wake region follows a Gaussian profile where the velocity reduction is greatest at the wake centerline and decreases smoothly and symmetrically towards the wake edges where wind speed approaches freestream. [22] The rate of this recovery is driven by turbulent mixing; both rotor-induced turbulence from the shear layer and ambient atmospheric turbulence contribute to drawing in higher momentum fluid from outside the wake, gradually restoring the velocity deficit toward freestream conditions. [19] The rate of wake recovery is further governed by the upstream turbine's thrust coefficient $C_t$, where a higher $C_t$ produces a deeper initial velocity deficit and slower recovery, making it the primary aerodynamic parameter targeted by the wake control strategies discussed in Section 2.4. [22] [5] In wind farm context, these wake interactions become particularly significant in multi-turbine arrays, where the combined velocity deficits of multiple upstream wakes determine the operating conditions of downstream rotors. [19]

## 2.3 Fatigue Risk

As mentioned above in section 2.2 and shown in equation (7), turbulence intensity is directly related to the standard deviation of streamwise velocity fluctuations. If a turbine experiences a turbulent flow, these fluctuations lead to chaotic and unsteady aerodynamic loads on the rotor blades. As these variable loads are continuously applied to the blades throughout the lifetime of the turbine, fatigue damage builds [5]. Additionally, fatigue damage accumulates faster when the frequency and amount of load fluctuations increase. A higher turbulence intensity leads to this increase in load variability, thus increasing fatigue damage. To fully confirm that turbulence intensity and structural strain correlate, it begins with the relative velocity ($V_{\text{rel}}$) on the blade element level defined as:

$$V_{\text{rel}}^2 = (U + u')^2 + (\Omega r)^2 \approx U^2 + 2Uu' + (\Omega r)^2 \tag{8}$$

where $u'$ represents the fluctuations in the turbulent flow. Equation (8) shows that changes in the amount of turbulent fluctuations affects the relative velocity, thus affecting the lift force, as seen in equation (9), of each blade element also. This proves how higher turbulence intensity directly leads to a larger difference in the lift force on the blade.[5]

$$\Delta F_L = \frac{1}{2}\rho\,\Delta(V_{\text{rel}}^2)\,c\,\Delta r \cdot C_L(\alpha) \tag{9}$$

This relation is not only proven through these equations, but also by the framework for a fatigue analysis. Hu et al. [23] show with their research that when calculating annual fatigue damage, it is necessary to use a distribution over ten minutes of both wind speed and turbulence intensity, not just wind speed. This is seen in equation (10) for the scaling of the standard deviation of the flapwise bending moment ($\sigma_M$) at the structural level:

$$\sigma_M \propto I_u \cdot U^2 \tag{10}$$

where $I_u$ is the longitudinal turbulence intensity. [13] This proves the direct and linear correlation between the turbulence intensity and the magnitude of structural load fluctuations. The Palmgren-Miner rule and S-N curve combine to show that the unsteady structural loads add up to fatigue damage to the turbine throughout its operational lifetime.[5], [24]

$$D = \sum_i \frac{n_i}{N_i} \tag{11}$$

$$N_i = C \cdot S_i^{-m} \tag{12}$$

where $n_i$ is the amount of cycles experienced at a certain stress level, $S_i$, and $N_i$ is the total number of cycles the material can operate at until structural failure; this occurs when D=1. The values $S_i$ and $N_i$ are obtained from the S-N curve, equation (12), where $m$ is the Wöhler or fatigue exponent. The last theoretical base for using turbulence intensity as a proxy for structural fatigue risk is the effective turbulence intensity equation [25]:

$$I_{eff} = \frac{1}{U}\sqrt{\frac{1}{T}\int_0^T u'^2\,dt} \tag{13}$$

where $u'$ is again the turbulent fluctuations in velocity and $T$ is the averaging period. The IEC 61400-1 uses this statistical TI equation in the context of fatigue design cases. Lastly, since this research uses RANS modeling, the following equation is used instead to approximate turbulence intensity:

$$TI = \frac{\sqrt{2k/3}}{U_\infty} \times 100\% \tag{14}$$

where $\sqrt{2k/3}$ is the root-mean-square (rms) turbulent velocity which comes from the $k-\varepsilon$ model and kinetic energy $k$. This is the RANS equivalent of the IEC standard TI definition equation (13). This leads to the conclusion that TI can be used as a proxy or qualitative indicator for fatigue risk.

## 2.4 Wake Management Strategies

Wake management strategies are of great interest for the development of future wind farms. As previously mentioned, the operations of wind farms are significantly impacted by wake formation from upstream wind turbines. Therefore, there is a need for intervention to prevent or mitigate these effects. The goal of wake management is to identify approaches to lessen the negative impact of wake formation in wind farms, hence improving the design of wind farms overall. The wake management strategies that are of importance for this thesis are Yaw control and Axial induction control via derating and pitch control. The axial induction control reduces the wake deficit while the yaw control method deflects the wake laterally. [4]

Axial induction control (AIC) is a wake management technique that involves reducing the induction factor of upstream turbines in order to improve the wake conditions experienced by downstream turbines. The aim is to increase total farm power production while reducing structural loading on downstream rotors. The induction factor can be controlled by either altering the blade pitch angle or the operating point of the rotor, thereby slowing the rotor speed. [4] A reduced induction factor leads to a faster recovering wake, the upstream turbine extracts less momentum from the flow, thus leaving a shallower velocity deficit in the wake. [26] The induction factor $a$ is directly correlated to the thrust coefficient $C_t$ as seen in equation (4). AIC deliberately operates the upstream turbine below this point, reducing both $a$ and $C_t$, which is the fundamental mechanism enabling wake recovery improvement. [4]

AIC via pitch control operates by increasing the blade pitch angle while maintaining a constant tip speed ratio (TSR) of the upstream wind turbine.[27] Blade pitching can be done in a collective or individual manner, where individual blade pitching consists of each blade having different pitching offsets applied [28]. Most studies observe the impacts of collective blade pitching. When the pitch is increased, there is a resultant reduced lift force on the blades, thus a decreased rotor-integrated thrust force, which directly determines the momentum extracted from the flow and in return lowers the axial induction factor and $C_t$. This decreases the power production of the upstream wind turbines while increasing the wind velocity in their wakes, resulting in increased power production in the downstream turbines and decreased turbulence intensity in the wake, leading to reduced load on the downstream turbines. This tradeoff can only be meaningful if the downstream gains exceed this upstream loss.

[27] While pitch control achieves this by modifying blade aerodynamics, generator torque derating reaches the same objective through the drivetrain.

AIC via derating is implemented by operating the upstream turbine at a fixed percentage of its rated power output. This approach, sometimes referred to as delta control, is an established method for active power curtailment in commercial wind turbines. [29] [30] The turbine's power production is intentionally curtailed, e.g., to 90% or 80% of rated power, in order to reduce the thrust coefficient $C_t$ and improve wake recovery for downstream turbines. The blade pitch angle remains fixed throughout. As $C_t$ decreases, the upstream turbine extracts less momentum from the flow, producing a shallower velocity deficit in the wake. [4] The tradeoff is a direct reduction in upstream turbine power output, which is only beneficial at the farm level if the downstream power gains exceed this loss. The specific numerical implementation of this derating within the CFD framework is discussed in Section 3.3.

The yaw control method is a wake management technique that involves rotating the rotor plane about the vertical axis to deflect the wake away from downstream turbines. [4] The purpose of yaw control is to steer the wake away from downstream turbines in order to increase farm power production and decrease fatigue risk on downstream rotors. The controlling factor is the misalignment angle $\gamma$, defined as the angle between the rotor normal and the incoming wind direction, as illustrated in figure 2.

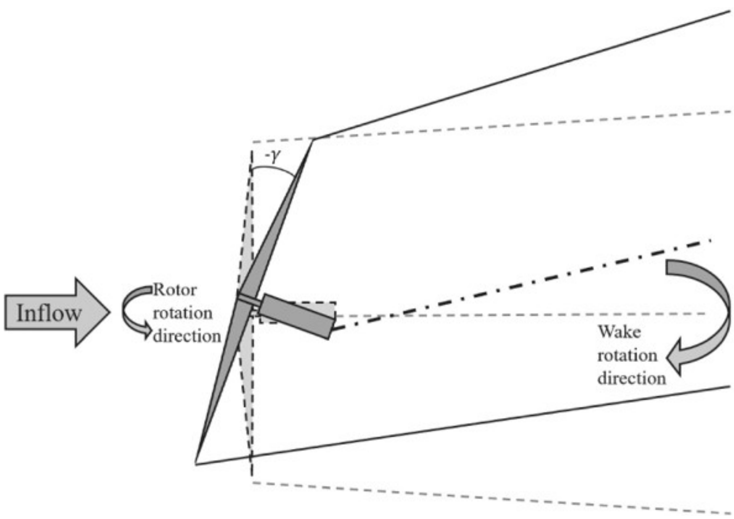


Figure 2: Yaw control setup [4]

Under yaw misalignment, the component of wind speed normal to the rotor plane is reduced to $U_\infty \cos(\gamma)$. The thrust force ($F_T$) acting on the rotor therefore scales as:

$$F_T = \frac{1}{2}\rho A U_\infty^2 C_t \cos^2(\gamma) \tag{15}$$

reflecting the reduced rotor-normal velocity component. [21] The misaligned thrust vector introduces a lateral force component that pushes the wake sideways, deflecting the wake centerline away from the downstream turbine. This lateral deflection is further reinforced by a counter-rotating vortex pair generated by the misaligned rotor, which deforms the wake cross-section into a characteristic curled shape. [21] The resulting upstream power loss is commonly approximated as proportional to $\cos^p(\gamma)$, where the exponent $p$ typically ranges between 2 and 3 depending on turbine type and wind speed conditions. [11] [31] As a result, downstream turbines experience a higher effective wind speed and reduced turbulence intensity compared to the unyawed case, improving both power production and fatigue risk.

In the CFD implementation used in this thesis, yaw misalignment is applied by rotating the rotor axis by $\gamma$ while maintaining the freestream direction, such that the rotor-normal velocity component is genuinely reduced to $U_\infty \cos(\gamma)$. This produces a physically representative upstream power penalty consistent with analytical model assumptions. The specific implementation is detailed in Section 3.4. Typical yaw angles in existing literature range from 10° to 30°, with higher misalignment angles producing greater wake deflection at the cost of increased upstream power loss. [32]

All wake strategies mentioned above sacrifice upstream turbine power in efforts to increase power production and decrease fatigue risk in the downstream turbines. AIC does this by reducing the induction factor via derating or pitching, reducing the wake deficit. Yaw control on the other hand, deflects the wake laterally, causing a reduction in the effective wind speed component normal to the rotor. This sacrifice in power production in the upstream turbine can only be meaningful if the wind farms total power production is increased or stays the same as well as if the reduction in fatigue risk in the downstream turbines reduces maintenance needed.

## 2.5 Governing Equations

Computational fluid dynamics is a numerical approach for solving fluid flow problems by discretising and solving the governing equations of fluid motion. These equations express the conservation of mass and momentum for a viscous fluid. The governing equations are the foundation of all CFD solvers, including the OpenFOAM solver used in this thesis. For wind farm flow, where air velocities are well below the speed of sound, and can therefore be treated as incompressible, meaning density is assumed constant throughout the domain.[33] Under this assumption, the flow is governed by the continuity and momentum equations.[34] The continuity equation expressing conservation of mass reduces to:

$$\frac{\partial u_i}{\partial x_i} = 0 \tag{16}$$

The momentum equation in Navier-Stokes form is:

$$\frac{\partial u_i}{\partial t} + u_j \frac{\partial u_i}{\partial x_j} = -\frac{1}{\rho}\frac{\partial p}{\partial x_i} + \nu \frac{\partial^2 u_i}{\partial x_j \partial x_j} \tag{17}$$

where $\rho$ is the fluid density, $p$ is the pressure, $\mu$ is the dynamic viscosity of the fluid, and $\nu = \mu/\rho$ is the kinematic viscosity. The left-hand side represents unsteady and convective acceleration, while the right-hand side represents pressure and viscous forces acting on the fluid. However, directly solving these equations for turbulent flows at engineering Reynolds numbers is computationally intractable due to the wide range of turbulent length and time scales present. [33] This motivates the Reynolds-averaging approach described in Section 2.6.

## 2.6 RANS Turbulence Modeling

As mentioned previously, simulations with incompressible, Newtonian fluids use the Navier-Stokes governing equations for the conservation of mass and momentum. When it comes to turbulent flows, solving these equations require some extra steps. Versteeg and Malalasekera [35] provide the information for the whole following RANS turbulence modeling section; the Reynolds number (Re) for a certain flow determines whether the regime is laminar or turbulent. Flows that have a Re above the critical Reynold number ($Re_{crit}$) are considered turbulent. Turbulent flows have random and unsteady flow behavior. In order to utilize the Navier-Stokes equations, the flow property values are decomposed into a steady time-averaged value and a fluctuating component, called the Reynolds decomposition and seen in equation (18), to account for the randomness of the turbulent flow.

$$u_i = \bar{u}_i + u_i' \tag{18}$$

where $u_i$ is the instantaneous velocity component, $\bar{u}_i$ is the time-averaged mean velocity component, and $u_i'$ is the turbulent fluctuation about the mean.

When the Reynolds decomposition is applied to the Navier-Stokes equations, the Reynolds Averaged Navier-Stokes (RANS) equations are produced, shown below as equation (19).

$$\frac{\partial \bar{u}_i}{\partial t} + \bar{u}_j \frac{\partial \bar{u}_i}{\partial x_j} = -\frac{1}{\rho}\frac{\partial \bar{p}}{\partial x_i} + \nu \frac{\partial^2 \bar{u}_i}{\partial x_j \partial x_j} - \frac{\partial \overline{u_i' u_j'}}{\partial x_j} \tag{19}$$

where $\bar{p}$ is the time-averaged pressure, and $\overline{u_i' u_j'}$ is the Reynolds stress tensor. This accounts for how the turbulent fluctuations affect the mean flow. The Reynold's stress tensor unfortunately creates an unsolvable scenario with more variables than equations to solve; this is referred to as the closure problem. The most practiced approach to solving this closure problem is the Boussinesq Hypothesis shown with equation (20). This hypothesis suggests that the Reynolds stresses may be proportional to the mean rates of deformation. This hypothesis is a very large simplification, but serves as an efficient solution and a basis for the $k-\varepsilon$ model.

$$-\overline{u_i' u_j'} = \nu_t \left( \frac{\partial \bar{u}_i}{\partial x_j} + \frac{\partial \bar{u}_j}{\partial x_i} \right) - \frac{2}{3} k \delta_{ij} \tag{20}$$

where $\nu_t$ is the turbulent eddy viscosity, $k = \frac{1}{2}\overline{u_i' u_i'}$ is the turbulent kinetic energy, and $\delta_{ij}$ is the Kronecker delta. The eddy viscosity $\nu_t$ is a flow property that varies in space and time and is determined by the turbulence model.

This simulation uses the standard $k-\varepsilon$ turbulence model which solves the closure problem through the addition of solving two transport equations. One transport equation is for the turbulent kinetic energy ($k$), equation (21). The other transport equation is for the turbulent dissipation rate ($\varepsilon$) shown in equation (23).

$$\frac{\partial k}{\partial t} + \bar{u}_j \frac{\partial k}{\partial x_j} = \frac{\partial}{\partial x_j}\left[ \left( \nu + \frac{\nu_t}{\sigma_k} \right) \frac{\partial k}{\partial x_j} \right] + P_k - \varepsilon \tag{21}$$

where $\sigma_k$ is the turbulent Prandtl number for $k$, $\varepsilon$ is the turbulent dissipation rate, and $P_k$ is the production of turbulent kinetic energy due to mean flow shear, defined as:

$$P_k = \nu_t \frac{\partial \bar{u}_i}{\partial x_j} \left( \frac{\partial \bar{u}_i}{\partial x_j} + \frac{\partial \bar{u}_j}{\partial x_i} \right) \tag{22}$$

$$\frac{\partial \varepsilon}{\partial t} + \bar{u}_j \frac{\partial \varepsilon}{\partial x_j} = \frac{\partial}{\partial x_j} \left[ \left( \nu + \frac{\nu_t}{\sigma_\varepsilon} \right) \frac{\partial \varepsilon}{\partial x_j} \right] + C_1 \frac{\varepsilon}{k} P_k - C_2 \frac{\varepsilon^2}{k} \tag{23}$$

where $\sigma_\varepsilon$ is the turbulent Prandtl number for $\varepsilon$, and $C_1$ and $C_2$ are empirical model constants. [35]

The limitations and assumptions that exist with RANS, and specifically $k-\varepsilon$ turbulence models, are not to be ignored. For RANS models, the actual turbulent fluctuations cannot be resolved, so the flow is time-averaged [35]. Additionally, RANS has higher accuracy in far wake regions because the flow is more homogeneous, and the assumptions associated with the Boussinesq hypothesis are more realistic for these conditions [19], [34]. Therefore, in the near wake regions, the areas with the most blade tip vortices and pressure gradients, RANS is the least reliable. Due to this inability to resolve the shear layer eddies and tip vortices, the magnitude of the peak turbulence intensity in this near-wake region is typically under-predicted. On the other hand, when it specifically comes to the exact model used for this research, the $k-\varepsilon$ model, the turbulent mixing or the wake recovery rate is over-predicted. An effect of this is that the power output of the downstream turbines may be calculated as higher than actuality, because the velocity deficit in the wake will seem to recover faster when using the $k-\varepsilon$ model [34]. An important distinction for the $k-\varepsilon$ model is that the turbulent kinetic energy is modeled statistically, so the k field does not represent resolved velocity fluctuations. The k field rather portrays the modeled turbulent energy, so it is not a physical embodiment of instantaneous flow [35]. The large eddy simulation (LES) method would provide much more accurate predictions for the wake turbulence, especially near wake, because it is able to resolve the large-scale eddies and only models the small scales. The limitation here is that LES is 10-100 times more computationally expensive that RANS modeling.

## 2.7 Actuator Line Method

Representing the aerodynamic influence of wind turbine blades in a CFD domain requires a choice between methods of varying fidelity and computational cost. At one end of the spectrum, full blade resolved simulations capture the complete geometry but are computationally expensive for farm-scale studies. At the other end, the actuator disk method (ADM) represents the entire rotor as a porous disk imposing a spatially uniform axial body force, which is computationally efficient but sacrifices near-wake resolution and cannot capture tip vortices or unsteady blade loading. The actuator line method (ALM), developed by Sørensen and Shen (2002) [36], is able to combat the accuracy limitations of the ADM while also remaining computationally cheap compared to a full blade-resolved simulation. It retains the physical fidelity of blade-scale aerodynamics and tip vortex formation while remaining manageable for multi-turbine farm simulations. For this thesis, where the accurate resolution of wake structure under different control strategies is central to the analysis, the ALM was selected as the rotor representation method. [37]

The ALM is able to compute the forces upon the turbine blade by simulating each turbine blade as a line where aerodynamic forces are placed along it. This is done by dividing the blade into blade elements with an actuator point at the center of each element, portraying its blade properties. The aerodynamic forces, lift and drag, are calculated based on the local relative velocity and angle of attack. The local relative velocity at each actuator point is the vector sum of the incoming flow velocity and the rotational velocity of the blade at that radial position, $\omega$r, from which the local angle of attack is determined. These aerodynamic forces are obtained from existing two-dimensional airfoil data, given the lift and drag coefficients $C_l$ and $C_d$ as a function of angle of attack for the airfoil profile at that blade section. This gives the aerodynamic force per unit span at each actuator point. [38] Because the blade geometry rotates through the fixed CFD mesh at each time step, the ALM is inherently unsteady and requires a time-marching simulation. The aerodynamic forces at each actuator point are then projected onto the surrounding mesh cells using the Gaussian kernel: [36]

$$\eta_\varepsilon(r) = \frac{1}{\varepsilon^3 \pi^{\frac{3}{2}}} exp(-\frac{r^2}{\varepsilon^2}) \tag{24}$$

where $r$ is the distance from the actuator point to the mesh cell center and $\varepsilon$ is the kernel width parameter. The choice of $\varepsilon$ involves a fundamental trade-off. It must be large enough relative to the local cell size to maintain numerical stability, but small enough to preserve the spatial fidelity of the blade force distribution. [39] [40] The specific determination of the turbinesFoam implementation used for this thesis is discussed in Section 3.1. The projected forces are subsequently imposed as a body force source term in the governing momentum equations, as detailed in Section 2.5.

A limitation inherent to the ALM is the overprediction of forces near the blade tip, where lift tends to increase towards the tip rather than going to zero as a blade resolved simulation and experiments show. [41] The Glauert tip loss correction accounts for this by applying a correction factor $F$ to the aerodynamic force at each blade element: [41]

$$F = \frac{2}{\pi} \arccos \left[ \exp\left( -\frac{1}{2} \frac{N_b(H-r)}{r \sin\phi} \right) \right] \tag{25}$$

where $r$ is the rotor radius, $N_b$ is the nr of blades, H is the rotor height and $\phi$ is the inflow angle. In turbinesFoam this correction ($F$) is applied as an optional setting referred to as `endEffects`, and is activated for all simulation cases in this study.

Although the ALM is well suited for wake farm simulations of this kind, it is not without limitations. In the ALM as implemented in TurbinesFoam, only the rotating blades are represented as body force lines. The tower and nacelle are not included in the model, as the original ALM was formulated to represent blade aerodynamics and their effect on wake formation. [36] The absence of the hub results in an overprediction of mean velocity and turbulence intensity at the wake centerline. [40] While tower effects can be approximated using additional actuator lines, this approach does not fully represent the tower as it does not replicate the stagnation pressure present in front of the tower, which would be present with a fully resolved geometry, limiting the accuracy gains relative to the additional computational cost. [42] For a comparative far-wake study such as this, the increased computational expense of including tower and hub elements is not justified by the marginal gains in accuracy. As all simulation cases share the same turbine representation, this simplification affects all cases equally and does not bias the relative comparison between wake control strategies.

# 3 Methods

The basis of the methodology for the study is the computational fluid dynamics (CFD) open source software, OpenFOAM. To model using the actuator line method (ALM), a library from GitHub called turbinesFoam is utilized. OpenFOAM version 2406, released June 2024, is run in an HPC environment.

## 3.1 Computational Setup

### 3.1.1 Domain & Boundary Conditions

All case simulations and computations are completed in a 6960 m x 1200 m x 990 m domain with three turbines in line. The distance between each turbine in the x-direction is 7 times the turbine's blade diameter (7D), which is 1680 m. The distance in the y-direction from the turbines to the left and right walls is 2.5D so that when cyclic conditions are applied to those walls the distance between each turbine in the y-direction is 5D, which equates to 1200 m. This turbine layout and spacing within the specified domain can be seen in figure 3, where turbines are positioned at x = 2400 m, x = 4080 m and x = 5760 m, respectively. This spacing is typical for offshore wind farms and is optimal for the least amount of inter-turbine interference in both directions while still optimizing the available area of the wind farm. [43] There is also a distance of 10D (2400 m) between the inlet and the first turbine to allow for a full development of the flow before reaching the turbine. The distance between the last turbine (T3) and the outlet is 5D (1200 m); for the wake to fully develop, a longer distance would be necessary. Although for the purposes of this study, it is not necessary to observe the behavior of the last turbine's wake fully, as it does not interfere with another turbine. One can study T3's performance characteristics with a partially developed wake.

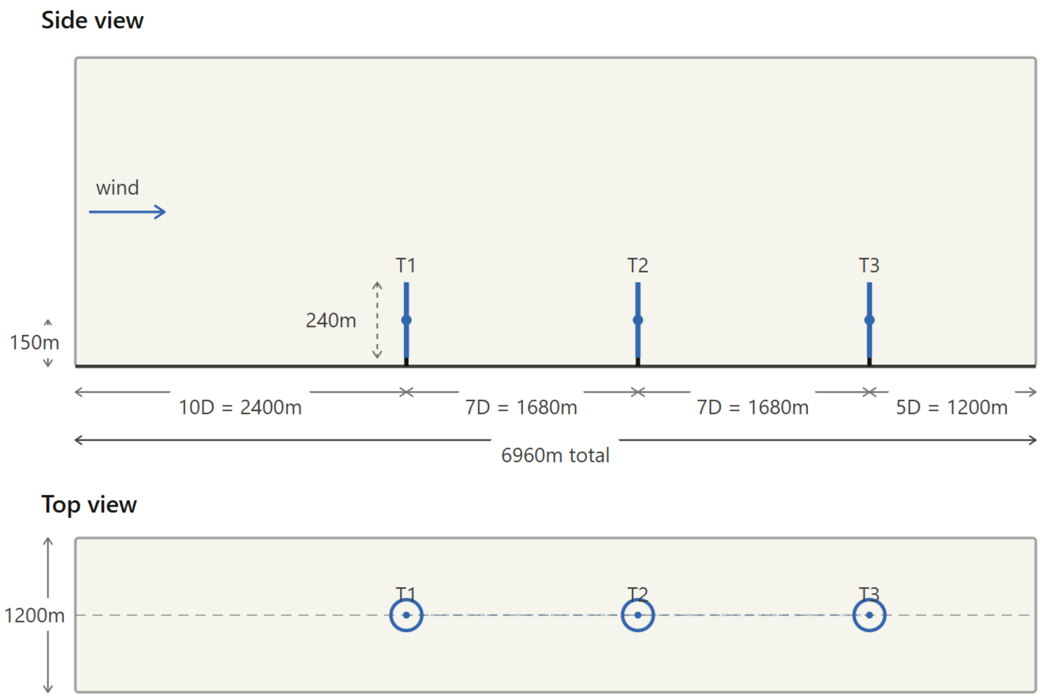


Figure 3: Domain layout, shown from top and side view with turbine positions and key dimensions. Figure generated using Claude.

Boundary conditions are set for all surfaces of the domain. The left and right sides of the domain have cyclic boundary conditions in order for the simulation to infinitely model columns of three turbines in the y-direction, which replicates a true wind farm environment. The bottom boundary has no-slip conditions for velocity and a zero pressure gradient. For $k$ at the bottom, the near-wall turbulence is modeled as a wall function of the local velocity instead of resolving the viscous sublayer near the sea surface. $\varepsilon$ in the near-wall region is set to maintain the log-law velocity profile. The top boundary uses a symmetric function that prevents any flow across the boundary and has gradients equal to zero. The inlet is well defined with a log-law neutral atmospheric boundary layer profile that uses equations (26), (27), and (28). From these equations, the velocity is coded to have a log-law function with the hub height velocity ending up at 10 m/s. For the turbulent kinetic energy, k, it is a fixed value calculated from equation (27), while $\varepsilon$ also follows the coded log-law function, equation (28), and pressure has a zero gradient. The prescribed inlet profile yields a hub-height turbulence intensity of approximately 4.3%, consistent with low-turbulence offshore atmospheric conditions [44]. Due to the defined inlet conditions, the pressure at the outlet has a fixed value of zero and the velocity, $k$, and $\varepsilon$ have a zero gradient. For these equations $Z_0$ is appropriately chosen as an adequate surface roughness length for an offshore landscape[45].

$$u^* = \frac{U\kappa}{\ln\left(\dfrac{z+z_0}{z_0}\right)} \tag{26}$$

$$k = \frac{u^{*2}}{\sqrt{C_\mu}} \tag{27}$$

$$\varepsilon(z) = \frac{u^{*3}}{\kappa\,(z+z_0)} \tag{28}$$

where: $z_0$ = surface roughness length = 0.0001m, $\kappa$ = von Kármán constant = 0.41, $C_\mu$ = model constant = 0.09.

### 3.1.2 Turbine Modeling

The turbine that is used for this study is the IEA 15 MW model which is a horizontal axis wind turbine (HAWT) designed by the National Renewable Energy Laboratory (NREL), the Technical University of Denmark (DTU), and University of Maine through the International Energy Agency (IEA) [44]. The essential design parameters and characteristics can be seen in table 1, and is designed to be built with a monopile foundation. The motivations for choosing this design are that the turbine's characteristics are publicly available and this turbine is considered to be a modernly large-sized design for offshore applications with a power output of 15 MW and a 240m rotor diameter. Therefore, in choosing to study this specific turbine design the goal of researching how effective wake management strategies are for today's large-scale offshore wind turbines is met. It should be noted that both hub and tower geometry are not simulated for any case, consistent with standard ALM practice as discussed in Section 2.7.

Table 1: Key design parameters and operating characteristics of the IEA 15 MW offshore reference wind turbine used as the baseline configuration in this study.[44]

| Parameter | Value | Unit |
|---|---|---|
| Turbine class | IEC Class 1B | - |
| Rotor diameter | 240 | m |
| Hub height | 150 | m |
| Rated wind speed | 10.59 | m/s |
| Design tip speed ratio | 9 | - |
| $Design\ C_p$ | 0.489 | - |
| $Design\ C_t$ | 0.799 | - |
| Power rating | 15 | MW |

The power output of each turbine is calculated from the simulated power coefficient using equation (3), where $U_\infty = 10m/s$ is the undisturbed freestream velocity prescribed at the inlet. Since turbinesFoam normalizes $C_p$ for all turbines using the $U_\infty$ as reference, the wake deficit experienced by downstream turbines is captured in the reduced $C_p$ values rather than through a modified reference velocity [46]. This is a valid approach to computing power output as the $C_p$ refers to the amount of wind power that a turbine can convert into mechanical work [5]. For yaw misalignment cases, the reported $C_p$ values are corrected by $cos^2(\gamma)$ before computing the power output as described in the upcoming Section 3.4.

As described in Section 2.7, the actuator line method is used to represent each turbine blade as a line where aerodynamic forces are placed along it. In turbinesFoam, the Gaussian smearing parameter is set to $\varepsilon = \varepsilon_{chord}$, scaling with local chord length to ensure consistent force distribution relative to the blade geometry. The Glauert tip loss correction is applied to all blade elements as described in Section 2.7.

The DTU FFA-W3 series of airfoils are used as a basis and optimized for this design. The design blade data is publicly available on a GitHub repository, and is used for all simulated turbine blades. Each turbine blade is discretised into 29 elements spanning r=2.0m to r=120m, with cord and twist distribution interpolated from the IEA-15-240-RWTAeroDyn15 blade file [44]. This blade element data discretiztion is shown in figure 5. The technical report for the IEA 15 MW turbine [44] is also used for validation of the computational setup and the blade data. The validation results can be seen in table 2 with the main takeaway that the simulation shows good agreement with the design values due to all error percentages being below 10%. However, it should be noted that the IEA 15MW turbine has a rated power of 15MW at 10.59m/s, so at 10m/s as seen in figure 4, the actual power production is lower than 15 MW, closer to 13-14 MW thus, the error percentage is lower between the simulation and design value than the table suggests. No experimental wake data is available for the IEA 15 MW at this scale, so validation is only done against the design values.

Table 2: Validation Results, simulation values gathered from the 2-turbine simulation, case 3.

| Parameter | Design Value | Simulation Value | Percent Error (%) |
|---|---|---|---|
| $C_p$ | 0.489 | 0.4898 | 0.12 |
| $C_t$ | 0.799 | 0.7546 | 5.5 |
| Power rating (MW) | 15 | 13.57 | 9.53 |

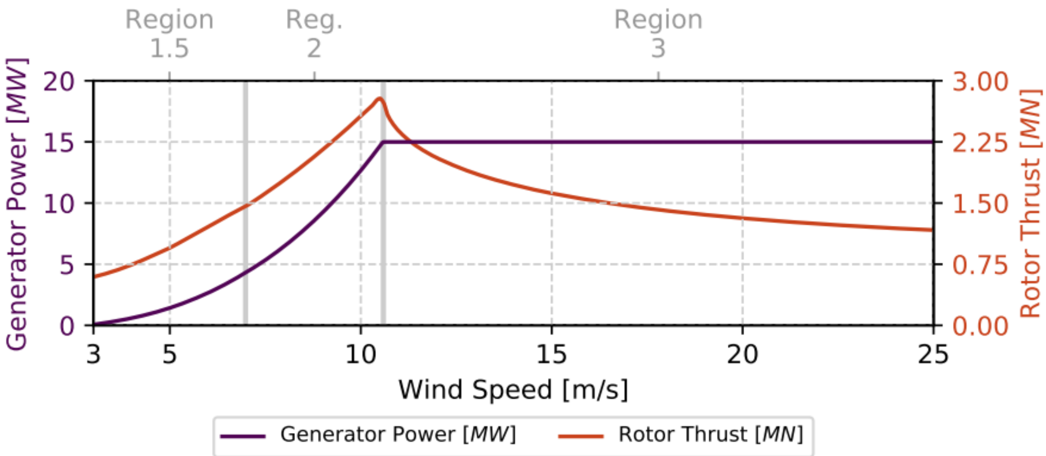


Figure 4: Generator power output and rotor thrust versus wind speed for the IEA 15 MW reference turbine across its three operating regions. Adapted from Gaertner et al. [44].

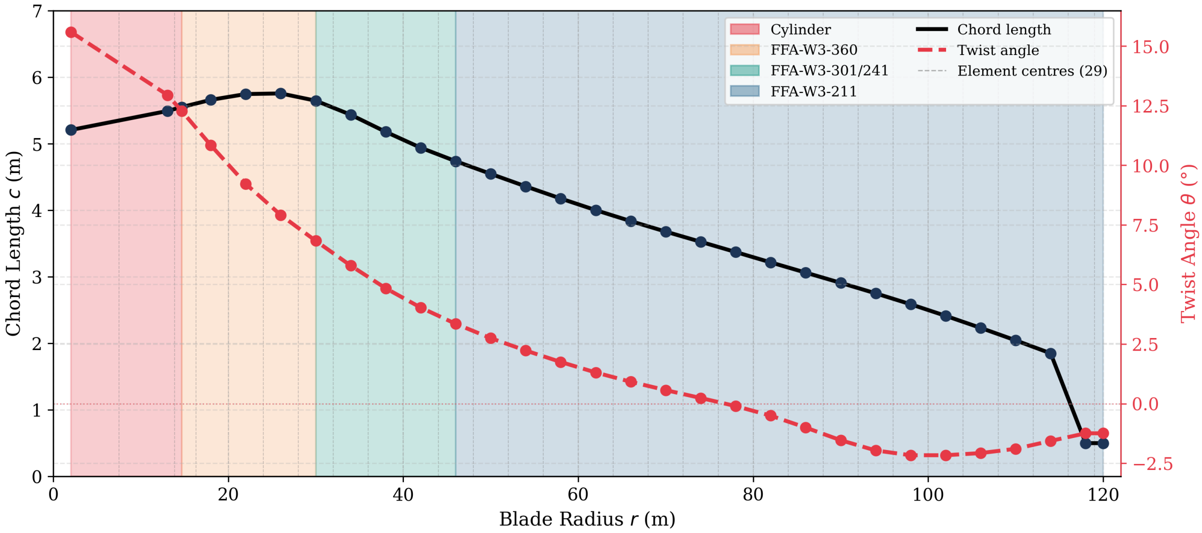


Figure 5: Chord length (left y-axis) and twist angle (right y-axis) along the blade radius, showing the spanwise airfoil regions.

Lastly, when it comes to the blade design by Gaertner et al. [44], it is important to note that the NREL-IEA 15 MW blade operates at a design tip-speed ratio of 9, and the design values shown in table 2 are for this TSR. In contrast, a QBlade BEM analysis is performed that shows the optimal TSR for this turbine is  10.4 as seen in figure 6. This means the design conditions are not synonymous with optimal conditions, and is important to keep in mind as certain wake control methods may produce unexpected results. The reason for this choice in design is that there is a maximum tip speed limitation of 95 m/s. Thus for a rated wind speed of 10.59 m/s, the maximum TSR is 9 [44]. This tip speed limit is to adhere to noise regulations, structural load limitations, and feasibility of the current industry. For such a large turbine as this, this limit is a strict constraint, and for smaller sized turbines this would not be so restrictive. As turbine blade design continues to progress, the possibility of exceeding a tip speed of 95 m/s for large-scale turbines may increase.

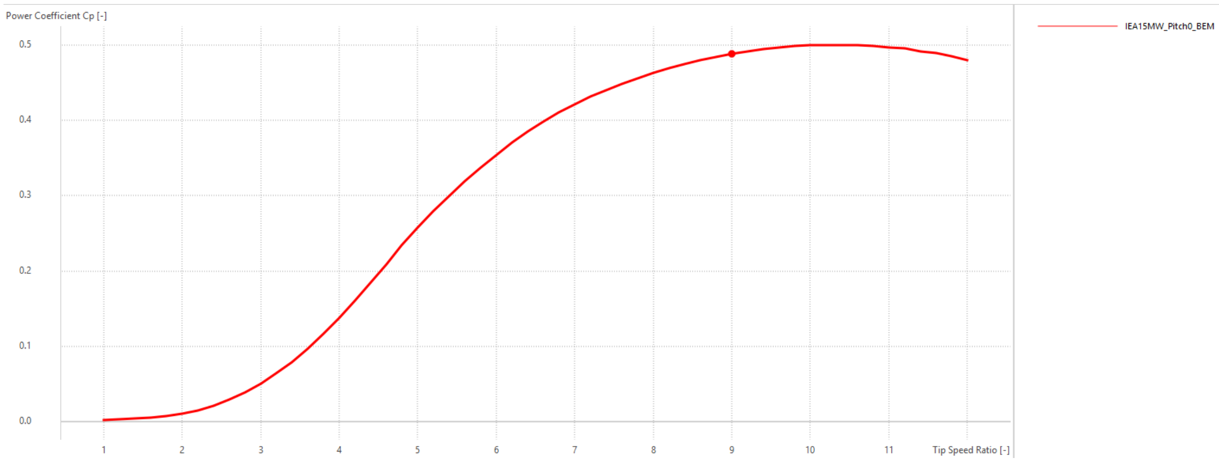


Figure 6: Power coefficient $C_p$ as a function of tip speed ratio $\lambda$ for the NREL-IEA 15 MW turbine at collective pitch angle $\theta_p = 0°$, obtained from a BEM analysis in QBlade using the IEA-15-240-RWT blade geometry and FFA-W3 airfoil polars at $Re = 1 \times 10^7$. The marked point at $\lambda = 9$ indicates the design operating point, and the aerodynamic optimum occurs at $\lambda \approx 10.4$.

### 3.1.3 Mesh

The mesh consists of a fully structured background mesh generated using blockMesh with a grid of 140 x 60 x 30 in the streamwise, spanwise, and vertical directions. This grid consists of base cell dimensions of 49.7 m x 20 m x 33 m and 3,689,504 cells. Refinement regions are used for the rotor and wake areas, where it is crucial for the mesh to be finer for numerical accuracy. SnappyHexMesh refines the base mesh and snaps to boundary points with a refinement level 3 in a cylindrical region about the rotor of each turbine and with refinement level 2 in a rectangular region encapsulating the wake region behind each turbine, as seen in figure 7. The transition sections between refinement regions and the background mesh produce segments of unstructured mesh, but the rest of mesh remains predominantly hexahedral and structured. This transitional region consists of one boundary layer between the refinement areas and the background mesh.

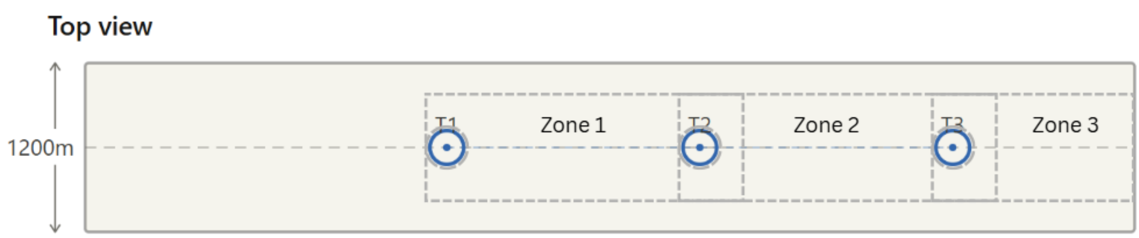


Figure 7: Mesh refinement zones, 140m radius refinement zone around each rotor with refinement level 3. 1920m x 600m x 400m refinement zone for each wake zone with refinement level 2. Figure generated using Claude and Canva.

The level of refinement in the wake and rotor regions is determined through a mesh sensitivity study outlined in table 3. Figure 8 shows that case 4 with a background mesh of (106 x 60 x 30) with base cell dimensions of 49.7 m x 20 m x 33 m and levels 3 and 2 for the rotor and wake regions, respectively, produce the coarsest possible mesh while still maintaining accurate results. The sensitivity analysis shows a 4.6% variation in $C_p$ between case 4 and the finest mesh, which is less than ideal. This means the result is not fully mesh-converged, but a finer mesh is not feasible due to the large domain size and thus long run times. A mesh finer than case 6 would have a run time that exceeds the 7 day limit that comes with using a SLURM job scheduler. Despite this, the chosen mesh produces valid results while having the lowest computational cost possible. The mesh sensitivity analysis is performed with an adjusted mesh and domain that models only two rows of turbines to save time and computational resources. After the analysis, the mesh and domain are altered for all wake control cases to model three rows of turbines for the final simulation. The same base cell dimensions as mentioned before are maintained from the mesh sensitivity case after extending the domain.

Table 3: Summary of the mesh sensitivity analysis cases used to assess numerical grid convergence, including background mesh resolution, rotor-region refinement level, wake-region refinement level, and total computational cell count.

| Case | Background mesh | Rotor level | Wake level | Number of cells |
|---|---|---|---|---|
| 1 | (53x30x15) | 2 | 1 | 51,689 |
| 2 | (53x30x15) | 3 | 2 | 268,528 |
| 3 | (106x60x30) | 2 | 1 | 406,848 |
| 4 | (106x60x30) | 3 | 2 | 2,122,926 |
| 5 | (212x120x60) | 2 | 1 | 3,260,636 |
| 6 | (212x120x60) | 3 | 2 | 16,790,320 |

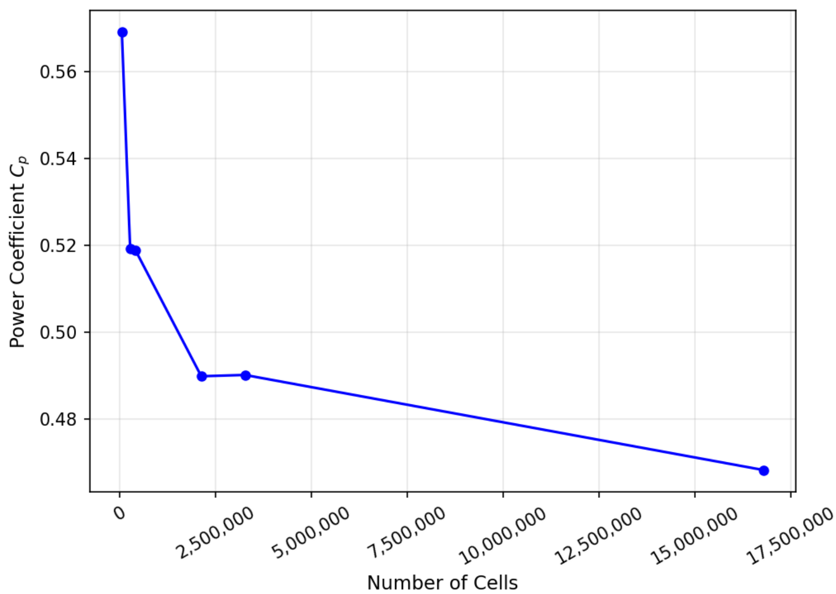


Figure 8: Power coefficient $C_p$ of turbine 1 as a function of total mesh cell count for the five mesh sensitivity cases summarised in Table 3. Results are time-averaged over $t > 250$ s. The curve shows rapid convergence between cases 1 and 3, with a 4.6% variation in $C_p$ between case 4 (2,122,926 cells) and the finest mesh, case 6 (16,790,320 cells).

### 3.1.4 Simulation Parameters

For the time control computational set up, the pimpleFoam application is used. The simulation's start time is at 0 and ends at time 600s. This calculates to around 72 revolutions of the turbine which is sufficient to reach convergence as can be seen in figure 9, and the full development of the wakes, where TSR = 9, U = 10 m/s, and R = 120 m. The results of the model are time averaged from 300 to 600s. The time step ($\Delta t$) is 0.04 s which calculates to 1.25° of rotation per time step. For the output, every 100 time steps, or every 4 seconds, the flow field is saved to the disk.

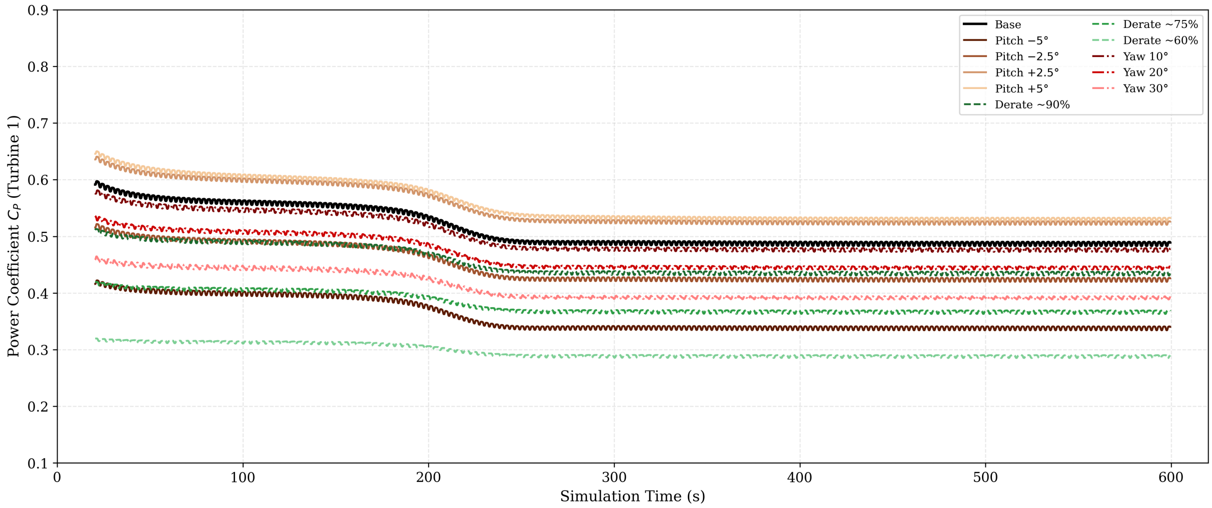


Figure 9: Time history of turbine 1 power coefficient $C_P$ for all simulation cases. All cases reach statistically stationary conditions.

For time discretisation, the simulation uses the first-order implicit (Euler) scheme which is standard practice for RANS turbulence modeling. A second-order accurate finite volume discretisation is used spatially as velocity and pressure are solved sequentially with a segregated solver. The simulation uses a PIMPLE solver which is a combination of the SIMPLE and PISO algorithms, specifically for the pressure-velocity coupling the PISO corrector loop is utilized. RANS $k-\varepsilon$ turbulence modeling is used for the simulation. $k-\varepsilon$ model is selected for its robustness and computational efficiency at high Reynolds numbers [35]. All simulations are run in parallel using 48 CPU cores via MPI domain decomposition on the LUNARC Aurora HPC cluster.

## 3.2 Axial Induction Control via Pitch

In order to observe the full effects that AIC via blade pitch control has on a wind farm with IEA 15 MW turbines, both positive and negative pitch must be modeled. Only the blade pitch changes with each case, so all other parameters, such as TSR and yaw alignment, do not deviate from the design values seen in table 1 for these cases. The range of blade pitch angle adjustments can be seen in table 4 and spans from -5° to +5° with 2.5° increments, where 0° pitch is the base case with the original element data of the IEA 15 MW turbine. Cases 1 and 2 pitch toward stall, which increases the angle of attack due to the pitch angle decreasing. Thus, cases 3 and 4 pitch toward feather by positively pitching and decreasing the angle of attack for the blade.

Table 4: AIC via blade pitching case setup.

| Case | Pitch offset (°) |
|---|---|
| 1 | -5 |
| 2 | -2.5 |
| 3 | 0 |
| 4 | +2.5 |
| 5 | +5 |

Blade pitching with CFD is done by applying uniform twist offsets to the original element data of the IEA 15 MW turbine for only turbine 1, T1. The other two downstream turbines maintain the original element data and twist orientation throughout every case. Thus any observed changes in performance values for T2 and T3 are a result only from the downstream affects of pitching T1. As mentioned in section 2.4, pitch control can be done via collective or individual blade pitching. The method for this study uses collective blade pitching, meaning all three blades of T1 have the same pitch control effects applied. Something to note for the sake of convention protocol is when using turbinesFoam and applying a positive twist offset this actually increases the angle of attack. The conclusion from this is: if the aim is to apply a positive pitch (pitch toward feather) on the blades which decreases the angle of attack (cases 4 and 5), then it is necessary to apply a negative twist offset when using turbinesFoam. Table 4 appropriately shows the *pitch offset angles*, the standard wind turbine pitch convention, which is the opposite of the *twist offset angles* applied in turbinesFoam.

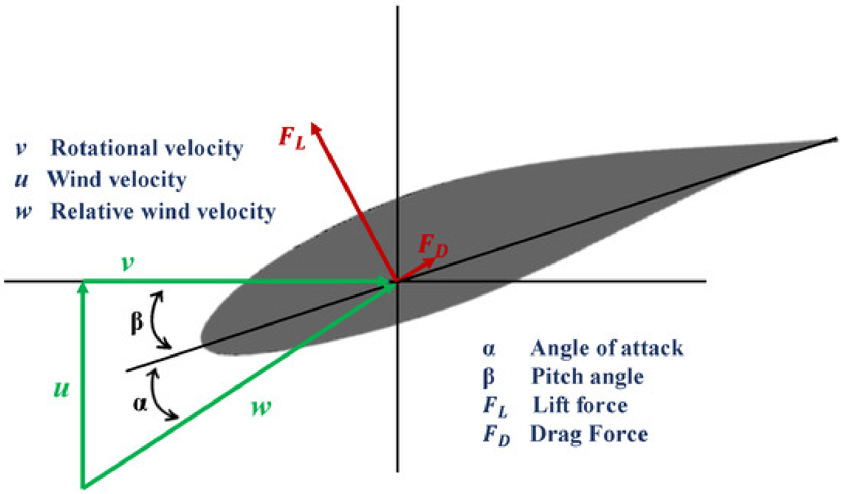


Figure 10: Schematic illustration of the aerodynamic forces and velocity components acting on a wind turbine blade element. The relative wind velocity $w$ is the vector sum of the rotational velocity $v$ and the wind velocity $u$. Adapted from Elkodama et al.[47]

The aerodynamic lift and drag forces acting on each blade element are calculated as:

$$F_L = \frac{1}{2}\rho V_{\mathrm{rel}}^2 \, c \, \Delta r \cdot C_L(\alpha) \tag{29}$$

where $\rho$ is the air density, $V_{\mathrm{rel}}$ is the magnitude of the relative velocity seen by the blade element, $c$ is the local chord length, $\Delta r$ is the spanwise element length, and $C_L(\alpha)$ and $C_D(\alpha)$ are the lift and drag coefficients obtained from the FFA-W3 airfoil polar data as functions of the local angle of attack $\alpha$.

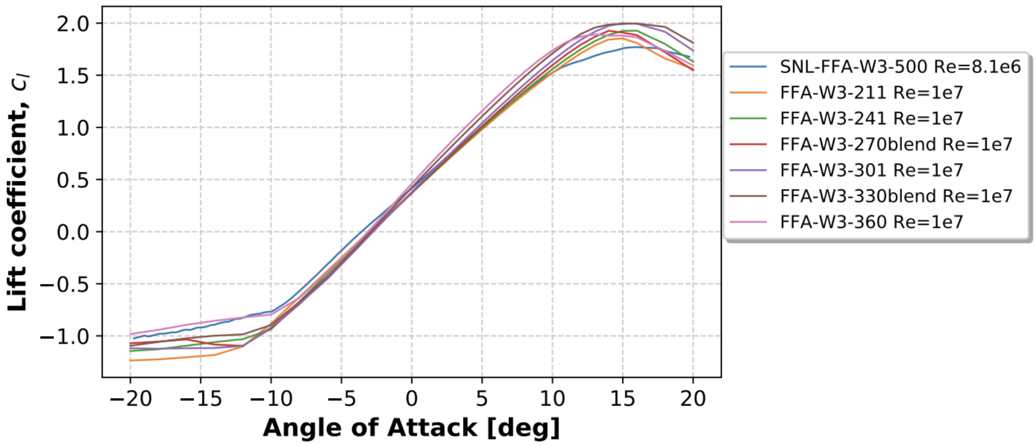


Figure 11: Lift coefficient $C_L$ as a function of angle of attack for the FFA-W3 airfoil series used in the NREL-IEA 15 MW blade, at Reynolds number $Re = 1 \times 10^7$. The profiles range from the thicker root sections (FFA-W3-360) to the thinner tip sections (FFA-W3-211), with blended profiles at intermediate thicknesses. Reproduced from Gaertner et al. [44].

Equation (6), as denoted in Section 2.1, proves that increasing pitch angle ($\theta_p$) does indeed decrease the angle of attack ($\alpha$) while decreasing $\theta_p$ increases $\alpha$. This can be conceptually visualized using figure 10 as well. Knowing this relation leads to the question of how changing angles of attack affects the performance values for the turbine. The lift coefficient ($C_L$) is a function of $\alpha$, and since $C_L$ changes, the lift force does as well as seen from equation (29). Using figure 11 reveals that as the angle attack decreases due to a pitch angle increase, the lift coefficient also decreases alongside $F_L$. The tangential component of $F_L$ causes rotor rotation for the turbine, so there is a direct relation between affects on $F_L$ and the rotor torque [48]. The rotor torque thus impacts the power coefficient $C_P$ and power output for the turbine [48]. Therefore, it is expected that as the pitch angle decreases (pitch toward stall), the angle of attack will increase, increasing rotor torque and power output for turbine 1. While the pitch angle increases (pitch toward feather), the angle of attack will decrease, as well as the power output for T1.

## 3.3 Axial Induction Control via Derating

As described in Section 2.4, AIC via derating operates the turbine at a fixed percentage of its rated power output. For this study, derating was implemented by reducing the TSR of turbine 1, T1, while maintaining a fixed blade pitch angle of 0°. In turbinesFoam, generator torque is not directly modeled; instead, the rotor angular velocity is prescribed through the tip speed ratio. TSR reduction, therefore, serves as a CFD approximation of generator torque derating. The TSR directly controls the rotor angular velocity through:

$$\omega = TSR\frac{U_\infty}{R} \tag{30}$$

Reducing TSR therefore reduces the rotor speed and thus extracts less momentum from the flow, resulting in a weaker wake deficit. For this study, only T1 is derated in each case; T2 and T3 maintain the design TSR of 9.0 and a fixed blade pitch of 0° throughout.

Three derating levels are investigated. The target power coefficient for each case is defined as:

$$C_{P,target} = f \times C_{P,opt} \tag{31}$$

where $f$ is the intended derating fraction and $C_{P,opt} = 0.489$ is the IEA-15MW design optimum power coefficient. [44] For the intended 90% and 80% cases, TSR values are initially selected from the rotor performance table `Cp_Ct_Cq.IEA15MW.txt` at pitch = 0°, choosing the TSR producing the closest $C_P$ to each target. This yields TSR= 7.0 for the intended 90% case and TSR= 6.0 for the intended 80% case.

However, the ALM simulation produces a higher base case power coefficient of $C_{P,base} = 0.4876$ than the BEM optimum of 0.4697, and the simulated $C_P$ at reduced TSR drops more steeply than the BEM table predicts due to the fixed pitch assumption. As a result, the achieved derating levels relative to the simulated base case differ significantly from the intended values where TSR= 7.0 yields an actual derating of 75.1% and TSR= 6.0 yields 59.1%, rather than the intended 90% and 80%.

To obtain a case closer to the intended 90% derating, the required TSR is estimated by linear interpolation between the two closest simulated operating points. Targeting $C_{P,target} = 0.90 \times 0.489 = 0.4401$ with $\mathrm{TSR}_1 = 9.0$, $C_{P,1} = 0.489$ and $\mathrm{TSR}_2 = 7.0$, $C_{P,2} = 0.3673$ yields an interpolated TSR of 8.2, rounded to TSR= 8.0 for simplicity. The resulting simulated $C_P = 0.4353$ corresponds to an achieved derating of 89.0% relative to the design $C_{P,opt}$. The three derating cases and their achieved derating levels are summarised in Table 5.

Table 5: AIC via derating case setup. Intended derating levels are defined relative to the design $C_{P,opt} = 0.489$ [44]. Achieved derating is relative to the simulated base case $C_{P,opt} = 0.489$.

| Case | TSR ) | Simulated $C_P$ | Achieved derating (%) |
|---|---|---|---|
| Base | 9.0 | 0.4876 | 100 |
| 1 | 8.0 | 0.4353 | 89.0 |
| 2 | 7.0 | 0.3673 | 75.1 |
| 3 | 6.0 | 0.2889 | 59.1 |

The specific derating levels investigated are consistent with those of Kazda et al. [49], who tested 62.5%, 75%, and 87.5% of the optimal power coefficient using the same fixed-pitch TSR reduction approach. This thesis studies comparable derating levels from 60 to 90%, covering a similar range. It should be noted that in a real wind turbine, generator torque derating would typically include blade pitch adjustment to maintain operation along the optimal $C_p - TSR$ curve. In the present CFD implementation, this was not done, meaning the rotor operates away from the aerodynamic optimum at reduced TSR.

## 3.4 Yaw Control

As described in Section 2.4, yaw control involves steering the wake away from downstream turbines in order to increase total farm production. For this study three yaw cases are investigated where the yaw misalignment is applied by rotating the rotor axis by 10°, 20° and 30° while maintaining the freestream direction, as summarized in table 6. These yaw angles were selected as they cover the range most commonly investigated in literature [50] [12]. The yaw misalignment is only applied to turbine 1, T1, with T2 and T3 remaining aligned with the freestream at TSR = 9. In turbinesFoam, yaw misalignment is implemented by rotating the rotor axis vector by angle $\gamma$ from the streamwise direction:

$$\mathbf{axis} = (\cos\gamma,\ \sin\gamma,\ 0) \tag{32}$$

While the freestream velocity vector is simultaneously set to:

$$\mathbf{U_{fs}} = (U_\infty \cos^2\gamma,\ U_\infty \cos\gamma \sin\gamma,\ 0) \tag{33}$$

which has a magnitude of $|U_{fs}| = U_\infty cos\gamma$. This correction of the velocity is necessary because turbinesFoam prescribes rotor angular velocity as:

$$\omega = \frac{\text{TSR} \times |\mathbf{U}_{fs}|}{R} \tag{34}$$

Therefore, setting $|U_{fs}| = U_\infty cos\gamma$ ensures the rotor speed is correctly reduced under yaw misalignment. If the freestream velocity were to be left at 10 m/s as prescribed, then in turbinesFoam, the rotor would spin at the same speed as an unyawed case. This was confirmed by inspecting the turbinesFoam source code [46]. It should be noted that turbinesFoam normalises the $C_p$ by $|U_{fs}|^2$ instead of $U_\infty^2$. Thus the reported $C_p$ values for yawed cases need to be corrected by a factor of $cos^2(\gamma)$ to get the true $C_p$ relative to the undisturbed wind speed:

$$C_{P,true} = C_{P,reported} \times \cos^2(\gamma) \tag{35}$$

The same correction is needed for $C_t$ as it also normalised by $|U_{fs}|^2$ instead of $U_\infty^2$.

$$C_{t,true} = C_{t,reported} \times \cos^2(\gamma) \tag{36}$$

Table 6: Yaw control case setup. The rotor axis is rotated by angle $\gamma$ and the freestream velocity magnitude is reduced to $U\cos(\gamma)$ to correctly scale rotor angular velocity under yaw misalignment.

| Case | Yaw angle $\gamma$ (°) | Rotor axis $(x, y, z)$ | $\lvert\mathbf{U}_\infty\rvert$ (m/s) |
|---|---|---|---|
| Base | 0 | (1.000, 0.000, 0) | 10.000 |
| 1 | 10 | (0.985, 0.174, 0) | 9.848 |
| 2 | 20 | (0.940, 0.342, 0) | 9.397 |
| 3 | 30 | (0.866, 0.500, 0) | 8.660 |

As mentioned in Section 3.1, cyclic boundary conditions are placed on the side walls of the domain. The cyclic boundary conditions in the lateral direction represent an infinite array of turbine columns. Under yaw misalignment, the deflected wake passes through the cyclic boundary and reenters the domain, physically representing the interaction between adjacent turbine columns in a wind farm, consistent with the behavior of the intended farm-level simulation.

# 4 Results

This chapter presents the CFD simulation results for the three wake control strategies investigated in this thesis: axial induction control via pitch, axial induction control via derating, and yaw control. All results are presented relative to a baseline case representing standard turbine operation without wake control. For each strategy the results focus on three key metrics: total farm power output, wake velocity deficit, and turbulence intensity distribution downstream of the controlled turbine. These metrics directly address the research questions outlined in Section 1.5.

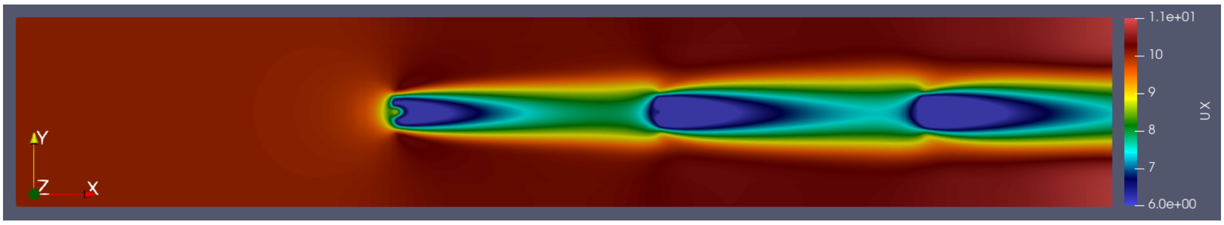


Figure 12: Normalised streamwise velocity $U_x$ at hub height ($z = 150$ m) for the base case. Flow direction is left to right.

## 4.1 Axial Induction Control via Pitch

In this section, results for axial induction control implemented via pitching on the upstream turbine T1 will be presented. As mentioned in the methods section 3.2, the turbine's blade pitch angle was adjusted for four separate angles, $-5°, -2.5°, +2.5°$ and $+5°$. The following results examine how, pitching towards stall or feather affects farm power output, wake velocity profiles and turbulence intensity downstream.

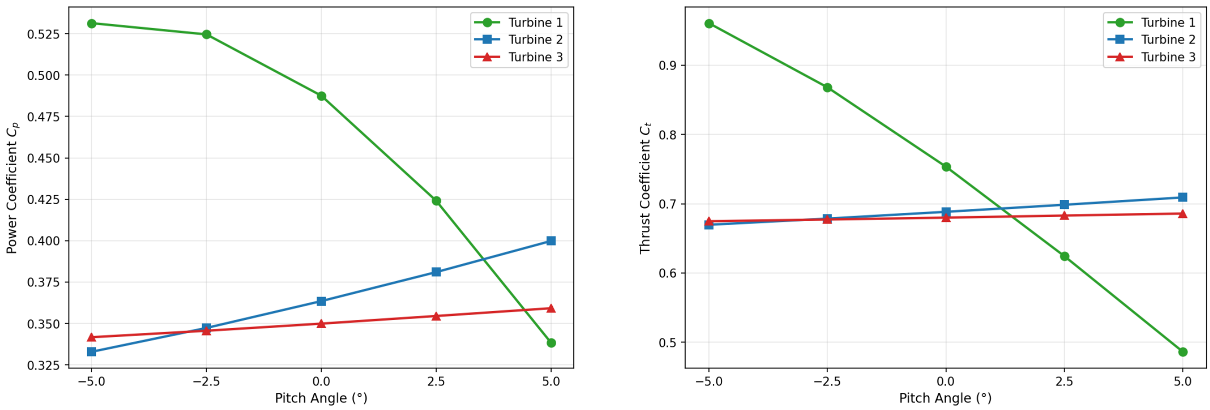


(a) $C_p$ per turbine for each pitching case.

(b) $C_t$ per turbine for each pitching case.

Figure 13: Time-averaged power and thrust coefficients for each turbine across the AIC via pitch cases, averaged over t>300s, where pitch angle = 0° corresponds to the baseline case.

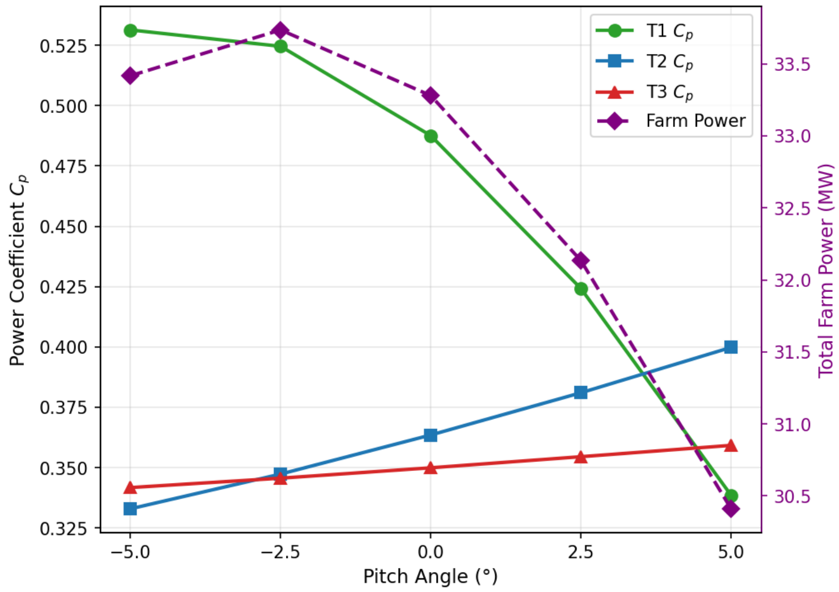


Figure 14: Power coefficient $C_p$ per turbine (left y-axis) and total farm power output (right y-axis) for each pitching case, time-averaged over t>300s, where pitch angle = 0° corresponds to the baseline case.

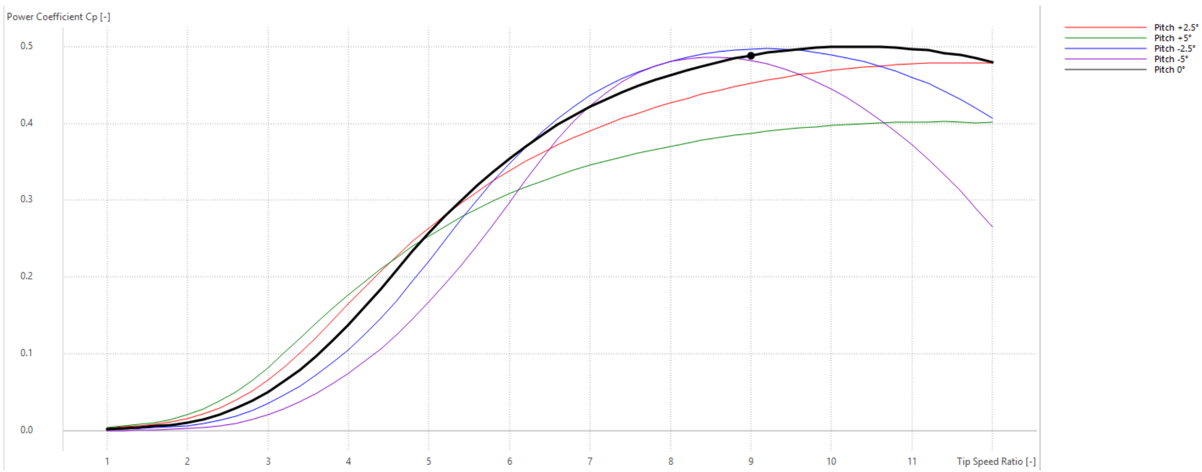


Figure 15: Computed $C_P$–$\lambda$ curves for blade pitch angles of −5°, −2.5°, 0°, +2.5°, and +5° with QBlade BEM analysis, showing the shift in peak power coefficient and optimal operating tip speed ratio with blade pitch adjustment.

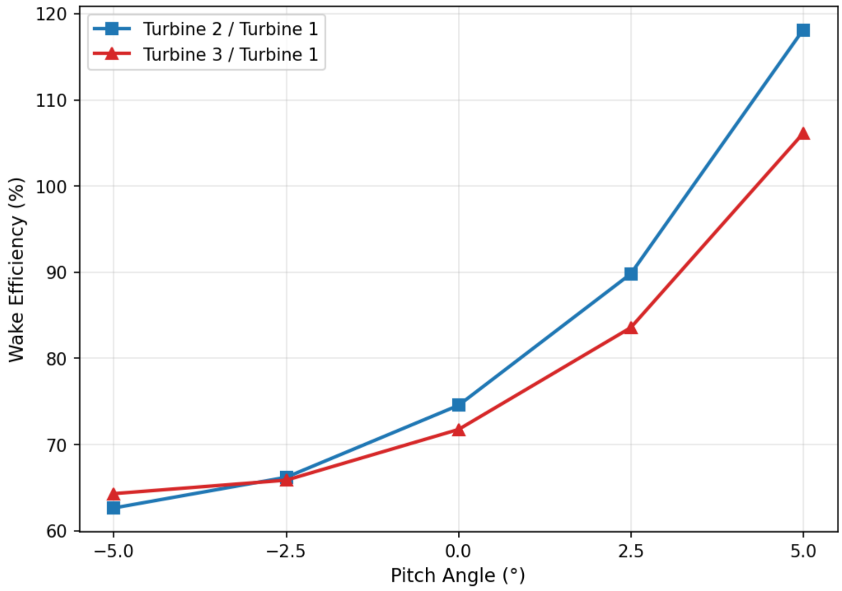


Figure 16: Wake efficiency, defined as the power ratio of each downstream turbine relative to T1, for each pitching case, where pitch angle = 0° corresponds to the baseline case.

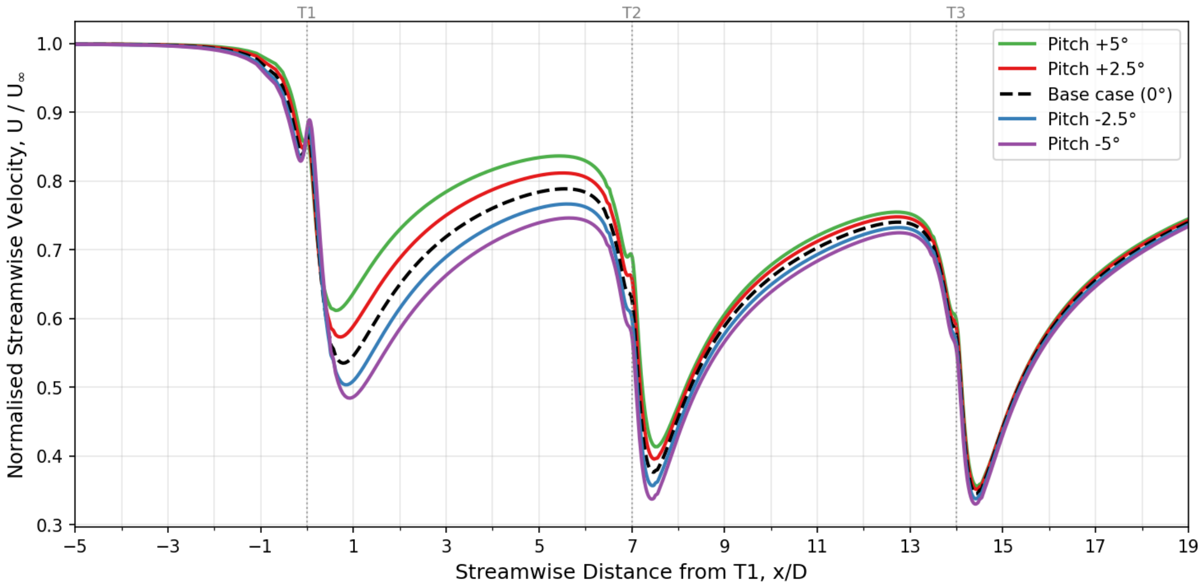


Figure 17: Normalised streamwise velocity $U/U_\infty$ along the farm centerline as a function of streamwise distance from T1 for each pitching case. Vertical dashed lines indicate the streamwise positions of T1, T2, and T3.

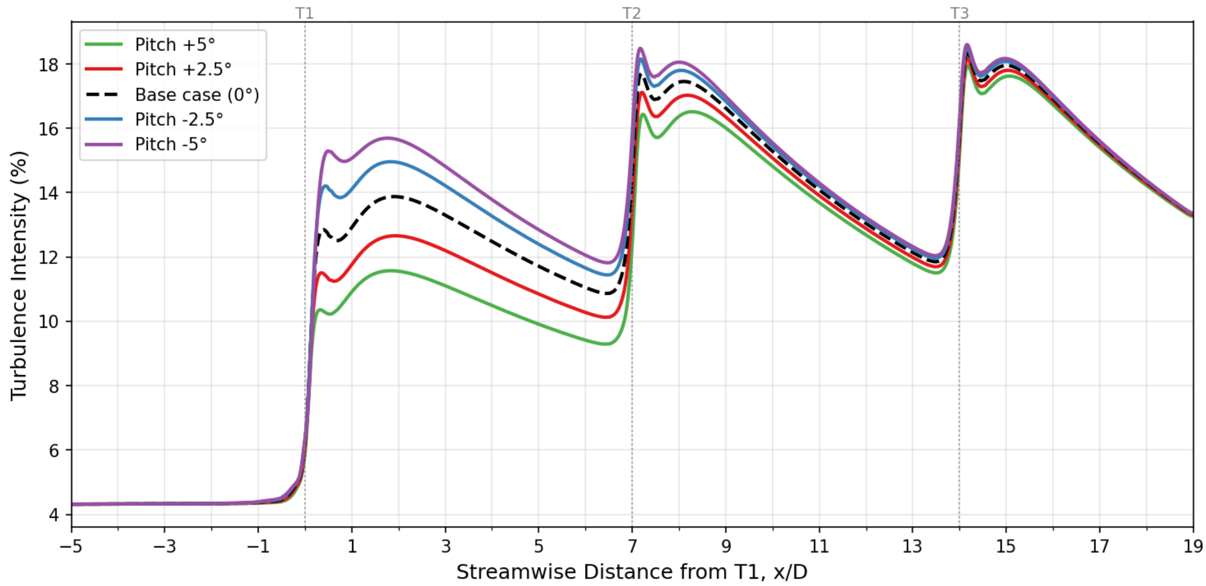


Figure 18: Streamwise turbulence intensity distribution along the farm centerline as a function of streamwise distance from T1 for each pitching case. Vertical dashed lines indicate the streamwise positions of T1, T2, and T3.

## 4.2 Axial Induction Control via Derating

In this section, results for axial induction control implemented via generator torque derating on the upstream turbine T1 will be presented. As mentioned in the methods section 3.3, the turbine was derated to 90%, 75% and 60% of rated power, reducing $C_t$ by operating the tip speed ratio at TSR = 8, 7 and 6, respectively. The following results examine how this curtailment affects farm power output, wake velocity profiles and turbulence intensity downstream.

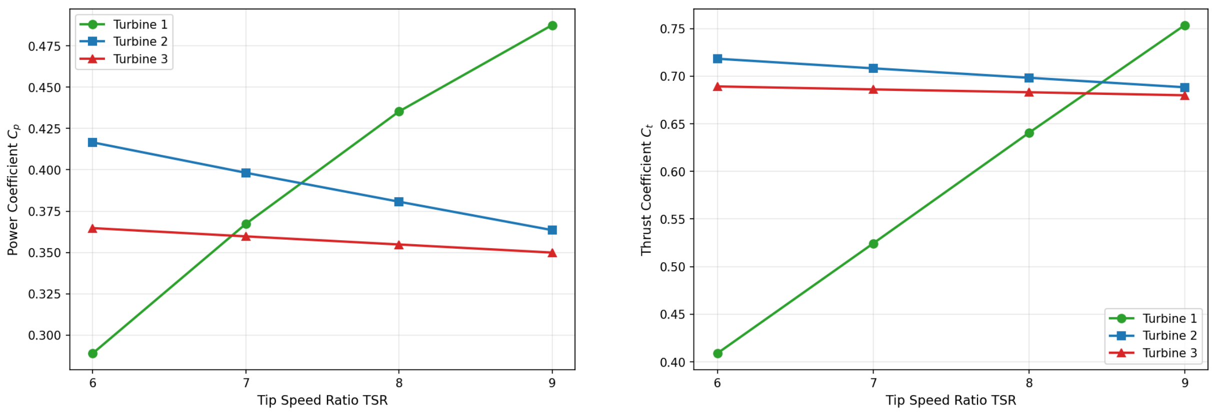


(a) $C_p$ per turbine for each derating case.

(b) $C_t$ per turbine for each derating case.

Figure 19: Time-averaged power and thrust coefficients for each turbine across the AIC derating cases, averaged over t>300s, where TSR = 9 corresponds to the baseline case.

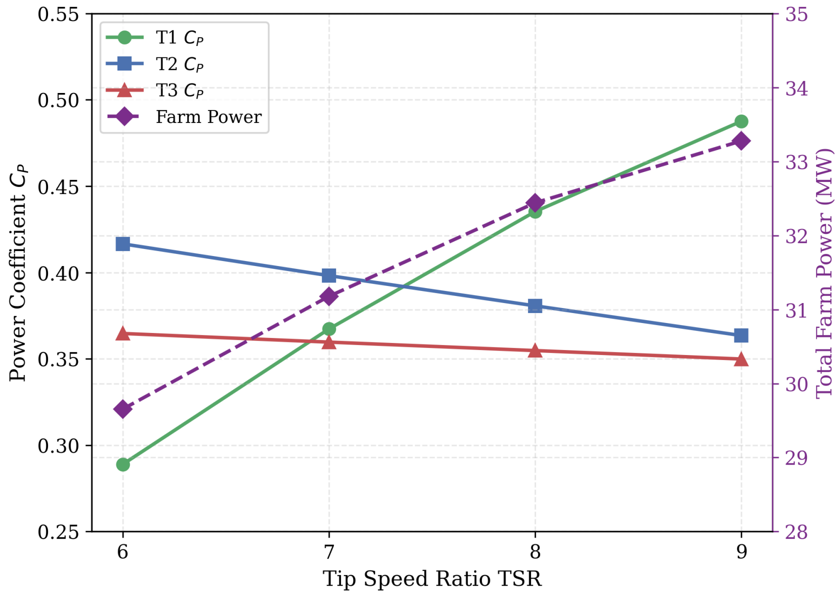


Figure 20: Power coefficient $C_p$ per turbine (left y-axis) and total farm power output (right y-axis) for each derating case, time-averaged over t>300s, where TSR = 9 corresponds to the baseline case.

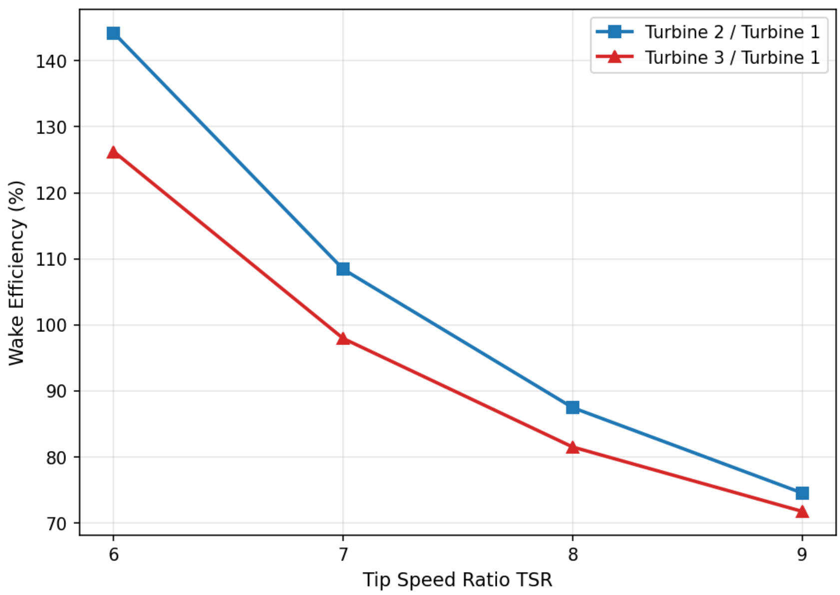


Figure 21: Wake efficiency, defined as the power ratio of each downstream turbine relative to T1, for each derating case, where TSR=9 corresponds to the baseline case.

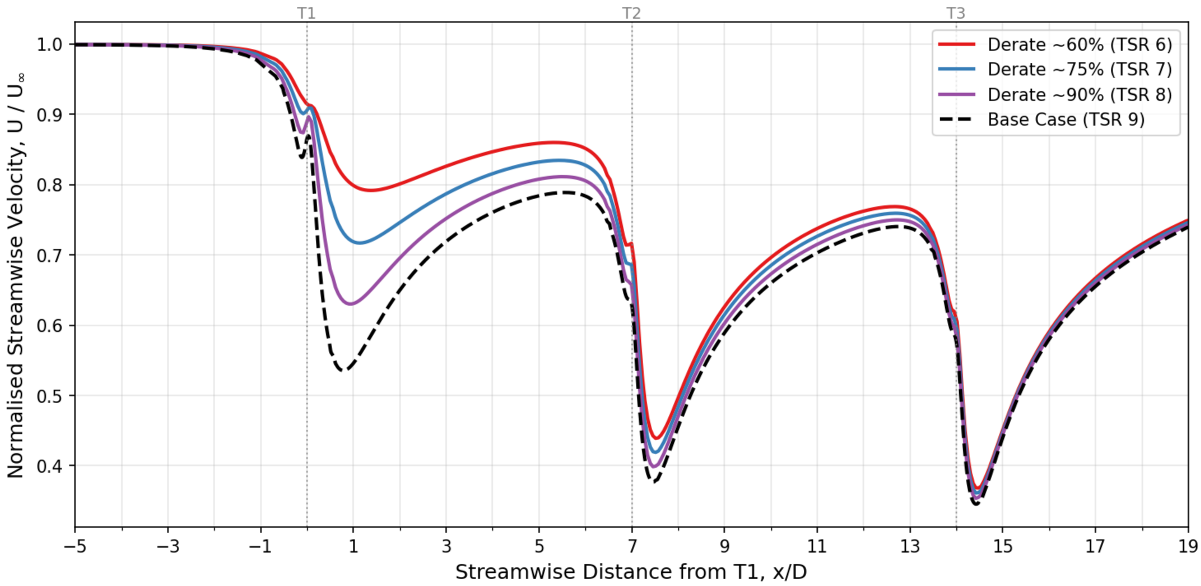


Figure 22: Normalised streamwise velocity $U/U_\infty$ along the farm centerline as a function of streamwise distance from T1 for each derating case, where base case TSR=9. Vertical dashed lines indicate the streamwise positions of T1, T2, and T3.

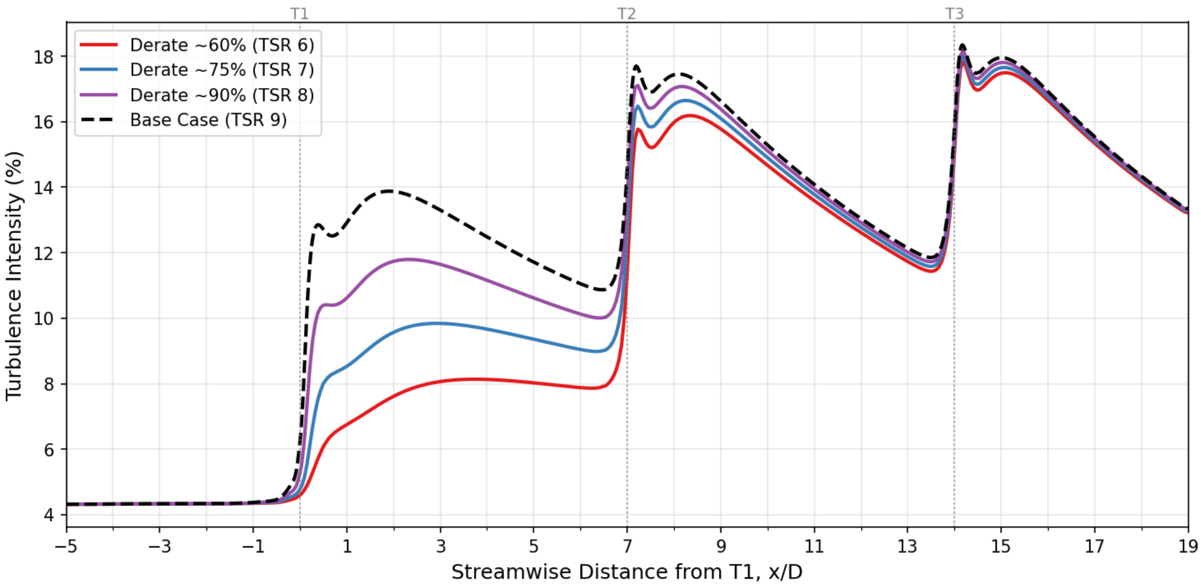


Figure 23: Streamwise turbulence intensity distribution along the farm centerline as a function of streamwise distance from T1 for each derating case, where base case TSR=9. Vertical dashed lines indicate the streamwise positions of T1, T2, and T3.

## 4.3 Yaw Control

In this section, the results for yaw control implementation on the upstream turbine T1 will be presented. As mentioned in the methods section 3.4, the rotor axis was misaligned with the incoming flow by $\gamma = 10°, 20°$ and $30°$, deflecting the wake laterally away from the downstream turbines. The following results examine how this deflection affects farm power output, wake velocity profiles and turbulence intensity at the downstream rotors.

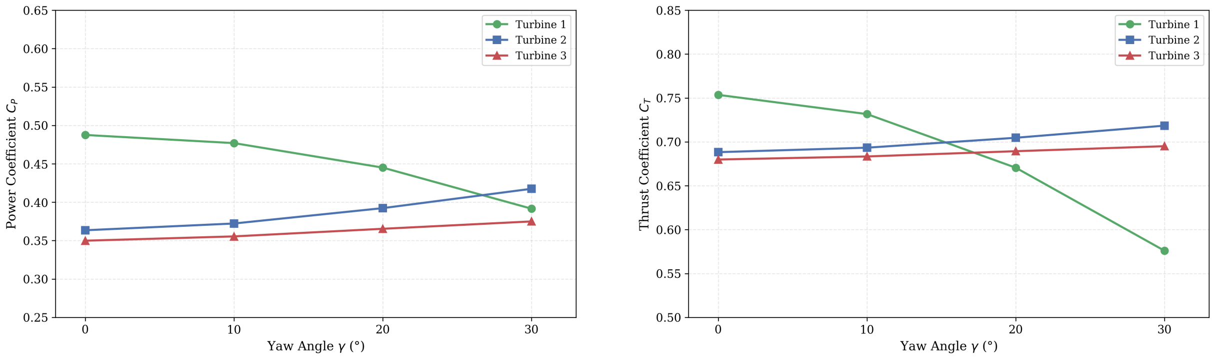


(a) $C_p$ per turbine for each yaw control case.

(b) $C_t$ per turbine for each yaw control case.

Figure 24: Time-averaged power and thrust coefficients for each turbine across the yaw control cases, averaged over t>300s, where $\gamma = 0°$ corresponds to the baseline case.

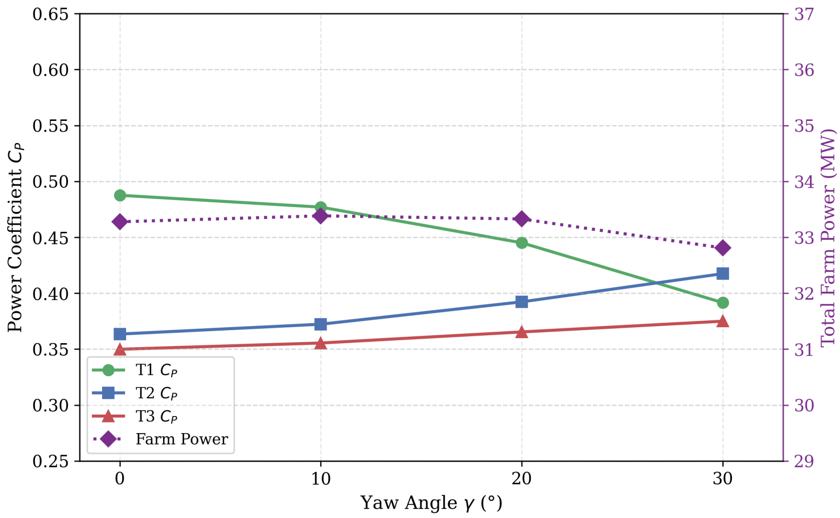


Figure 25: Power coefficient $C_p$ per turbine (left y-axis) and total farm power output (right y-axis) for each yaw control case, time-averaged over t>300s, where $\gamma = 0°$ corresponds to the baseline case.

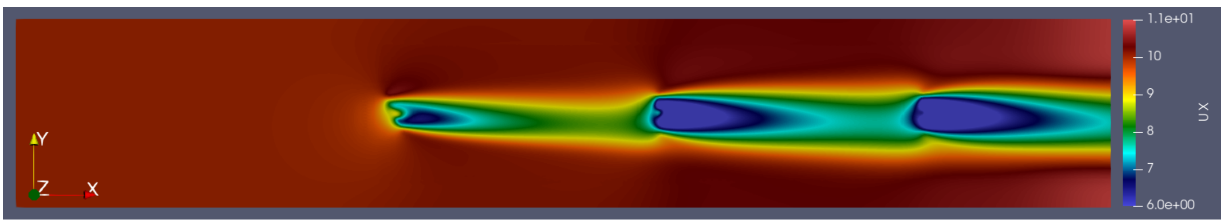


Figure 26: Normalised streamwise velocity $U_x$ at hub height ($z$ = 150 m) for the yaw 30° case. Flow direction is left to right.

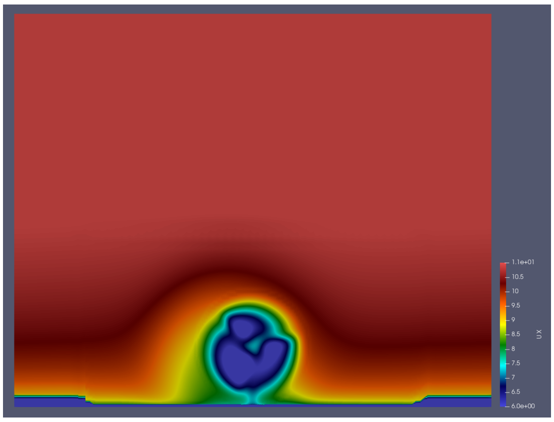

(a) $x/D = 2$

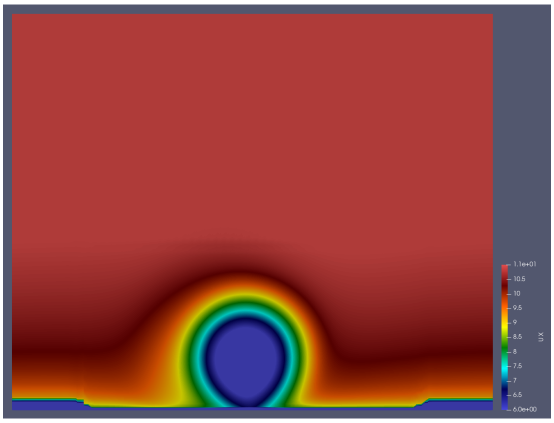

(b) $x/D = 3$

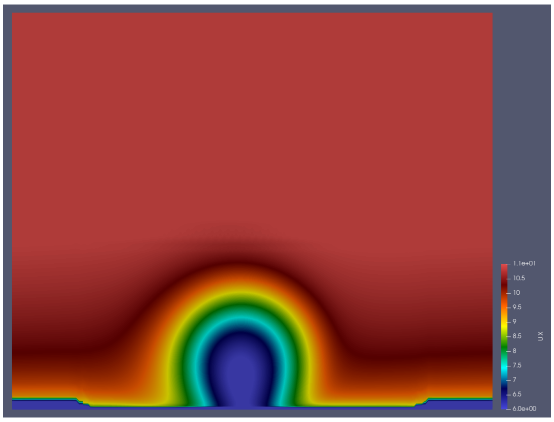

(c) $x/D = 4$

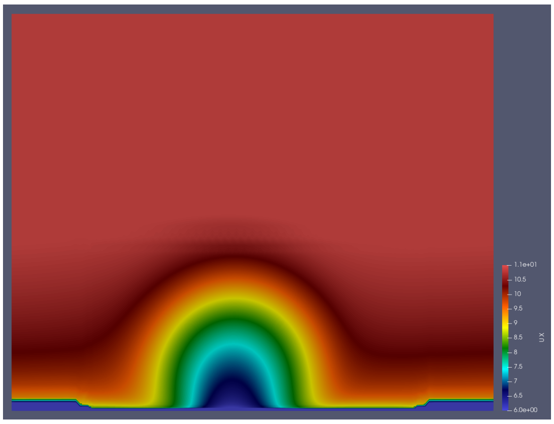

(d) $x/D = 6$

Figure 27: Cross-sectional streamwise velocity $U_x$ for yaw 30° case at downstream positions $x/D = 2, 3, 4, 6$ relative to T1. The curled wake structure develops and persists downstream due to the counter-rotating vortex pair generated by yaw misalignment.

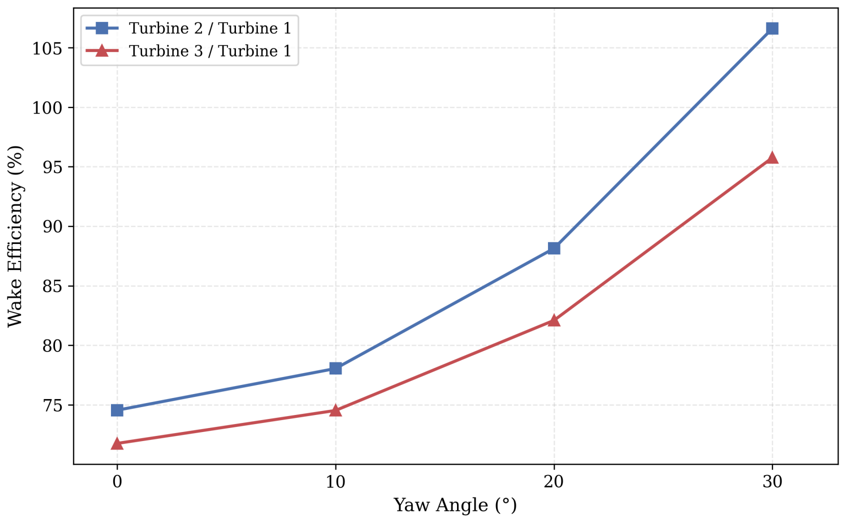


Figure 28: Wake efficiency, defined as the power ratio of each downstream turbine relative to T1, for each yaw misalignment angle $\gamma$, where $\gamma = 0°$ corresponds to the baseline case.

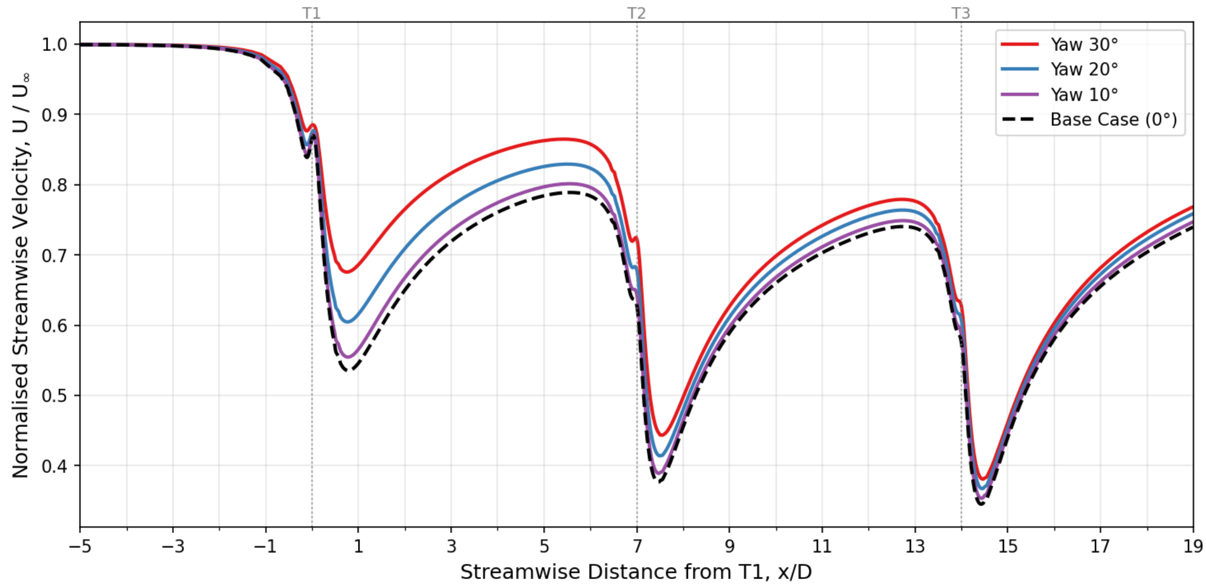


Figure 29: Normalised streamwise velocity $U/U_\infty$ along the farm centerline as a function of streamwise distance from T1 for each yaw misalignment angle $\gamma$. Vertical dashed lines indicate the streamwise positions of T1, T2, and T3.

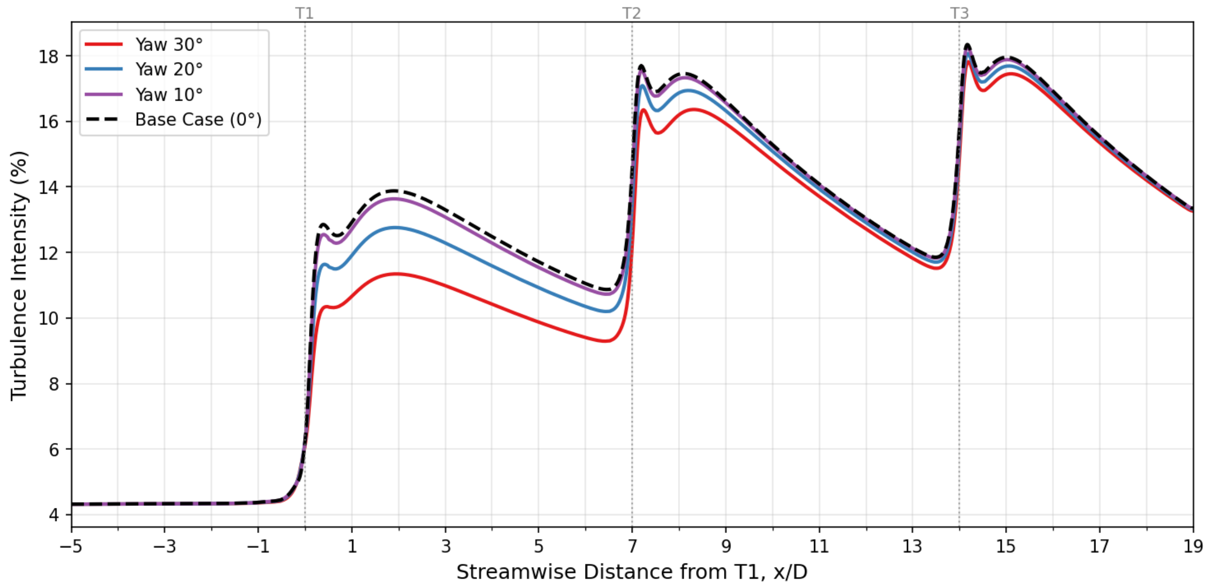


Figure 30: Streamwise turbulence intensity distribution along the farm centerline as a function of streamwise distance from T1 for each yaw misalignment angle $\gamma$. Vertical dashed lines indicate the streamwise positions of T1, T2, and T3.

## 4.4 Comparative Analysis

Having examined each wake control strategy individually, this section presents a direct comparison of all three methods against the baseline case. The comparison focuses on total farm power output, wake velocity recovery, and turbulence intensity reduction, providing the basis for answering the research questions outlined in Section 1.5.

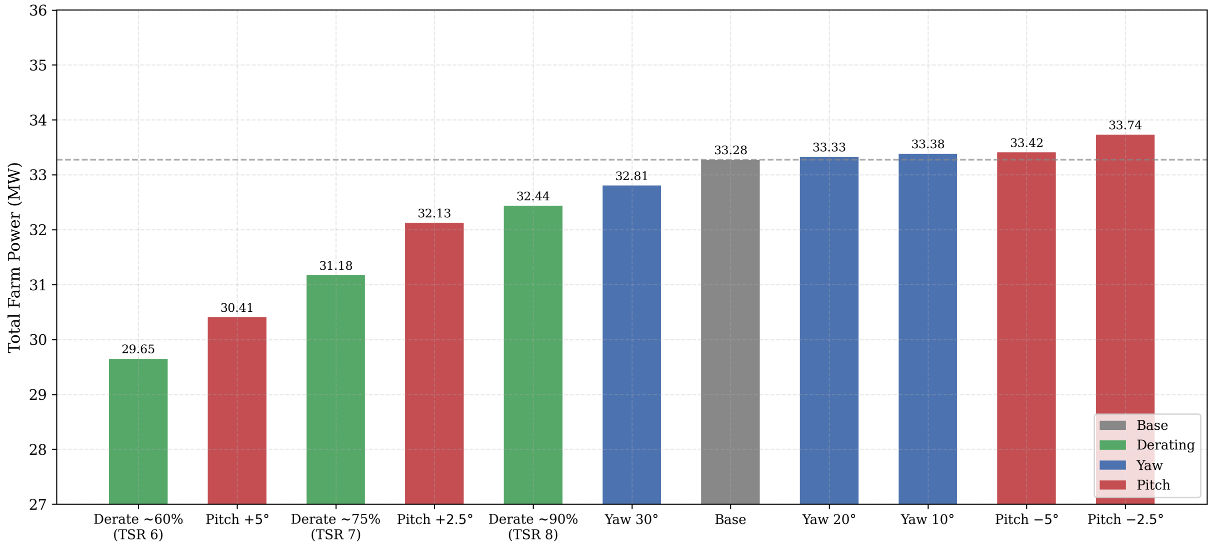


Figure 31: Total farm power output for all wake control cases, ordered from lowest to highest. The baseline ($P_{farm}$ = 33.28 MW) is shown as both a reference bar and a horizontal line

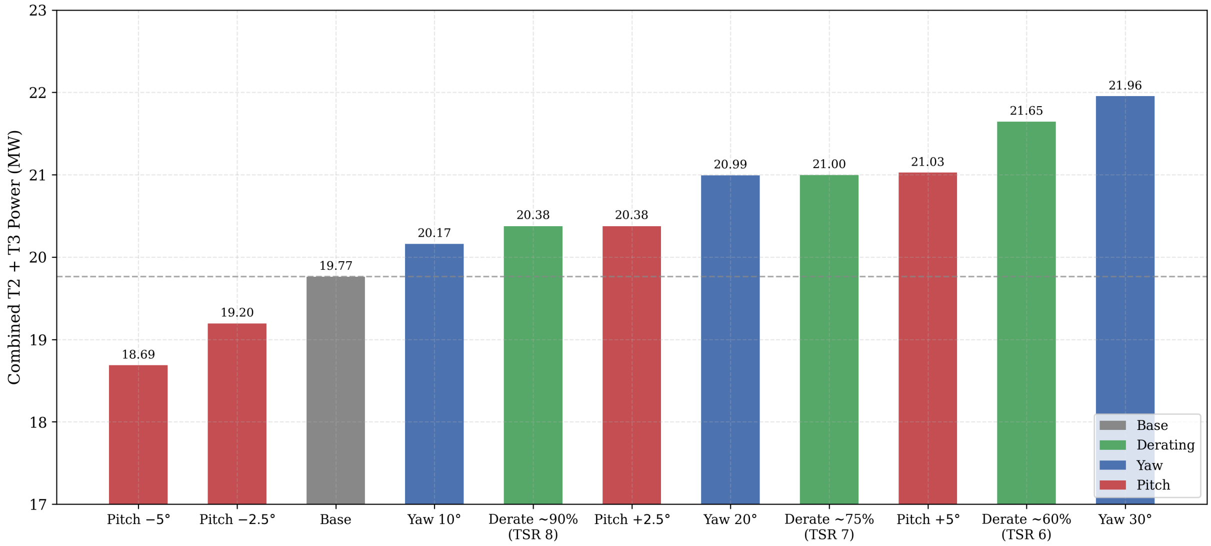


Figure 32: Total farm power output of T2 and T3 for all wake control cases, ordered from lowest to highest. The baseline ($P_{T2\&T3}$ = 19.77 MW) is shown as both a reference bar and a horizontal line

Table 7: Per-turbine performance results averaged over $t > 300$ s for all wake management cases. IEA 15MW BEM reference $C_P = 0.489$.

| Case | T1 $C_P$ | T2 $C_P$ | T3 $C_P$ | T1 (MW) | T2 (MW) | T3 (MW) | Farm (MW) | Δ Farm Power vs Base (%) |
|---|---|---|---|---|---|---|---|---|
| Base | 0.4876 | 0.3635 | 0.3499 | 13.511 | 10.072 | 9.695 | 33.278 | — |
| Pitch −5° | 0.5314 | 0.3329 | 0.3417 | 14.724 | 9.224 | 9.468 | 33.417 | +0.42 |
| Pitch −2.5° | 0.5246 | 0.3473 | 0.3456 | 14.536 | 9.623 | 9.576 | 33.736 | +1.37 |
| Pitch +2.5° | 0.4242 | 0.3810 | 0.3545 | 11.754 | 10.557 | 9.823 | 32.134 | −3.44 |
| Pitch +5° | 0.3385 | 0.3998 | 0.3592 | 9.379 | 11.078 | 9.953 | 30.410 | −8.62 |
| Derate 90% | 0.4353 | 0.3807 | 0.3548 | 12.062 | 10.549 | 9.831 | 32.442 | −2.51 |
| Derate 75% | 0.3673 | 0.3982 | 0.3597 | 10.177 | 11.034 | 9.967 | 31.178 | −6.31 |
| Derate 60% | 0.2889 | 0.4166 | 0.3647 | 8.005 | 11.544 | 10.105 | 29.654 | −10.89 |
| Yaw 10° | 0.4770* | 0.3723 | 0.3555 | 13.217 | 10.316 | 9.850 | 33.384 | +0.32 |
| Yaw 20° | 0.4451* | 0.3923 | 0.3654 | 12.333 | 10.870 | 10.125 | 33.328 | +0.15 |
| Yaw 30° | 0.3916* | 0.4175 | 0.3750 | 10.851 | 11.568 | 10.391 | 32.810 | −1.41 |

* T1 $C_P$ corrected by $\cos^2(\gamma)$ to account for turbinesFoam normalisation using reduced freestream velocity magnitude. Farm (MW) denotes total farm power output [T1 + T2 + T3].

Table 8: Streamwise turbulence intensity (TI) at downstream rotor planes for all wake management cases, with percent change relative to the base case. Values are collected from T2 and T3 rotor planes to best evaluate fatigue risk.

| Case | TI T2 (%) | TI T3 (%) | ΔTI T2 vs Base (%) | ΔTI T3 vs Base (%) |
|---|---|---|---|---|
| Base Case | 14.376 | 15.276 | 0.00 | 0.00 |
| Pitch −5° | 15.313 | 15.549 | +6.52 | +1.79 |
| Pitch −2.5° | 14.930 | 15.436 | +3.85 | +1.05 |
| Pitch +2.5° | 13.659 | 15.072 | -4.99 | -1.34 |
| Pitch +5° | 12.808 | 14.827 | -10.91 | -2.94 |
| Derate 90% (TSR 8) | 13.612 | 15.167 | -5.31 | -0.71 |
| Derate 75% (TSR 7) | 12.747 | 14.980 | -11.33 | -1.94 |
| Derate 60% (TSR 6) | 11.787 | 14.792 | -18.01 | -3.17 |
| Yaw 10° | 14.211 | 15.202 | -1.15 | -0.48 |
| Yaw 20° | 13.648 | 14.990 | -5.06 | -1.87 |
| Yaw 30° | 12.734 | 14.722 | -11.42 | -3.63 |

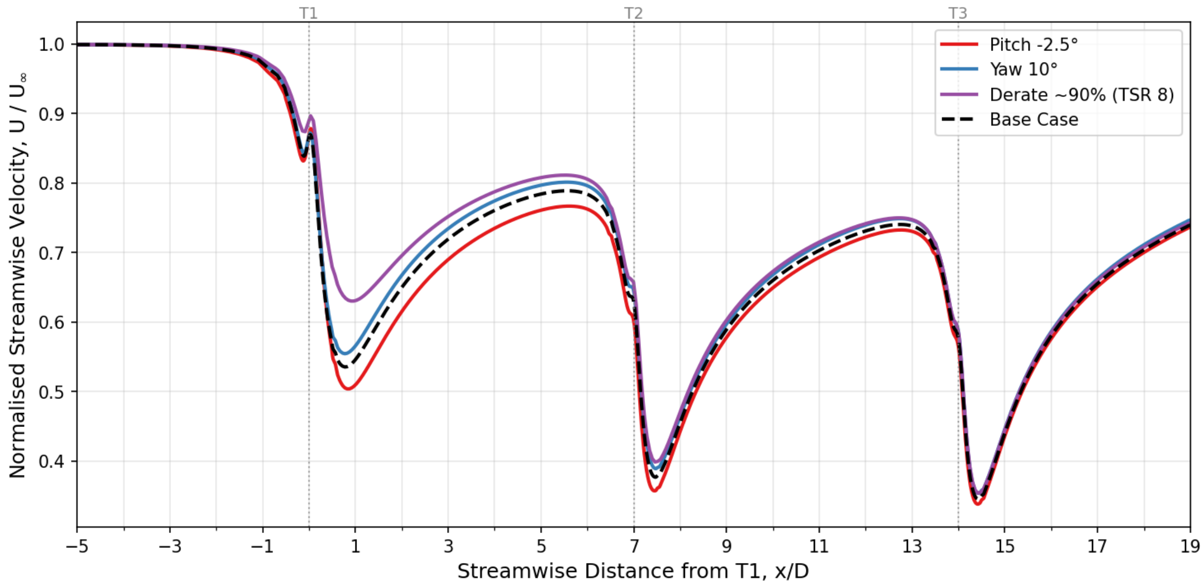


Figure 33: Normalised streamwise velocity $U/U_{\infty}$ along the farm centerline as a function of streamwise distance from T1 for the following cases: Pitch $-2.5°$, Yaw $10°$, Derate 90% and Base case. Vertical dashed lines indicate the streamwise positions of T1, T2, and T3.

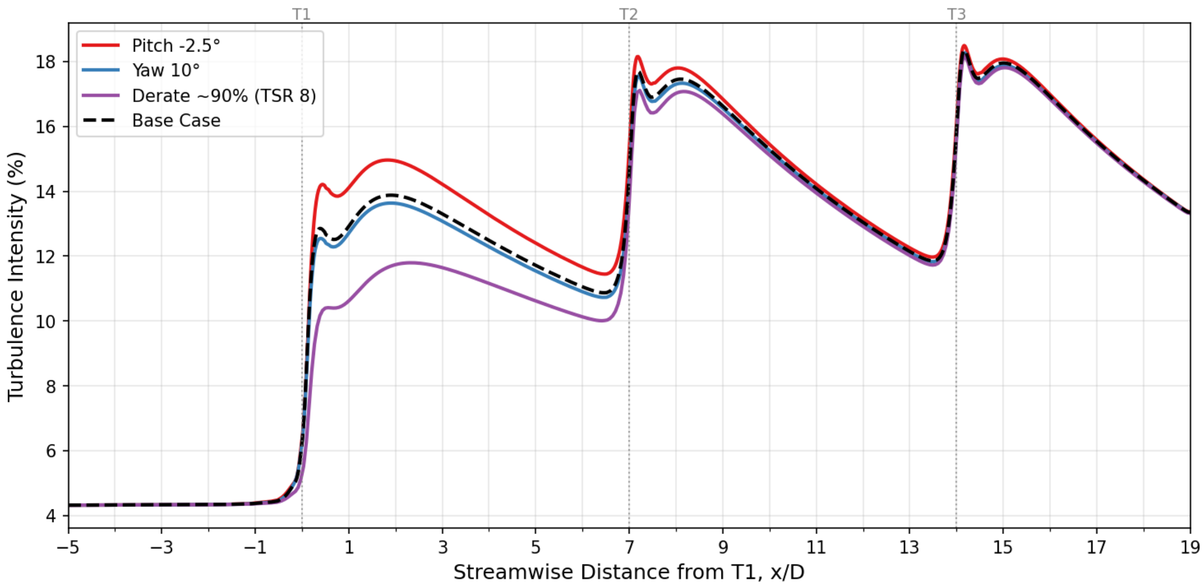


Figure 34: Streamwise turbulence intensity distribution along the farm centerline as a function of streamwise distance from T1 for for the following cases: Pitch $-2.5°$, Yaw $10°$, Derate 90% and Base case. Vertical dashed lines indicate the streamwise positions of T1, T2, and T3.

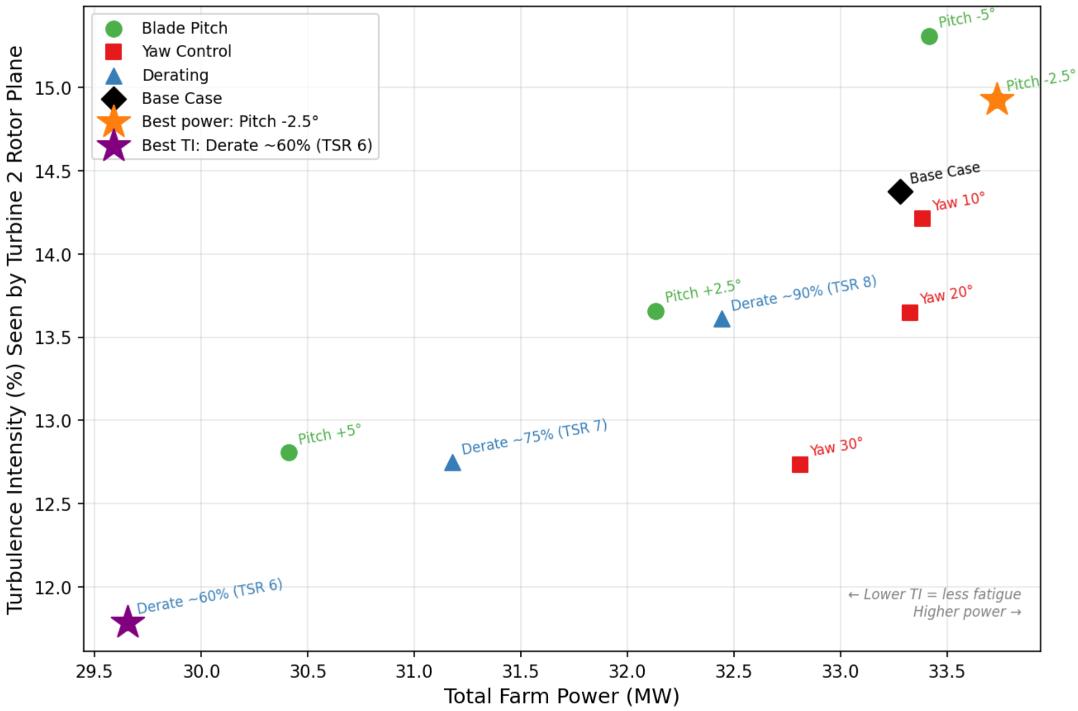


Figure 35: Incoming turbulence intensity (%) as seen by the rotor plane of turbine 2 versus total farm power for all wake management cases. Points in the lower right region indicate favourable operating conditions with high farm power and low turbulence intensity. The optimal strategy for power production (Pitch −2.5°) and the optimal strategy for turbulence reduction (Derate ~60%, TSR 6) are highlighted as a star symbol.

# 5 Discussion

This chapter interprets the CFD simulation results presented in Section 4 in the context of the research questions outlined in Section 1.5. Each wake control strategy is discussed individually with respect to its aerodynamic mechanism and observed effects on farm power output, wake velocity recovery, and turbulence intensity. A comparative analysis then directly addresses which strategy performs best overall. The chapter concludes with a discussion of the limitations and sources of uncertainty inherent to the simulation approach.

## 5.1 Axial Induction Control via Pitch Performance

The aim of axial induction control is to use techniques to reduce the induction factor of the controlled upstream turbine so that the directly downstream turbine experiences a shorter and more recovered wake. As mentioned in Section 2.4, this is done through the mechanism of the upstream turbine extracting less momentum from the flow before it. Changing the blade pitch angle of the turbine is one method of AIC, and for this research, collective pitching for all three blades is used. Changes in the pitch impact the angle of attack for each blade, thus affecting the power output for turbine 1 due to changing forces on the blade as outlined in Section 3.2. When these blade forces change, the thrust coefficient, $C_t$, is impacted, and so is the axial induction factor, as seen in equation (4). The results in Section 4.1 are produced from pitching toward stall through decreasing the pitch angle by -5° (case 1) and -2.5° (case 2), and through pitching toward feather by positive 2.5° (case 4) and 5° (case 5). These results will be examined further from a power production, wake velocity, and wake turbulence intensity lens to best explain the phenomena.

***Power Analysis***

As one of the goals of this research is to determine which wake control method contributes to the best power output, it is important to relay the critical findings that relate to the power production per turbine and for the whole farm. Power and the power coefficient, $C_p$, are directly related through equation (3). So, first looking at how $C_p$ and power change for just T1, it is obvious from figures 13a that pitching toward feather with +2.5° and +5° decreases both power and $C_p$. For 2.5° and 5°, there is a 13% and 31.5% decrease, respectively, in $C_p$ and power from the base case. Whereas for pitching toward stall produces a 7.6% and 9% increase in power and $C_p$ when pitching -2.5° and -5°, respectively, for T1.

From past research [6] and aerodynamic theory, the curve in figure 13a was expected to have a symmetric and parabolic shape, where the base case of 0° would have the highest $C_p$ and power output if the blade is operating at optimal conditions (optimal TSR, blade pitch, wind speed, etc.). Since figure 13a does not exactly follow this trend, a BEM QBlade turbine analysis for the IEA 15 MW blades is performed for all blade pitching to gather insight. It is concluded from figure 6 that the optimal TSR and design TSR are not the same for this turbine. It can be seen that the optimal TSR is 10.4 while the design TSR is 9 [44]. Additionally, figure 15 shows that, when compared to figure 13a, the changes in $C_p$

per pitch angle from QBlade have the same trend as those from OpenFoam, verifying that the results of this research are accurate. Knowing that the turbine is designed to operate at a less than optimal TSR means that the blades are still able to be negatively pitched and increase the angle of attack more before stall is reached. This explains why negatively pitching increases the $C_p$ and power rather than decreasing it, because the blade angle for peak $C_p$ at TSR of 9 is not the base blade pitch angle.

The aerodynamic mechanisms behind the trend of power and $C_p$ decreasing as the pitch angles increases starts with the fact that a higher blade pitch leads to a lower angle of attack ($\alpha$). Thus the lift force increases as shown in equation (29) since $C_L$ raises in relation to $\alpha$. Subsequently, the rotor torque raises which lastly increases the $C_p$ and power for the turbine. [48] This trend of decreasing pitch angle to increase $C_p$ or, inversely, increasing pitch angle to decrease $C_p$ leads to the impact these changes to T1 have on the downstream T2 and T3.

With respect to T1, as its $C_p$ and power production decreases, it is extracting less and less momentum from the wind. This means T1 is taking less kinetic energy out of wind as it flows through the rotor when pitched toward feather. This allows for more momentum to remain in the flow for the downstream turbine 2. Referring back to figure 13a shows how this effect creates a trend for T2 and T3. This trend is that the $C_p$ for T2 and T3 increases with pitch angle, and is directly related to the fact that $C_p$ of T1 is lowering. For T2, the $C_p$ raises by a range of 4.1 - 4.9% per each 2.5° incremental increase of the pitch angle on T1. Turbine 3 only experiences a 5.1% increase in $C_p$ over the whole 10° range (-5° to +5°) of blade pitching. This can also be seen in figure 13a as the trend for T3 has an almost flat slope. This relation is because only T1 has the AIC via pitch applied to its blades, so only T2 is seeing the benefits. While these phenomena are important to understand, it also illustrates a tradeoff effect of T1's power decreasing while T2 and T3 increase in power production. This effect is why it's essential to look at the total farm's power production for each pitch angle.

The total farm power output is calculated by summing the power of turbine 1, 2, and 3. The curve of total power vs pitch angle follows a very similar trend to the $C_p$ of T1, but is not exactly the same in a few ways. The peak total power is at a pitch of -2.5° with a small 1.37% increase from the 0° pitch base case's total power. For a pitch of -5° the peak power for T1 is outweighed by the downstream power losses of T2 and T3. Similarly, for a positive 5° pitch. While pitching toward feather increases the power of both T2 and T3, it is not of a large enough magnitude. So, the total farm power output decreases for all positively pitched cases (case 3 and 4). This makes it obvious that pitch toward feather is not beneficial for total power production when the columns consist of directly aligned turbines. Therefore, the pitch angle of -2.5° for this specific case of a large offshore turbine that operates at a design TSR lesser than the optimal TSR is the optimal pitch angle for total farm power production.

### ***Wake Velocity Analysis***

In order to add more context to the mechanisms behind the power and turbulence intensity trends, it is necessary to analyze the wake velocity characteristics. The results show with figure 17 that pitching toward feather of turbine 1 decreases the normalized streamwise velocity of the wake behind it. Inversely, the trend also follows that pitching toward stall increases the wake velocity. This effect is linked directly to how $C_t$ changes. Since only T1 has pitching applied, looking at the $C_t$ effects of turbine 1 in figure 13b is most helpful for determining the correlation between upstream turbine $C_t$ and downstream wake velocity.

From this figure 13b it is easy to see that for turbine 1, where the blade pitching effects are applied, $C_t$ decreases as pitch angle increases. As mentioned previously, an essential aspect of rotor and wake performance is assessing how much momentum the rotor extracts from the flow thus also measuring how much momentum is left in the wake for the downstream turbine. As equation (4) shows, $C_t$ is a function of $a$, the induction factor. As the wind flows through the rotor, the velocity and rate of change of momentum are altered, and the induction factor represents the reduction fraction of these aspects for a turbine. Therefore, it is appropriate to directly link that any changes to $C_t$ will also happen to the amount of momentum extracted from the flow. This provides the explanation for why pitching toward feather produces a more shallow wake velocity deficit (higher velocity overall) with faster wake recovery, because $C_t$ decreases meaning less momentum and speed is taken away from the flow. Another aspect of significance to consider when analyzing figure 17 is that after x/D = 7 the streamwise velocity is nearly the same for each case, which is obviously because only turbine 1 has blade pitching changes applied, whereas turbines 2 and 3 have the same conditions for every case.

Figure 16 illustrates that as the blades are pitched toward feather the wake efficiency of turbine 2 and turbine 3 relative to turbine 1 increases. This aligns with the trend velocity trends of figure 17, meaning a higher wake velocity causes higher wake efficiency for these turbines. This is because the positive blade pitching allows for the downstream turbines to receive less of a depleted inflow. Another key trade-off is that despite turbine 2 and 3 seeing a higher velocity with a higher pitch angle which is beneficial for those turbines' power performances, this significantly decreases the power output for turbine 1. As mentioned previously, this is one of the many reasons why it is imperative to compare the total power output for the farm as is done above.

### *Turbulence Intensity Analysis*

When it comes to the turbulence intensity (%) of the wakes, figure 18 and table 8 show the key observations that pitching toward stall increases the TI of the wake downstream turbine 1, and increasing the blade pitch angle decreases turbulence intensity. The differences between cases in best seen in the near wake region after turbine 1. The mechanism behind an increasing pitch angle leading to decreasing turbulence intensity is due to the lower $C_t$ for pitching toward feather, outlined in figure 13b. As explained in Section 2.2, a lower $C_t$ generates weaker tip vortices and a less energetic shear layer at the wake boundary. This leads to the lower turbulence levels in the near wake region for higher pitch angle cases. An implication that is very worth noting at this point are the limitations that should be accounted for due to using the RANS $k-\varepsilon$ turbulence model. These limitations are fully outlined in Section 2.6 and essentially amount to under-predictions in the near wake region for peak turbulence intensity and over-predictions in the wake recovery rate. With that being said, the results' trends can still be taken for significant consideration; it is just not to be assumed the exact TI values are quantitatively accurate.

When comparing figures 18 and 17, it is observed that as turbulence intensity decreases over the cases, the velocity increases. This is because a higher TI means there are more velocity fluctuations present. These fluctuation lead to a slower overall wind speed. Although, a raised turbulence intensity promotes increased mixing in the wake. This mixing allows for a faster wake recovery, this can be seen in figure 17 that for the pitch toward stall cases (those that have the higher turbulence intensities) have the largest velocity deficit, but are able to recovery much faster than the positive pitch cases. Additionally, there are other implications that stem from an increased turbulence intensity when increasing the pitch angle. As established in Section 2.3, the increased fluctuations and unsteady flow increases the changes in structural loads for turbine 2 and 3. There is risk for fatigue if the structural loads are often fluctuating. If the aim is reduce potential fatigue risk, then pitching toward feather is the best choice. But, this choice would come at an 8.62% cost to power production. This is a significant tradeoff, and it needs to be considered if this is the best choice as there is a 10.91% decrease in turbulence intensity as seen in table 8. This percent change in TI also can not be directly equated to a 10.91% decrease in risk for fatigue; it can just be said that decreasing TI decreases the risk for fatigue overall. Lastly, something to point out is in both figure 17 and 18 there is an observed convergence at turbine 2 and 3 (x/D = 7 and x/D = 14). This suggests that each turbine has rotor-induced turbulence emitting in the negative streamwise direction, combating the positive streamwise velocity and TI.

## 5.2 Axial Induction Control via Derating Performance

Axial induction control via derating achieves the same objective as pitch control but through a different aerodynamic path. AIC via derating curtails the upstream turbine's power output to a fixed percentage of its rated value, shifting the operating point away from the optimal tip speed ratio and reducing the thrust coefficient, $C_t$, which is directly related to the axial induction factor, as seen in equation (4). Three derating levels were applied to T1, corresponding to approximately 90%, 75% and 60% of rated power. The following section examines the performance of this strategy across farm power output, wake velocity, and turbulence intensity.

***Power Analysis***

The effect of derating on turbine power output is examined first, as it represents the most direct measure of the upstream sacrifice made by each derating case and establishes the farm-level trade-off that motivates the use of this strategy. As power production is directly related to the value of $C_p$ through equation (3), it is of great importance. In figure 19, the trend for time-averaged $C_p$ for each turbine per derating case can be observed. The figure shows a clear trend where T1, $C_p$, decreases as the TSR decreases, with a reduction between 10% - 40.7%, while T2 and T3, $Cp$, increase by 1.4% - 12.7% and 1.4% - 4%, respectively. Similar trends can be observed for the $C_t$ in figure 19. This trend is consistent with BEM theory, where operating below $\lambda opt$ shifts the turbine along the $C_p - \lambda$ curve, simultaneously reducing both power extraction and thrust as described in Section 2.1. The steeper decline in T1 $C_p$ relative to the modest gains in T2 and T3 illustrates the fundamental tradeoff for AIC via derating. The upstream turbine must sacrifice power to improve downstream conditions, and this sacrifice is only worthwhile at the farm level if the downstream gains exceed the upstream loss. This tradeoff is examined further through the total farm power output.

This imbalance between upstream loss and downstream gain is confirmed in figure 20, which shows the correlation between $C_p$ and total farm power across all derating cases. Although downstream turbine power improves with increasing derating level, the improvement is insufficient to offset the reduction in T1 output, resulting in a net power reduction of -2.5% to -10.9% compared to the baseline, as seen in table 9. The derating strategy, therefore, did not achieve a net improvement in total farm power output under the conditions simulated, and thus is an ineffective method if the goal is to enhance total power production, which is one of the primary reasons wake strategies have been examined so extensively. However, this does not signify that this is an inadequate wake management strategy. As noted in the methods Section 3.3, all derating cases are simulated with a fixed blade pitch angle of 0°. which represents a simplification of real industrial practice where pitch adjustments would typically accompany generator torque derating to maintain aerodynamic efficiency.

Despite this simplification, existing literature suggests that fixed-pitch derating can still improve total farm power production under certain conditions. Kazda et al. [49] demonstrated that derating an upstream turbine to 87.5% of rated power with a fixed pitch angle of 0° produced a 9.7% increase in total power for the turbines considered, suggesting that the approach used in this study is not inherently ineffective. However, there are several key differences between the two studies that limit direct comparability. The wind farm simulations are done for onshore wind turbines, thus including a roughness height, which can be negated for offshore wind turbines as used in this study. The farm layout is non-linear, with two out of nine turbines being directly placed behind two upstream turbines, which are operated with AIC via derating to potentially mitigate the effects of the upstream turbines' wakes. In contrast, this study places all three turbines in line, maximizing wake exposure and amplifying the upstream power sacrifice relative to the downstream recovery potential. Thus, the surrounding conditions as well as placement of turbines play a big role in the effectiveness of the AIC via derating strategy and need to be taken into account for real-world implementation.

### ***Wake Velocity Analysis***

While total farm power quantifies the energy consequence of derating, the wake velocity field provides the underlying physical explanation for the observed power changes. Examining the velocity deficit downstream of T1 reveals how effectively each derating level reduces the momentum extracted from the flow and how this translates to improved inflow conditions for turbines 2 and 3. In figure 22, the trend for normalized streamwise velocity for each turbine per streamwise distance can be observed. The figure shows a clear trend where the velocity deficit behind T1 decreases with increasing derating level, from approximately 55% of freestream velocity in the baseline case to around 80% for the 60% derating case. This confirms that reducing TSR directly reduces $C_t$ and produces a shallower wake as the theory predicts, in Section 2.4. Further downstream, the difference in deficit becomes nearly uniform between the derating cases and the base case as turbulent mixing homogenizes the wake. With T1 operating at reduced $C_t$, its downstream wake recovers more rapidly, delivering higher velocity inflow to T2 and T3. The increased inflow velocity allows T2 and T3 to operate closer to their optimal operating point, which is reflected in their increased $C_t$ and $C_p$ values shown in figure 19. Wake recovery rate can also be seen to improve with more derating. However, at no point is the wake able to approach freestream conditions, closest it comes to freestream conditions is just before T2 at approximately 7D, with a deficit of around 15%. Though the normalized streamwise velocity becomes almost uniform around T3 due to the combined wake from turbines 1 and 2, it is still slightly improved by derating, which can be confirmed by the increased power production for T3, compared to the base case for all derating cases as seen in table 9. These velocity improvements are consistent with the $C_p$ gains observed for T2 and T3 in the power section, confirming that wake velocity recovery is the primary mechanism driving downstream power improvement.

This relationship is further quantified in figure 21, which shows the wake efficiency, defined as the power ratio of each downstream turbine relative to T1, for each derating case. Both T2 and T3 show a clear increase in wake efficiency with increased derating level, reaching approximately 143% and 126% of T1 power, respectively at TSR = 6, derating 60%. The fact that wake efficiency exceeds 100% at higher derating levels reflects the significant curtailment of T1 rather than an absolute increase in downstream turbine power beyond rated capacity. Turbine 1, derated by 60%, is producing substantially less power, decreasing by 40.7% compared to the base case, while T2 and T3 benefit from improved inflow conditions, increasing their combined power production by 8.7%. The consistently higher efficiency of T2 relative to T3 is due to the combined wake from T1 and T2. Even as derating improves T1 wake, T3 inflow remains constrained by the wake generated by T2, which is not subjected to any control input.

### *Turbulence Intensity Analysis*

Beyond power output and wake velocity, turbulence intensity (TI) within the wake represents a critical metric for assessing the fatigue risk experienced by downstream turbines. As established in Section 2.3, higher TI leads to increased velocity fluctuations at the blade element level, directly increasing the variability of aerodynamic lift forces on the rotor blades as shown in equations (8) and (9). These fluctuating loads accumulate as fatigue damage over the turbine lifetime, making TI a key qualitative proxy for structural fatigue risk. It should be noted that the $k-\varepsilon$ model is known to overpredict turbulent diffusion, meaning absolute TI values may differ from higher-fidelity LES predictions, as discussed further in Section 2.6. The turbulence intensity, as defined in equation (7), is influenced by the rotor-induced turbulence and atmospheric turbulence. The following Section examines how each derating level affects the TI distribution downstream of T1 and what this implies for the fatigue risk of T2 and T3. Figure 23 shows the trend for streamwise turbulence intensity distributed along the centerline for each case. The figure shows clearly that all four cases have an ambient TI of approximately 4.3% at hub height, confirming that the observed differences in TI are attributable solely to the wake control strategy rather than variations in inflow conditions.

Behind T1, derating produces a significant reduction in wake-added TI, with baseline case peaks at 14.4%, while the derating cases peak at 11.8%-13.6%, with TI increasing as less derating is implemented. This reduction is consistent with the lower $C_t$ values observed for derated T1. As discussed in Section 2.2, a reduced thrust coefficient extracts less momentum from the flow, generating weaker tip vortices and less turbulent shear layer in the near wake. Further downstream, near T2, all cases experience a sharp spike, with the base case peaking at approximately 17-18% and the 60% derating case showing the lowest spike at approximately 16%. The less derated cases have less than 1% change from the base case, showing little improvement in decreasing the TI. This modest reduction in TI, reflects the improved inflow conditions delivered by the derated T1 wake. However, the resulting spike suggests that T2's own rotor-induced turbulence dominated over the inherited wake turbulence from T1. The sharp TI spikes at the T2 and T3 rotor planes reflect the rotor-induced turbulence generated as each turbine interacts with the incoming flow, consistent with the elevated TI associated with the cylindrical shear layer described in Section 2.2. At T3, the difference in TI becomes uniform between the derating cases and the base case, with a TI of approximately 18-19%, with negligible differences between derating levels. This indicates that T3's turbulence environment is governed primarily by T2's wake rather than T1's derated wake, which is consistent with the results of the wake velocity. The reduced TI in the wake of derated T1 suggests a meaningful reduction in fatigue risk for T2 under higher derating levels. This is consistent with the relationship established in Section 2.3 between TI and structural fatigue risk. However, the benefit to T3 remains limited by the dominant influence of T2's wake, which governs the turbulence environment at that downstream position regardless of the derating applied to T1. This reveals a secondary tradeoff inherent to derating; while higher derating levels produce greater TI reduction and improved downstream flow conditions, they simultaneously impose larger upstream power losses that cannot be recovered by downstream gains under the conditions simulated. The optimal derating level therefore depends on whether the primary objective is power maximization or fatigue risk reduction, as no single derating level achieves both simultaneously.

## 5.3 Yaw Control Performance

In contrast to AIC strategies, where the upstream power reduction results from a deliberate modification of the turbine's aerodynamic operating point, the power loss under yaw control is an unavoidable aerodynamic consequence of rotor misalignment. The upstream turbine is physically oriented away from its optimal energy extraction position, by rotating the rotor plane of T1 by a misalignment angle $\gamma$. Three different misalignment angles were applied, $\gamma = 10°, 20°$ and $30°$, and the following section examines the performance of this fundamentally different wake control mechanism across farm power output, wake velocity, and turbulence intensity.

### ***Power Analysis***

Firstly, the impact of using yaw control on turbine power output will be examined, as it is a direct measure of the upstream sacrifice made by each yaw case and establishes the farm-level trade-off that motivates the use of this strategy. In figure 24, the trend of time-averaged $C_p$ per yaw angle case for each turbine can be observed. Turbine 1 experiences a decrease in $C_p$ of 2.2%-19.7% compared to the base case, as the $\gamma$ increases. As mentioned in the methods section 3.4, the $C_p$ values for yaw cases are corrected by $cos(\gamma)$ as described in equation (35) to account for turbinesFoam normalization using the reduced freestream velocity magnitude. This is a direct consequence of rotor misalignment, as $\gamma$ increases, the component wind speed normal to the rotor plane decreases proportionally to $cos(\gamma)$, reducing the effective wind speed available for energy extraction, as described in Section 2.4. Unlike AIC, where the upstream power reduction is a deliberate operational choice with no regard to wind resources. However, T2 and T3 are not yawed and thus $C_p$ increases by 2.4%-12.9% and 1.6%-6.7%, respectively, as $\gamma$ increases.This is due to the wake being deflected laterally, leading to less wake interaction. This is true especially for T2 for the yaw 30° case, where the $C_p$ for T2 exceeds $C_p$ for T1. The crossover of T2 $C_p$ above T1 $C_p$ at $\gamma = 30°$ indicates that T1's misalignment has reduced its power extraction to below that of a turbine operating in partial wake. The same trend is observed for $C_t$in figure 24, where T1 $C_t$ decreases steeply with increasing $\gamma$, consistent with $cos^2(\gamma)$ thrust scaling, described by equation (36), while T2 and T3 $C_t$ increase modestly as they receive improved inflow conditions. This is a clear sign that the upstream sacrifice at this angle is disproportionate to the downstream benefit. This disproportion between upstream loss and downstream gain is confirmed in figure 24. The figure shows that a slight increase in $\gamma$ can increase the total power production even with a decreased power output for T1. For $\gamma = 10°$ and 20°, total power production increased by +0.32% and +0.15%, respectively. However, beyond a certain misalignment angle, the negative effect on T1 outweighs the positive effects on T2 and T3, as seen for $\gamma = 30°$, where total power production becomes lower than that of the base case, decreasing by -1.41% for total power output. This behavior reveals the central tradeoff of yaw control, where moderate misalignment angles produce sufficient wake deflection to improve downstream conditions while keeping the upstream power penalty manageable, but larger angles impose disproportionate upstream losses that outweigh the downstream gains. The existence of an optimal yaw angle reflects this balance, beyond which the cosine power penalty on T1 dominates the farm level outcome. Although $\gamma = 10°$ successfully produced a net farm power gain of +0.32%, both magnitude and optimal angle are lower than reported in comparable studies, a discrepancy that warrants examination of the key methodological differences.

This discrepancy is further evident when compared to the experimental results of Bartl et al. [10], who conducted an experimental wind tunnel study with two aligned turbines and reported an approximately +8% increase in total power production at $\gamma = 30°$. The experimental nature of the study limits direct comparability with the present CFD simulation. Several experimental conditions likely contributed to the higher optimal angle reported. A wind tunnel blockage ratio of 12.8% causes freestream flow acceleration around the deflected wake, artificially enhancing downstream turbine power at higher yaw angles. Notably, the authors acknowledge this effect but do not apply blockage correction models to their results. [10] The authors also report unusually high T2 $C_p$ values, which they attributed to increased velocity levels of $u/u_{ref} = 1.1$, increasing their total power production. This suggests that their reported power gains at higher yaw angles are likely overestimated relative to open-atmospheric conditions such as those simulated in the present study.

The CFD study by Fleming et al. [8], reports a +4.6% farm power increase at $\gamma = 25°$. Several methodological differences likely contributed to this discrepancy, such as the use of LES. LES resolves vortical wake structures more accurately than the RANS $k - \varepsilon$ approach. As discussed in Section 2.6, the enhanced turbulent diffusion in RANS smooths the deflected wake and may reduce the effective lateral displacement at higher $\gamma$. Furthermore, the difference in boundary conditions could also be a significant contributing factor. The present study employs cyclic lateral boundary conditions, which simulate the presence of adjacent turbine rows by reintroducing laterally deflected wake fluid into the domain. This closely resembles the operating conditions of a real wind farm where deflected wakes affect neighboring turbines rather than dissipate freely. Fleming et al. [8] simulate only two isolated turbines without cyclic lateral boundaries, meaning their deflected wake is not reintroduced into the domain. This difference in boundary treatment may contribute to the higher optimal yaw angle reported in their study, as the lateral constraint imposed by cyclic boundaries in the present simulation limits the net benefit of larger misalignment angles where wake deflection is most pronounced.

Together, these methodological differences highlight the sensitivity of the optimal yaw angle and achievable power gains to the simulation approach, boundary conditions, and experimental setup, making direct quantitative comparison between studies challenging.

### ***Wake Velocity Analysis***

Having established the farm-level power consequences of yaw misalignment, the wake velocity field is examined to provide the underlying physical explanation for the observed power trends. Unlike AIC where the velocity deficit decreases in magnitude while remaining centered on the streamwise axis, yaw control produces a lateral displacement of the wake. The deflected wake moves away from the downstream turbines rather than becoming shallower. This distinction is clearly visible in the horizontal plane velocity contour shown in figure 26, where the T1 wake is deflected away from the farm centerline with $\gamma = 30°$. Figure 27 shows a cross-sectional view of the development of a yawed wake, at x/D=2,3,4,6 for the 30° case. At the near wake, x/D=2, the wake is visibly asymmetric, consistent with early development of the counter-rotating vortex pair described in Section 2.2. [21] As the wake moves further downstream, the wake deficit shifts slightly in a lateral direction, confirmed by the top view figure 34, at hub height. Immediately preceding T2, at x/D = 6, the wake has deflected sufficiently for T2 to encounter a more asymmetric flow. The curl wake structure, while present, is less visually pronounced as RANS $k-\varepsilon$ approach smooths the sharp vortical structures such as the counter-rotating vortex pair. [34]

The effect of yaw angle on normalized streamwise velocity is quantified in figure 29, for each turbine per streamwise distance. Behind T1, a clear improvement in centerline velocity is observed with increasing $\gamma$, from approximately 55% of freestream velocity in the base case to approximately 58%-68% as the yaw angle increases. This improvement reflects the lateral displacement of the wake rather than a reduction in deficit intensity. That is the fundamental distinction between yaw control and AIC. At the T2 rotor plane, the normalized streamwise velocity becomes approximately 45% at $\gamma = 30°$, 43% at $\gamma = 20°$, and 39% at $\gamma = 10°$, compared to the 38% for the base case. These results are consistent with the $C_p$ gains observed for T2 in the power section, reflecting a meaningful improvement in inflow conditions. Further downstream at T3, the differences between yaw cases narrow progressively as T3 is dominated by T2's wake, regardless of T1's yaw angle, limiting the benefit of wake deflection at this downstream position.

The relationship between wake deflection and downstream power gain is further quantified in figure 28, which shows the wake efficiency defined as the power ratio of each downstream turbine relative to T1, for each yaw case. Both T2 and T3 show a consistent increase in wake efficiency with increasing $\gamma$, where T2 and T3 at $\gamma = 30°$ reach approximately 107% and 96% of T1 power, respectively. The fact that T2 wake efficiency exceeds 100% at 30° reflects the significant curtailment of T1 rather than T2 exceeding its rated capacity. The relatively consistent gap between T2 and T3 efficiency across all yaw angles suggests that yaw control produces a distributed downstream benefit. The lateral deflection of T1's wake improves inflow conditions progressively across the farm rather than concentrating the benefit solely at T2.

These results confirm that yaw control successfully deflects the T1 wake laterally across all tested misalignment angles. Thus, instead of T2 receiving a weaker centered wake, how AIC operates, T2 receives a partially deflected flow where aerodynamic conditions vary across the rotor plane. The implications of this asymmetric loading for turbulence intensity and fatigue risk are examined in the following section.

### *Turbulence Intensity Analysis*

Beyond power output and wake velocity, turbulence intensity (TI) within the wake represents a critical metric for assessing the fatigue risk experienced by downstream turbines. As established in Section 2.3, elevated TI increases the variability of aerodynamic forces acting on downstream rotor blades, as described by equations (8) and (9), accumulating as fatigue damage over the turbine lifetime. It should be noted that the $k-\varepsilon$ model is known to overpredict turbulent diffusion, meaning absolute TI values may differ from higher-fidelity LES predictions, as discussed further in Section 2.6. Unlike AIC, where TI reduction is a result of lower $C_t$, which generates weaker tip vortices and less turbulent shear, yaw control reduces centerline TI through a different mechanism. Yaw control moves the high TI wake core laterally away from the centerline by rotating the rotor plane away from the incoming flow direction, rather than reducing the overall turbulence generated. Figure 30 shows streamwise turbulence intensity distribution along the farm centerline for each yaw case. The figure shows clearly that all four cases have an ambient TI of approximately 4.3% at hub height, confirming that the observed differences in TI are attributable solely to the wake control strategy rather than variations in inflow conditions. Behind T1, turbulence intensity spikes, where the base case peaks around 14.4% compared to yawed cases, where the peak is at 12.7%-14.2% as the yaw angle decreases. The sharp TI spike at T2 reflects rotor-induced turbulence generated as T2 interacts with the incoming flow, consistent with the elevated TI associated with the cylindrical shear layer described in Section 2.2, and is present regardless of yaw angle as T2 itself is not yawed. At T2, the base case spikes to approximately 17-18%, while the $\gamma = 30°$ case shows a reduction to approximately 16%. All yawed cases have a lower centerline TI compared to the base case, with the decreased centerline TI decreasing progressively with increasing yaw angle, confirming that yaw misalignment is able to deflect the core wake laterally. Notably, the $\gamma = 10°$ case shows centerline TI values almost identical to the baseline. Indicating that, though total power output increases, the increase in fatigue risk is still significant due to higher levels of centerline turbulence intensity. At T3, the centerline TI values across all cases converge, with differences between yaw angles narrowing considerably relative to the T1 and T2 regions. T3 remains dominated by T2's own rotor-induced turbulence regardless of T1's yaw angle, limiting the structural loading benefit of wake deflection at this downstream position. Despite this $\gamma = 30°$ maintains a visually noticeable reduction in TI at T3, consistent with the 7% increase in T3 power output observed in table 9, the largest T3 improvement recorded across all wake control strategies tested in this study.

Overall, yaw control demonstrates a meaningful reduction in centerline TI behind T1 and a modest improvement at T2, with the benefit diminishing progressively toward T3 as T2's own rotor-induced turbulence dominates the downstream flow. The TI reduction achieved through lateral wake deflection is less pronounced than that achieved through AIC derating at comparable upstream power sacrifice levels. A distinction that will be examined further in the comparative analysis. Nevertheless, the fatigue risk relief offered to T2 under higher yaw angles represents a tangible benefit of the strategy, particularly when considered alongside the farm power gains observed at $\gamma = 10°$. A further tradeoff specific to yaw control is that while lateral wake displacement reduces centerline TI for the aligned downstream turbines, the deflected wake is redirected toward adjacent turbine columns rather than being eliminated. In the present simulation, this effect is captured through the cyclic lateral boundary conditions, which reintroduce the deflected wake fluid into the domain, representing the interaction between adjacent turbine columns in a real wind farm. This means that at higher yaw angles, the TI reduction observed for T2 and T3 in the aligned column may come at the cost of increased wake loading on laterally adjacent turbines, which is a farm-level consequence that reinforces the importance of optimizing yaw angle carefully rather than maximizing deflection indiscriminately. The contrasting mechanisms of TI reduction between AIC and yaw control deficit reduction versus lateral displacement have distinct implications for downstream fatigue risk that are examined further in the comparative analysis.

## 5.4 Comparative Analysis

This section presents a direct comparison of all three wake control strategies, AIC via pitch, AIC via derating and yaw control, evaluated against the same metrics examined in the preceding sections: total farm power output, wake velocity recovery, and turbulence intensity. The comparison draws on the highest performing case for each strategy and concludes with direct answers to the research questions outlined in section 1.

A key objective of this study is to determine which wake control strategy achieves the highest total farm power and whether this aligns with the strategy that best improves downstream turbine performance, as outlined in the research questions in Section 1.5. In figure 31 the total farm power output for each case is presented, including the base case. The total farm power output for all the wake cases is ordered from lowest to highest to facilitate direct comparison of strategy effectiveness. The ten subcases comprise four AIC pitch angles, three AIC derating levels and three yaw angles. Four out of ten subcases exceed the total farm power of the base case, ranging from +0.15% to +1.37%. All derating cases fall below the baseline case, ranging from −2.5% to −10.9%, confirming that fixed-pitch derating as implemented in this study cannot be considered a viable strategy when the primary objective is increased power production. The two highest performing cases are AIC pitch at −2.5° and pitch −5°, producing 33.74 MW and 33.42 MW, respectively, both exceeding the baseline of 33.28 MW. The other two cases that exceed the baseline are yawing cases at 10° and 20°, producing 33.38MW and 33.33MW. Making it a viable wake management strategy in regard to increasing power output. However, as previously mentioned, this strategy is limited to lower yaw angles, with $\gamma = 30°$ resulting in a -1.41% power reduction. This method is specifically limited in farm setups, as discussed in Section 5.3, the cyclic lateral boundary conditions mean that excessively deflected wakes re-enter the domain, limiting the net benefit of larger misalignment angles in the present simulation setup. While AIC pitch at −2.5° and −5° achieve the highest total farm power, this is driven entirely by increased T1 power extraction rather than improved downstream performance, making them the highest farm power cases but not the most effective wake management strategies in the traditional sense.

Power production for the combined downstream turbines, T2 and T3, is an important discussion for this thesis. The main focus of wake management strategies is to increase the power output of the downstream turbines while balancing the decrease in power in upstream turbines. Thus, it is important to see if there is a strong correlation between the wake management strategies that presented the greatest improvement in total power and those that produced the greatest total power production for downstream turbines. In figure 32 the total combined power for T2 and T3 for each case is presented. In the figure eight out of the ten subcases exceed the baseline case, by 0.4-2.19MW, which has a combined T2 and T3 power of 19.77MW. The highest performing case is the yaw 30°, producing 21.96 MW. This increase in power production for the downstream turbines can be attributed to yaw control, deflecting T1 wake laterally, allowing T2 and T3 to operate in partially improved inflow conditions approaching freestream velocity. Unlike AIC strategies where the wake deficit remains centered on the downstream turbines, lateral deflection can move the wake core sufficiently far from the rotor centerline that downstream turbines experience near-freestream conditions on a significant portion of their swept area. The two cases that have a combined T2 and T3 power below the baseline are the two negative-pitched cases, pitch $-2.5°$ and pitch $-5°$. Though they had the highest total power production, it was due to T1 power increase instead of the increase in T2 and T3 for the cases. This occurred because the turbine that this report is based on is not set to the optimal tip speed ratio, which is expanded upon in Section 5.1. Consequently, when the AIC via negative pitching (pitching towards stall) was introduced, the angle of attack and thrust increased, boosting T1 power. Had the simulation been run at the optimal TSR, negative pitch control may have produced different results. Operating at optimal TSR would mean any pitch adjustment moves the turbine away from peak efficiency, potentially producing the expected AIC behavior of reduced $C_t$ and improved downstream conditions. The present results, therefore, reflect the specific operating conditions of this study rather than a general limitation of negative pitch control

Considering both total farm power and downstream turbine performance simultaneously, yaw control at $\gamma = 10°$ represents the most balanced wake management strategy, achieving a net farm power gain of +0.32% while also producing meaningful improvements in T2 and T3 power output. The $\gamma = 30°$ case achieves the highest combined T2 and T3 power at 21.96 MW but results in a net farm power reduction of -1.41%, making it suboptimal when total farm performance is the objective. These results confirm that lateral wake deflection at moderate misalignment angles is more effective than either pitch-based or derating-based AIC under the specific operating conditions of this study. These results also reveal that the strategy achieving the highest total farm power does not coincide with the strategy that best improves downstream turbine performance, where pitch $-2.5°$ leads in total farm power while yaw 30° leads in downstream turbine power, as outlined in the research questions in Section 1.5

To understand why the power results differ between strategies and to address which strategy best reduces the downstream velocity deficit as outlined in Section 1.5, the wake velocity field is examined, providing the underlying physical explanation for the observed power changes. In figure 33, a small velocity spike is visible at the rotor centerline immediately downstream of each turbine location. This is attributed to the absence of a resolved hub geometry in the ALM implementation, which allows flow to pass through the hub region unimpeded, a known limitation discussed in Section 2.7. As this artifact is present in all cases equally, it does not affect the relative comparison between strategies. The figure itself describes the normalized streamwise velocity per streamwise distance for the highest performing case for each strategy, which is compared against the baseline. The three cases that are chosen have the highest farm power production for each wake management strategy, pitch −2.5°, 90% derating and yaw 10°. Behind T1, the 90% derating case produces the greatest improvement in cetreline velocity, reaching approximately 65% of streamwise velocity compared to 55% for the baseline. That is a direct consequence of reduced $C_t$ generating a shallower velocity described in Section 2.4. In contrast, the pitch −2.5° case produces a streamwise velocity of approximately 50%, which is marginally below the baseline. However, as has been mentioned before, this is a consequence of the increased $C_t$ for T1, which deepens the wake. This is consistent with prior discussion on observed T2 and T3 power for pitch cases.

Further downstream right before T2, at 5.5D, the dearting 90% and yaw 10° cases both show comparable improvement, reaching approximately 82% and 80% of streamwise velocity, respectively. While the pitch −2.5° case drops to approximately 76%, slightly below baseline at approximately 78%. This confirms that the total farm power gains achieved by negative pitch control are driven entirely by increased T1 power extraction rather than improved downstream conditions. At T3, all cases converge to near identical centerline velocities, with differences between strategies becoming negligible. This is consistent with the findings of the individual wake management sections 5.1, 5.2, 5.3.

The relationship between turbulence intensity and wake recovery rate warrants consideration when interpreting these results. Higher ambient TI generally accelerates wake recovery through enhanced turbulent mixing as established in Section 2.2. However, this does not necessarily translate to improved downstream velocity conditions. Hence, a faster recovering wake still carries a velocity deficit, and the increased turbulence associated with recovery itself imposes additional structural loading on downstream rotors. In the present study, the 90% derating case produces the lowest wake-added TI behind T1 while simultaneously achieving the greatest centerline velocity improvement, suggesting that in this configuration, reducing $C_t$ and the associated wake turbulence is more beneficial than relying on turbulent mixing to accelerate recovery. The yaw 10° case produces a comparable downstream velocity through lateral displacement rather than turbulent recovery, with lower wake-added TI at the centerline than the baseline. The pitch −2.5° case, despite generating higher TI through its increased $C_t$, does not benefit from accelerated recovery in terms of downstream velocity as the deeper initial deficit more than offsets any recovery enhancement from increased mixing. This suggests that for the farm configuration and spacing studied here, the rate of wake recovery is less important than the initial deficit depth in determining downstream velocity conditions.

Considering both centerline velocity recovery and the underlying physical mechanisms simultaneously, the 90% derating case produces the greatest centerline velocity improvement at T2 while yaw 10° achieves comparable downstream conditions with the additional advantage of net farm power gain. The pitch −2.5° case, despite achieving the highest total farm power, produces the worst downstream velocity conditions of all strategies tested, confirming that its power gains are driven by increased upstream extraction rather than improved wake conditions. Regarding the relationship between turbulence intensity and wake recovery, a lower initial velocity deficit achieved through $C_t$ reduction proves more beneficial for downstream conditions than relying on turbulent mixing to accelerate recovery as higher wake-added TI may enhance recovery rate, but the deeper initial deficit produced by higher $C_t$ strategies more than offsets this benefit under the turbine spacing and operating conditions of this study. These results show that the 90% derating case best minimizes the centerline velocity deficit at T2, while yaw 10° achieves comparable downstream conditions through a fundamentally different mechanism, lateral displacement rather than deficit reduction. Critically, wake recovery rate proves less important than initial deficit depth in determining downstream velocity conditions, directly addressing the second research question outlined in Section 1.5.

To answer the question of which wake management strategy minimizes the risk of structural fatigue for the downstream turbines, it's important to restate that conclusions from this research can only be used to state an overall trend in risk of fatigue (referred to as a qualitative proxy), since no absolute real structural load calculations are performed. Additionally, when it comes to turbulence considerations, a large RANS limitation is that the turbulence values are modeled rather than resolved. Looking at figure 35 reveals that AIC via derating by 60% at a TSR of 6 decreases the turbulence intensity the most out of all cases. Numerically, this is a 18.01% reduction in the TI for the second turbine, compared to the base case. As a qualitative proxy to fatigue risk, this means that this case of derating decreases the risk the most. Other than being the best case for fatigue risk reduction, AIC via derating is also overall the best wake control method for this aim. This is determined because not only do all derating cases have TI values below the base case (so do yaw and pitching toward feather), but it also decreases TI by the largest magnitude. The reason for this is that the method of derating decreases the $C_t$ for the first turbine the most aggressively. Specifically for derating by 60%, turbine 1 achieves the lowest $C_t$ value of 0.4 out of all cases. A lower $C_t$ value encourages a weaker shear layer thus weaker tip vortices. These weaker vortices mean there is less rotor-induced turbulence generation, which results in a reduced TI for downstream wakes.

Under the fully aligned conditions of the turbines for this model, lessening the wake is best for controlling the effect of turbulence on the downstream turbines' fatigue rather than redirecting the wake. This means that the AIC method out-performs yaw control for decreasing the TI. This is specifically because yaw deflects the wake, and the downstream may see less turbulence intensity because of this. But yaw control does nothing to physically reduce the turbulence content at all; the same level of TI for the wake remains through every yaw case. At the same time AIC method's strategy is to directly lessen the wake and actually reduce the generated turbulence at the rotor source. Alongside this is the observation shown with figures 35 and 34, that the streamwise turbulence intensity assessment reveals that yaw control does lead to a very slight decrease in TI seen by the hub height of the downstream turbine. The reason for this effect is explained previously, and is mainly due to the wake being redirected so that the most intense section of the wake is no longer aligned with the hub. Overall, with the largest decrease in turbulence intensity being 18.01%, this would decrease the risk for fatigue, but it cannot be said with certainty what the actual change in structural load would be without more calculations.

One last and very important topic is the trade-off between increasing total power production and increasing the risk for fatigue. The principle of this trade-off is that every strategy that decreases the turbulence intensity for the downstream achieves this through the $C_t$ value lowering. Then, as the $C_t$ is reduced, the power output decreases. This is not desired because an ideal case would include a reduced TI with an increased total power production. Unfortunately, there is no case in this study that achieves that unrealistic goal, and figures 33, 34, and 35 prove it.

It is already mentioned previously that despite the pitching by -2.5° case producing the highest total power for this research's specific scenario, that yaw control is a better overall wake control method for maximizing total power production. This is because for this specific IEA 15 MW turbine it is designed to operate below its optimal TSR. When a turbine is operating below optimal TSR, pitching toward stall maximizes power output better. Therefore, the pitching by -2.5° and -5° cases have the best power output, but not due to wake control methods and effects. Simultaneously, the AIC via derating cases best decrease TI and the risk of fatigue for downstream turbines.

To properly assess the benefits and disadvantages of increasing or decreasing fatigue risk and power production, it is essential to mention that the largest reduced TI case is by 18.01% for turbine 2. Considering no structural load calculations are done and that TI is being used as a proxy indicator of fatigue risk, it is unable to be determined if this is significant enough of a change to genuinely impact fatigue risk. In the end, the most balanced performance for power and TI is desired. The case of yaw by 10° offers the best balance, and yaw control in general is the most balanced wake management method. This is because the yaw control cases generally do not drastically decrease the total power output or increase the turbulence intensity, as seen in figure 35. The factor that would best determine which control method and specific case is optimal is the economic standpoint. Future research should include a levelized cost of electricity analysis. This would consider the money saved by reducing fatigue due to less maintenance and a longer lifetime of the turbine. The increased power production would also be financially considered as more revenue would come from more power production.

# 6 Conclusion

The research surrounding wind turbines initially revolved around improving the performance of a singular turbine and as certain parameters have been optimized, the current advancement goals now majorly involve how the turbines behave and operate in arrays. Specifically, studying how turbine wakes interfere with the performance of downstream turbines by using wake control methods is the current point of improvement for this field. The majority of research in the most recent years on this topic has been for smaller (5 MW) on-shore turbines where the studies typically only look at the effects of one method at a time with respect to only power output or structural fatigue. This thesis provides a high fidelity CFD study where three wake management techniques are modeled separately and compared based on total farm power output and risk of structural fatigue for a large (IEA 15 MW) off-shore turbine. The three wake control approaches are axial induction control via blade pitching, AIC via derating, and yaw control. This topic becomes increasingly important in this field also because over the years wind turbine size has been steadily growing and will continue to grow. The effects of wake management can vary significantly based on the design and size of the turbine.

A first conclusion of this comprehensive study is that the derating 60% case gives the best reduction in turbulence intensity for the wake of the first turbine. In this thesis, turbulence intensity is used as a qualitative proxy for the risk of fatigue on the downstream turbines. So, there are no conclusions or calculations of the physical structural loading, but it can be said that the derating 60% case reduced the risk for structural the best out of all cases. Another conclusion related to fatigue risk is that there is a significant trade-off relationship between power production and structural fatigue risk. For every wake control method that reduces TI, it decreases power at the same time, and vise versa.

Next, looking at power production alone, the case of blade pitching by $-2.5°$ increases total farm power production the most by 1.37%. This is because the turbine's design TSR is lower than the optimal TSR due to the larger size of the IEA 15 MW turbine. Therefore, the pitching increases the first turbine's $C_p$ closer to optimal $C_p$ for the blade data used. Additionally, only the power output of turbine 1 increases, while the two downstream turbines decrease in power, meaning the rise in total farm power is solely due to the optimization of turbine 1 and not because of the wake management strategy. Instead, yaw control best increases power output through wake management mechanisms. Yawing $10°$ increases total power output by 0.32% by increasing the power production of the two downstream turbines. Theoretically, a final conclusion that can be drawn is that if negative pitch and yawing were combined for this specific turbine and set-up, then this could potentially increase farm output even more. This theory requires many additional aspects of future research to determine if this is a reasonable conclusion.

To build upon this and other past studies involving wake control methods for wind turbines, researching combined methods would be beneficial. The next step is determining what combinations of methods produce the best power and fatigue risk, considering the trade-off between these two variables. Alongside this, actual structural load calculations would add significant depth to this study, rather than just relating trends in turbulence intensity to expected trends in fatigue. Hard numbers would also make it possible to perform levelized cost of electricity calculations. For real world applications, the choice of the best strategy depends on economic considerations; whichever method produces the most revenue and reduces operation and maintenance costs. Then, the levelized cost of electricity (LCOE) could serve as an extremely helpful metric in evaluating the trade-off between fatigue and power production. More supporting future research should include varying the wind speed, the atmospheric boundary layer, the spacing between turbines, and the alignment of the farm arrays. The last important factor that could produce higher fidelity results would be to use large eddy simulations for resolving turbulent fluctuations, if not limited by computational cost.

# References

[1] IRENA, “Renewable Energy Statistics 2025,” International Renewable Energy Agency IRENA, Tech. Rep., 2025.

[2] D. Van Der Hoek, J. Frederik, M. Huang, F. Scarano, C. Simao Ferreira, and J.-W. Van Wingerden, “Experimental analysis of the effect of dynamic induction control on a wind turbine wake,” en, *Wind Energy Science*, vol. 7, no. 3, pp. 1305–1320, Jun. 2022, ISSN: 2366-7451. DOI: 10.5194/wes-7-1305-2022. Accessed: May 12, 2026. [Online]. Available: https://wes.copernicus.org/articles/7/1305/2022/.

[3] M. Vali, V. Petrovic, L. Y. Pao, and M. Kuhn, “Model Predictive Active Power Control for Optimal Structural Load Equalization in Waked Wind Farms,” *IEEE Transactions on Control Systems Technology*, vol. 30, no. 1, pp. 30–44, Jan. 2022, ISSN: 1063-6536, 1558-0865, 2374-0159. DOI: 10.1109/TCST.2021.3053776. Accessed: May 12, 2026. [Online]. Available: https://ieeexplore.ieee.org/document/9345792/.

[4] D. R. Houck, “Review of wake management techniques for wind turbines,” en, *Wind Energy*, vol. 25, no. 2, pp. 195–220, Feb. 2022, ISSN: 1095-4244, 1099-1824. DOI: 10.1002/we.2668. Accessed: Mar. 26, 2026. [Online]. Available: https://onlinelibrary.wiley.com/doi/10.1002/we.2668.

[5] T. Burton, N. Jenkins, D. Sharpe, and E. Bossanyi, *Wind Energy Handbook*, en, 1st ed. Wiley, May 2011, ISBN: 9780470699751 9781119992714. DOI: 10.1002/9781119992714. Accessed: May 17, 2026. [Online]. Available: https://onlinelibrary.wiley.com/doi/book/10.1002/9781119992714.

[6] D. Dilip and F. Porté-Agel, “Wind Turbine Wake Mitigation through Blade Pitch Offset,” en, *Energies*, vol. 10, no. 6, p. 757, May 2017, ISSN: 1996-1073. DOI: 10.3390/en10060757. Accessed: May 17, 2026. [Online]. Available: https://www.mdpi.com/1996-1073/10/6/757.

[7] M. N. Kaya, O. Uzol, D. Ingham, F. Köse, and R. Buyukzeren, “The aerodynamic effects of blade pitch angle on small horizontal axis wind turbines,” en, *International Journal of Numerical Methods for Heat & Fluid Flow*, vol. 33, no. 1, pp. 120–134, Jan. 2023, ISSN: 0961-5539, 0961-5539. DOI: 10.1108/HFF-02-2022-0128. Accessed: May 17, 2026. [Online]. Available: http://www.emerald.com/hff/article/33/1/120-134/73953.

[8] P. Fleming et al., “Simulation comparison of wake mitigation control strategies for a two-turbine case: Simulation comparison of wake mitigation control strategies for a two-turbine case,” en, *Wind Energy*, vol. 18, no. 12, pp. 2135–2143, Dec. 2015, ISSN: 10954244. DOI: 10.1002/we.1810. Accessed: May 17, 2026. [Online]. Available: https://onlinelibrary.wiley.com/doi/10.1002/we.1810.

[9] C. Galinos, T. J. Larsen, and M. Mirzaei, “Impact on wind turbine loads from different down regulation control strategies,” *Journal of Physics: Conference Series*, vol. 1104, p. 012 019, Oct. 2018, ISSN: 1742-6588, 1742-6596. DOI: 10.1088/1742-6596/1104/1/012019. Accessed: May 17, 2026. [Online]. Available: https://iopscience.iop.org/article/10.1088/1742-6596/1104/1/012019.

[10] J. Bartl and L. Sætran, "Experimental testing of axial induction based control strategies for wake control and wind farm optimization," *Journal of Physics: Conference Series*, vol. 753, p. 032 035, Sep. 2016, ISSN: 1742-6588, 1742-6596. DOI: 10.1088/1742-6596/753/3/032035. Accessed: May 17, 2026. [Online]. Available: https://iopscience.iop.org/article/10.1088/1742-6596/753/3/032035.

[11] P. M. O. Gebraad et al., "Wind plant power optimization through yaw control using a parametric model for wake effects-a CFD simulation study: Wind plant optimization by yaw control using a parametric wake model," en, *Wind Energy*, vol. 19, no. 1, pp. 95–114, Jan. 2016, ISSN: 10954244. DOI: 10.1002/we.1822. Accessed: May 12, 2026. [Online]. Available: https://onlinelibrary.wiley.com/doi/10.1002/we.1822.

[12] J. Bartl, F. Mühle, and L. Sætran, "Wind tunnel study on power output and yaw moments for two yaw-controlled model wind turbines," en, *Wind Energy Science*, vol. 3, no. 2, pp. 489–502, Aug. 2018, ISSN: 2366-7451. DOI: 10.5194/wes-3-489-2018. Accessed: May 15, 2026. [Online]. Available: https://wes.copernicus.org/articles/3/489/2018/.

[13] S. T. Frandsen, "Turbulence and turbulence-generated structural loading in wind turbine clusters," Doctoral thesis, 2007, ISBN: 87-550-3458-6.

[14] K. Thomsen and P. Sørensen, "Fatigue loads for wind turbines operating in wakes," en, *Journal of Wind Engineering and Industrial Aerodynamics*, vol. 80, no. 1-2, pp. 121–136, Mar. 1999, ISSN: 01676105. DOI: 10.1016/S0167-6105(98)00194-9. Accessed: May 17, 2026. [Online]. Available: https://linkinghub.elsevier.com/retrieve/pii/S0167610598001949.

[15] S. Ali, M. Waleed, and D. Lee, "Structural Load Optimization of 15 MW Offshore Wind Turbine Using LHS-Based Design Space," en, *Journal of Marine Science and Engineering*, vol. 13, no. 6, p. 1066, May 2025, ISSN: 2077-1312. DOI: 10.3390/jmse13061066. Accessed: May 17, 2026. [Online]. Available: https://www.mdpi.com/2077-1312/13/6/1066.

[16] J. Sun et al., "Wake redirection control for offshore wind farm power and fatigue multi-objective optimisation based on a wind turbine load indicator," en, *Energy*, vol. 313, p. 133 893, Dec. 2024, ISSN: 03605442. DOI: 10.1016/j.energy.2024.133893. Accessed: May 17, 2026. [Online]. Available: https://linkinghub.elsevier.com/retrieve/pii/S0360544224036715.

[17] L. Zhao et al., "Study on Mitigation of Wake Interference by Combined Control of Yaw Misalignment and Pitch," en, *Journal of Marine Science and Engineering*, vol. 11, no. 7, p. 1288, Jun. 2023, ISSN: 2077-1312. DOI: 10.3390/jmse11071288. Accessed: May 17, 2026. [Online]. Available: https://www.mdpi.com/2077-1312/11/7/1288.

[18] M. J. LoCascio, C. J. Bay, M. Bastankhah, G. E. Barter, P. A. Fleming, and L. A. Martínez-Tossas, "FLOW Estimation and Rose Superposition (FLOWERS): An integral approach to engineering wake models," en, *Wind Energy Science*, vol. 7, no. 3, pp. 1137–1151, Jun. 2022, ISSN: 2366-7451. DOI: 10.5194/wes-7-1137-2022. Accessed: May 13, 2026. [Online]. Available: https://wes.copernicus.org/articles/7/1137/2022/.

[19] L. Vermeer, J. Sørensen, and A. Crespo, "Wind turbine wake aerodynamics," en, *Progress in Aerospace Sciences*, vol. 39, no. 6-7, pp. 467–510, Aug. 2003, ISSN: 03760421. DOI: 10.1016/S0376-0421(03)00078-2. Accessed: May 13, 2026. [Online]. Available: https://linkinghub.elsevier.com/retrieve/pii/S0376042103000782.

[20] A. Crespo and J. Herna´ndez, "Turbulence characteristics in wind-turbine wakes," en, *Journal of Wind Engineering and Industrial Aerodynamics*, vol. 61, no. 1, pp. 71–85, Jun. 1996, ISSN: 01676105. DOI: 10.1016/0167-6105(95)00033-X. Accessed: May 13, 2026. [Online]. Available: https://linkinghub.elsevier.com/retrieve/pii/016761059500033X.

[21] M. Bastankhah and F. Porté-Agel, "Experimental and theoretical study of wind turbine wakes in yawed conditions," en, *Journal of Fluid Mechanics*, vol. 806, pp. 506–541, Nov. 2016, ISSN: 0022-1120, 1469-7645. DOI: 10.1017/jfm.2016.595. Accessed: May 12, 2026. [Online]. Available: https://www.cambridge.org/core/product/identifier/S0022112016005954/type/journal_article.

[22] M. Bastankhah and F. Porté-Agel, "A new analytical model for wind-turbine wakes," en, *Renewable Energy*, vol. 70, pp. 116–123, Oct. 2014, ISSN: 09601481. DOI: 10.1016/j.renene.2014.01.002. Accessed: May 13, 2026. [Online]. Available: https://linkinghub.elsevier.com/retrieve/pii/S0960148114000317.

[23] W. Hu, K. K. Choi, O. Zhupanska, and J. H. Buchholz, "Integrating variable wind load, aerodynamic, and structural analyses towards accurate fatigue life prediction in composite wind turbine blades," en, *Structural and Multidisciplinary Optimization*, vol. 53, no. 3, pp. 375–394, Mar. 2016, ISSN: 1615-147X, 1615-1488. DOI: 10.1007/s00158-015-1338-5. Accessed: May 17, 2026. [Online]. Available: http://link.springer.com/10.1007/s00158-015-1338-5.

[24] S. Mozafari, P. Veers, J. Rinker, and K. Dykes, "Sensitivity of fatigue reliability in wind turbines: Effects of design turbulence and the Wöhler exponent," en, *Wind Energy Science*, vol. 9, no. 4, pp. 799–820, Apr. 2024, ISSN: 2366-7451. DOI: 10.5194/wes-9-799-2024. Accessed: May 17, 2026. [Online]. Available: https://wes.copernicus.org/articles/9/799/2024/.

[25] Internationale Elektrotechnische Kommission, Ed., *Design requirements* (Wind energy generation systems / International Electrotechnical Commission part 1), eng, Edition 4.0. Geneva, Switzerland: International Electrotechnical Commission, 2019, ISBN: 9782832262535.

[26] D. Vahidi and F. Porté-Agel, "Influence of thrust coefficient on the wake of a wind turbine: A numerical and analytical study," en, *Renewable Energy*, vol. 240, p. 122 194, Feb. 2025, ISSN: 09601481. DOI: 10.1016/j.renene.2024.122194. Accessed: May 5, 2026. [Online]. Available: https://linkinghub.elsevier.com/retrieve/pii/S0960148124022626.

[27] S. Kanev, F. Savenije, and W. Engels, "Active wake control: An approach to optimize the lifetime operation of wind farms," en, *Wind Energy*, vol. 21, no. 7, pp. 488–501, Jul. 2018, ISSN: 1095-4244, 1099-1824. DOI: 10.1002/we.2173. Accessed: May 4, 2026. [Online]. Available: https://onlinelibrary.wiley.com/doi/10.1002/we.2173.

[28] R. Nash, R. Nouri, and A. Vasel-Be-Hagh, “Wind turbine wake control strategies: A review and concept proposal,” en, *Energy Conversion and Management*, vol. 245, p. 114 581, Oct. 2021, ISSN: 01968904. DOI: 10.1016/j.enconman.2021.114581. Accessed: May 17, 2026. [Online]. Available: https://linkinghub.elsevier.com/retrieve/pii/S0196890421007573.

[29] J. Aho et al., “A tutorial of wind turbine control for supporting grid frequency through active power control,” in *2012 American Control Conference (ACC)*, Montreal, QC: IEEE, Jun. 2012, pp. 3120–3131, ISBN: 9781457710964 9781457710957 9781457710940 9781467321020. DOI: 10.1109/ACC.2012.6315180. Accessed: May 11, 2026. [Online]. Available: http://ieeexplore.ieee.org/document/6315180/.

[30] S. Boersma et al., “A tutorial on control-oriented modeling and control of wind farms,” in *2017 American Control Conference (ACC)*, Seattle, WA, USA: IEEE, May 2017, pp. 1–18, ISBN: 9781509059928. DOI: 10.23919/ACC.2017.7962923. Accessed: May 11, 2026. [Online]. Available: https://ieeexplore.ieee.org/document/7962923/.

[31] M. F. Howland, S. K. Lele, and J. O. Dabiri, “Wind farm power optimization through wake steering,” en, *Proceedings of the National Academy of Sciences*, vol. 116, no. 29, pp. 14 495–14 500, Jul. 2019, ISSN: 0027-8424, 1091-6490. DOI: 10.1073/pnas.1903680116. Accessed: May 12, 2026. [Online]. Available: https://pnas.org/doi/full/10.1073/pnas.1903680116.

[32] P. Fleming et al., “Initial results from a field campaign of wake steering applied at a commercial wind farm – Part 1,” en, *Wind Energy Science*, vol. 4, no. 2, pp. 273–285, May 2019, ISSN: 2366-7451. DOI: 10.5194/wes-4-273-2019. Accessed: May 12, 2026. [Online]. Available: https://wes.copernicus.org/articles/4/273/2019/.

[33] S. B. Pope, *Turbulent flows*, eng, 1. publ., 12. print. Cambridge: Cambridge Univ. Press, 2000, ISBN: 9780521598866 9780521591256.

[34] B. Sanderse, S. Van Der Pijl, and B. Koren, “Review of computational fluid dynamics for wind turbine wake aerodynamics,” en, *Wind Energy*, vol. 14, no. 7, pp. 799–819, Oct. 2011, ISSN: 1095-4244, 1099-1824. DOI: 10.1002/we.458. Accessed: May 15, 2026. [Online]. Available: https://onlinelibrary.wiley.com/doi/10.1002/we.458.

[35] H. K. Versteeg and W. Malalasekera, *An introduction to computational fluid dynamics: the finite volume method*, eng, 2. ed., [Nachdr.] Harlow: Pearson/Prentice Hall, 2007, ISBN: 9780131274983.

[36] J. N. Sorensen and W. Z. Shen, “Numerical Modeling of Wind Turbine Wakes,” en, *Journal of Fluids Engineering*, vol. 124, no. 2, pp. 393–399, Jun. 2002, ISSN: 0098-2202, 1528-901X. DOI: 10.1115/1.1471361. Accessed: May 7, 2026. [Online]. Available: https://asmedigitalcollection.asme.org/fluidsengineering/article/124/2/393/444521/Numerical-Modeling-of-Wind-Turbine-Wakes.

[37] L. Martinez, S. Leonardi, M. Churchfield, and P. Moriarty, “A Comparison of Actuator Disk and Actuator Line Wind Turbine Models and Best Practices for Their Use,” en, in *50th AIAA Aerospace Sciences Meeting including the New Horizons Forum and Aerospace Exposition*, Nashville, Tennessee: American Institute of Aeronautics and Astronautics, Jan. 2012, ISBN: 9781600869365. DOI: 10.2514/6.2012-900. Accessed: May 7, 2026. [Online]. Available: https://arc.aiaa.org/doi/10.2514/6.2012-900.

[38] M. Ravensbergen, A. Bayram Mohamed, and A. Korobenko, “The actuator line method for wind turbine modelling applied in a variational multiscale framework,” en, *Computers & Fluids*, vol. 201, p. 104 465, Apr. 2020, ISSN: 00457930. DOI: 10.1016/j.compfluid.2020.104465. Accessed: May 10, 2026. [Online]. Available: https://linkinghub.elsevier.com/retrieve/pii/S0045793020300384.

[39] L. A. Martínez-Tossas, M. J. Churchfield, and C. Meneveau, “Optimal smoothing length scale for actuator line models of wind turbine blades based on Gaussian body force distribution,” en, *Wind Energy*, vol. 20, no. 6, pp. 1083–1096, Jun. 2017, ISSN: 1095-4244, 1099-1824. DOI: 10.1002/we.2081. Accessed: May 10, 2026. [Online]. Available: https://onlinelibrary.wiley.com/doi/10.1002/we.2081.

[40] N. Troldborg, “Actuator Line Modeling of Wind Turbine Wakes,” PhD Thesis, Technical University of Denmark, Lyngby, Denmark, 2008.

[41] P. Melani, F. Balduzzi, and A. Bianchini, “Simulating tip effects in vertical-axis wind turbines with the actuator line method,” *Journal of Physics: Conference Series*, vol. 2265, no. 3, p. 032 028, May 2022, ISSN: 1742-6588, 1742-6596. DOI: 10.1088/1742-6596/2265/3/032028. Accessed: May 20, 2026. [Online]. Available: https://iopscience.iop.org/article/10.1088/1742-6596/2265/3/032028.

[42] R. Stanly, L. A. Martínez-Tossas, S. H. Frankel, and Y. Delorme, “Large-Eddy Simulation of a wind turbine using a Filtered Actuator Line Model,” en, *Journal of Wind Engineering and Industrial Aerodynamics*, vol. 222, p. 104 868, Mar. 2022, ISSN: 01676105. DOI: 10.1016/j.jweia.2021.104868. Accessed: May 17, 2026. [Online]. Available: https://linkinghub.elsevier.com/retrieve/pii/S016761052100341X.

[43] J. Svensson, *Wind Power Systems - Siting, System Design & Integration*, Lecture slides, Lund University, Nov. 2025.

[44] E. Gaertner et al., *IEA Wind TCP Task 37 Definition of the IEA Wind 15-Megawatt Offshore Reference Wind Turbine Technical Report*. 2020. [Online]. Available: https://www.nrel.gov/docs/fy20osti/75698.pdf.

[45] J. Wieringa, “Updating the Davenport roughness classification,” en, *Journal of Wind Engineering and Industrial Aerodynamics*, vol. 41, no. 1-3, pp. 357–368, Oct. 1992, ISSN: 01676105. DOI: 10.1016/0167-6105(92)90434-C. Accessed: May 25, 2026. [Online]. Available: https://linkinghub.elsevier.com/retrieve/pii/016761059290434C.

[46] P. Bachant, A. Goude, and M. Wosnik, *Turbinesfoam*, https://github.com/turbinesFoam/turbinesFoam, Accessed: 2025, 2018.

[47] A. Elkodama, A. Ismaiel, A. Abdellatif, S. Shaaban, S. Yoshida, and M. A. Rushdi, “Control Methods for Horizontal Axis Wind Turbines (HAWT): State-of-the-Art Review,” en, *Energies*, vol. 16, no. 17, p. 6394, Sep. 2023, ISSN: 1996-1073. DOI: 10.3390/en16176394. Accessed: May 17, 2026. [Online]. Available: https://www.mdpi.com/1996-1073/16/17/6394.

[48] C. G. Anderson, *Wind Turbines: Theory and Practice*, 2nd ed. Cambridge University Press, Dec. 2024, ISBN: 9781009499040 9781009499026. DOI: 10.1017/9781009499040. Accessed: May 17, 2026. [Online]. Available: https://www.cambridge.org/highereducation/product/9781009499040/book.

[49] J. Kazda, M. Zendehbad, S. Jafari, N. Chokani, and R. Abhari, “Mitigating adverse wake effects in a wind farm using non-optimum operational conditions,” en, *Journal of Wind Engineering and Industrial Aerodynamics*, vol. 154, pp. 76–83, Jul. 2016, ISSN: 01676105. DOI: 10.1016/j.jweia.2016.04.004. Accessed: May 15, 2026. [Online]. Available: https://linkinghub.elsevier.com/retrieve/pii/S0167610516302264.

[50] P. A. Fleming et al., “Evaluating techniques for redirecting turbine wakes using SOWFA,” en, *Renewable Energy*, vol. 70, pp. 211–218, Oct. 2014, ISSN: 09601481. DOI: 10.1016/j.renene.2014.02.015. Accessed: May 15, 2026. [Online]. Available: https://linkinghub.elsevier.com/retrieve/pii/S0960148114000950.

# A Appendix

In this section, all excess post-processing figures for each case, AIC via pitching, AIC via derating and yaw control, are presented. All figures in this section are represented as a z-slice at hub height, scaled for a UX range of 6-11m/s.

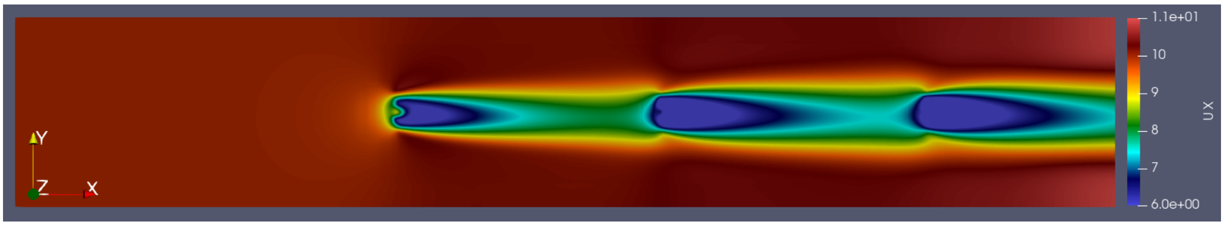


Figure 36: Normalised streamwise velocity $U_x$ at hub height ($z$ = 150 m) for the yaw 10° case. Flow direction is left to right.

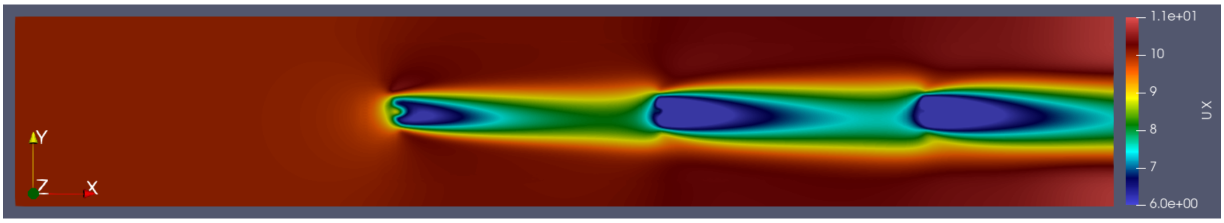


Figure 37: Normalised streamwise velocity $U_x$ at hub height ($z$ = 150 m) for the yaw 20° case. Flow direction is left to right.

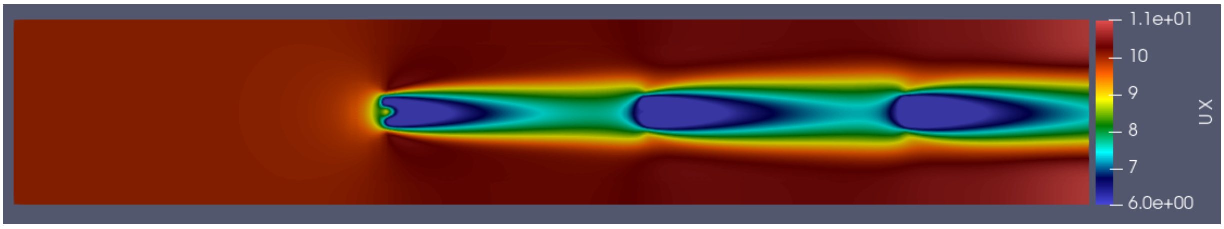


Figure 38: Normalised streamwise velocity $U_x$ at hub height ($z$ = 150 m) for the pitch −2.5° case. Flow direction is left to right.

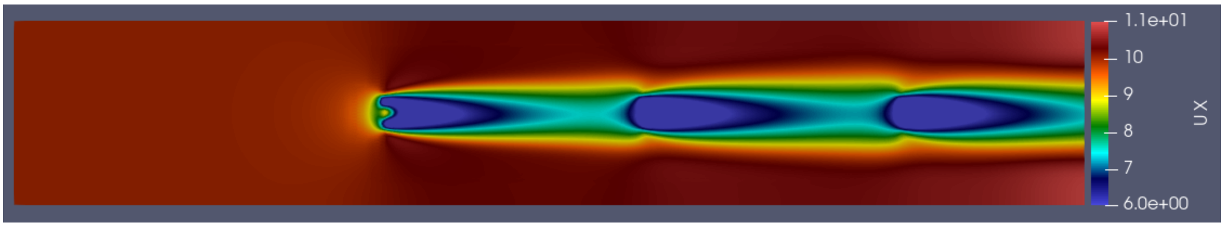


Figure 39: Normalised streamwise velocity $U_x$ at hub height ($z$ = 150 m) for the pitch −5° case. Flow direction is left to right.

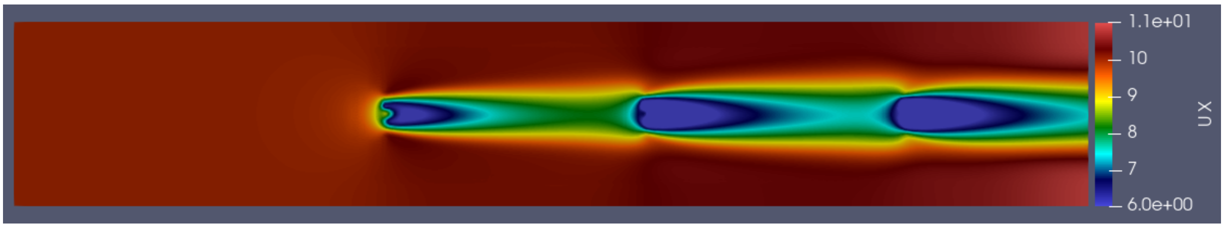


Figure 40: Normalised streamwise velocity $U_x$ at hub height ($z$ = 150 m) for the pitch +2.5° case. Flow direction is left to right.

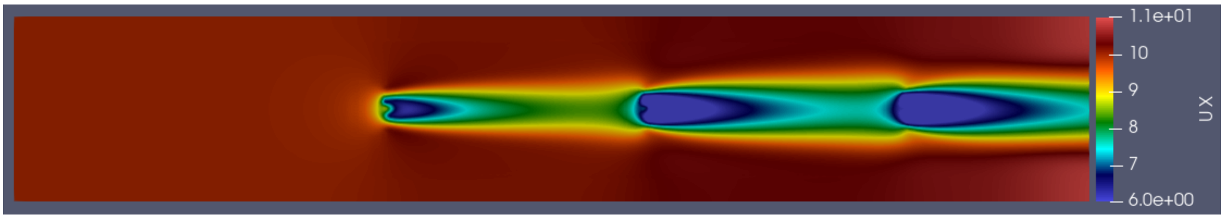


Figure 41: Normalised streamwise velocity $U_x$ at hub height ($z$ = 150 m) for the pitch +5° case. Flow direction is left to right.

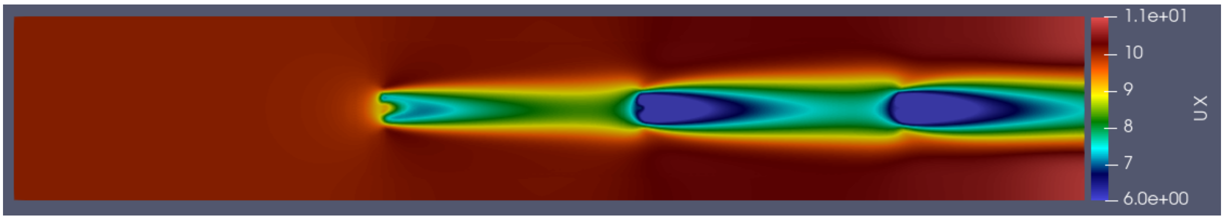


Figure 42: Normalised streamwise velocity $U_x$ at hub height ($z$ = 150 m) for the derating 90% case. Flow direction is left to right.

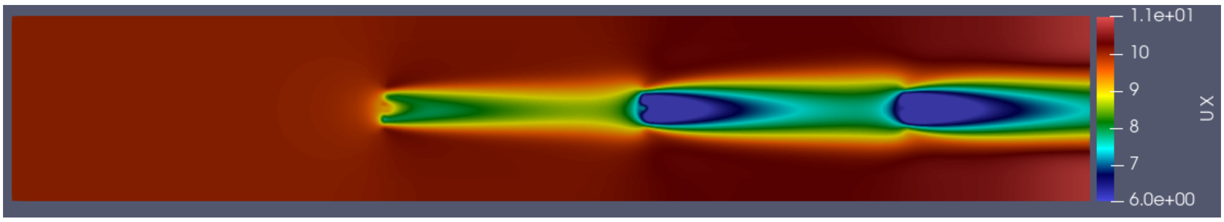


Figure 43: Normalised streamwise velocity $U_x$ at hub height ($z$ = 150 m) for the derating 75% case. Flow direction is left to right.

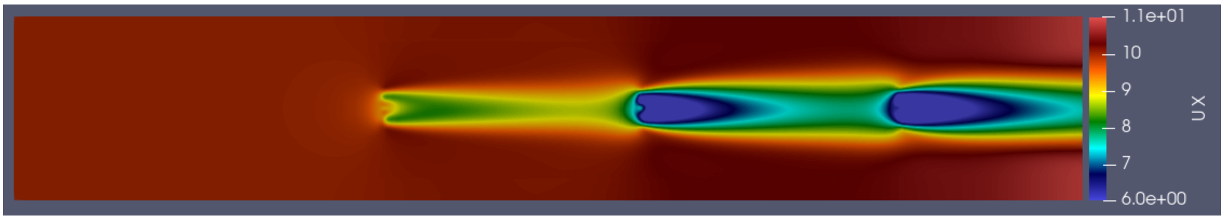


Figure 44: Normalised streamwise velocity $U_x$ at hub height ($z$ = 150 m) for the derating 60% case. Flow direction is left to right.

# B Appendix

In this section, all excess data related to the simulation can be found: blade data, element data, and the run script for the base case. The actual simulation contains further files, which are called upon in the run script. Such files will not be presented in this Appendix.

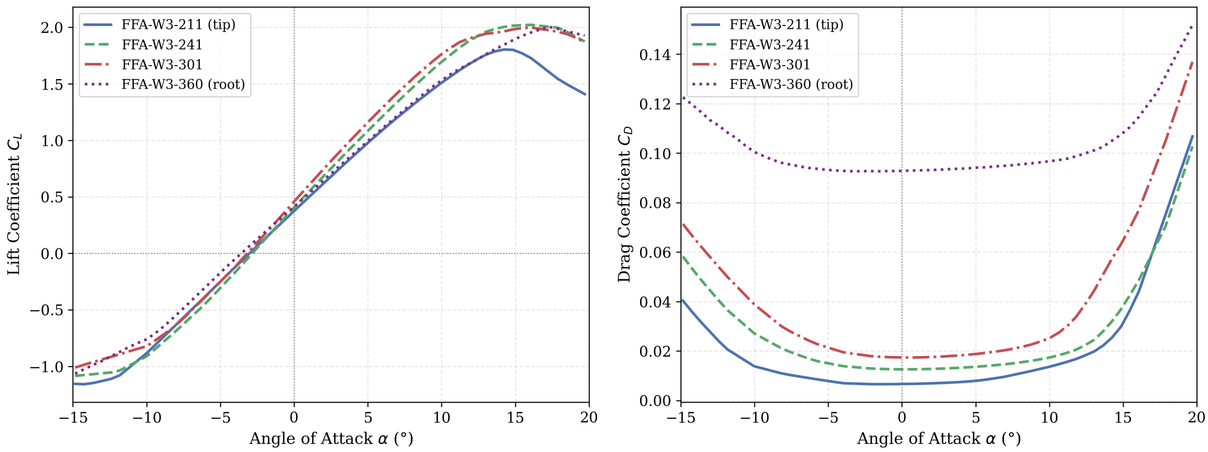


Figure 45: Lift coefficient $C_L$ and drag coefficient $C_D$ as functions of angle of attack for the four FFA-W3 airfoil profiles used in the IEA-15-240 RWT blade element discretisation. Polar data sourced from the IEA-15-240-RWT AeroDyn15 polar database [44]

Table 9: Element data of the blade used in the simulation. Data gathered from IEA-15-240-RWTAeroDyn15 blade file [44].

| Axial Distance | Radius | Azimuth | Chord | Chord Mount | Twist Angle |
|---|---|---|---|---|---|
| 0 | 2 | 0 | 5.2075 | 0.25 | 15.59 |
| 0 | 13.0667 | 0 | 5.4936 | 0.25 | 12.94 |
| 0 | 14.6664 | 0 | 5.5517 | 0.25 | 12.28 |
| 0 | 18 | 0 | 5.6602 | 0.25 | 10.84 |
| 0 | 21.9996 | 0 | 5.7477 | 0.25 | 9.22 |
| 0 | 26.0004 | 0 | 5.757 | 0.25 | 7.91 |
| 0 | 30 | 0 | 5.6477 | 0.25 | 6.83 |
| 0 | 33.9996 | 0 | 5.4364 | 0.25 | 5.79 |
| 0 | 38.0004 | 0 | 5.1794 | 0.25 | 4.84 |
| 0 | 42 | 0 | 4.9406 | 0.25 | 4.03 |
| 0 | 45.9996 | 0 | 4.7381 | 0.25 | 3.35 |
| 0 | 50.0004 | 0 | 4.5478 | 0.25 | 2.75 |
| 0 | 54 | 0 | 4.3597 | 0.25 | 2.23 |
| 0 | 57.9996 | 0 | 4.1772 | 0.25 | 1.75 |
| 0 | 62.0004 | 0 | 4.0025 | 0.25 | 1.31 |
| 0 | 66 | 0 | 3.8375 | 0.25 | 0.92 |
| 0 | 69.9996 | 0 | 3.6799 | 0.25 | 0.57 |
| 0 | 74.0004 | 0 | 3.5267 | 0.25 | 0.24 |
| 0 | 78 | 0 | 3.3727 | 0.25 | -0.1 |
| 0 | 81.9996 | 0 | 3.2172 | 0.25 | -0.5 |
| 0 | 86.0004 | 0 | 3.0634 | 0.25 | -1 |
| 0 | 90 | 0 | 2.9093 | 0.25 | -1.53 |
| 0 | 93.9996 | 0 | 2.7517 | 0.25 | -1.96 |
| 0 | 98.0004 | 0 | 2.5876 | 0.25 | -2.16 |
| 0 | 102 | 0 | 2.4136 | 0.25 | -2.16 |
| 0 | 105.9996 | 0 | 2.2324 | 0.25 | -2.07 |
| 0 | 110.0004 | 0 | 2.0451 | 0.25 | -1.89 |
| 0 | 114 | 0 | 1.8502 | 0.25 | -1.56 |
| 0 | 117.9996 | 0 | 0.5 | 0.25 | -1.24 |
| 0 | 120 | 0 | 0.5 | 0.25 | -1.24 |

Script 1: SLURM run script for base case simulation.

```bash
#!/bin/bash
#
#SBATCH -A LU2026-2-25
#no. of cores
#SBATCH -N 1
#SBATCH --tasks-per-node=48
#SBATCH --exclusive
#Job time
#SBATCH -t 48:00:00
#SBATCH --mail-user=ju1567ho-s@lu.se
#job name
#SBATCH -J bpCase3
#
#SBATCH -o thick_%j.out
#SBATCH -e thick_%j.err
#
cat $0
export FOAM_RUN=/home/jholz/lu2025-12-17/jholz/OpenFOAM/xjobb-v2406/run
cd $FOAM_RUN/bpCase3
echo "RUNNING IN: $(pwd)"
#module load intel
module load GCC/12.3.0
module load OpenMPI/4.1.5
module load OpenFOAM/v2406
. $FOAM_INST_DIR/OpenFOAM-v2406/etc/bashrc
export LD_LIBRARY_PATH=$LD_LIBRARY_PATH:/home/jholz/lu2025-12-17/jholz/OpenFOAM/xjobb-v2406/platforms/linux64GccDPInt32Opt/lib
rm -rf constant/polyMesh
blockMesh > logbm 2>&1
snappyHexMesh -overwrite > logsnappm 2>&1
checkMesh > logcheck 2>&1
topoSet > logtopo 2>&1
decomposePar -force > logde 2>&1
mpirun -np 48 pimpleFoam -parallel > log 2>&1
reconstructPar -latestTime > logrep 2>&1
```

# C Division of Work

This project was researched and written jointly by both authors of this paper. This division of work does its best to outline which tasks were performed by which author, but in reality almost every undertaking was done with some level of collaboration. Firstly, for the research aspects of the thesis, Birta Aradóttir performed a literature review, created the mesh & its parameters, created the domain size & layout of the turbines, selected the time parameters, ran & set up all cases for yaw control, ran & set up all cases for derating, and created the blades in OpenFOAM. Julia Holz completed a literature review, the mesh sensitivity analysis, validated the simulation, created the ABL velocity profile, determined all boundary conditions, performed the QBlade BEM analysis, and ran & set up all cases for blade pitching. Secondly, for the division of work for the writing of the report, Birta and Julia both wrote the theory section, the methods section, the results section, and discussion. Birta wrote the appendix, abstract, and specifically the yaw, derating, and comparative parts of the discussion. Julia wrote the introduction, conclusion, and the blade pitching & comparative parts of the discussion. All challenges throughout this project were handled and discussed by both authors.